2019

# STRAINTRONIC NANOMAGNETIC DEVICES FOR NON-BOOLEAN COMPUTING

Md Ahsanul Abeed
*Virginia Commonwealth University*

www.manaraa.com

# STRAINTRONIC NANOMAGNETIC DEVICES FOR NON-BOOLEAN COMPUTING

A Dissertation submitted in partial fulfillment of the requirements for the degree of Doctor of Philosophy in Engineering at Virginia Commonwealth University.

by

Md Ahsanul Abeed

Bachelor of Science in Electrical and Electronic Engineering, Bangladesh University of Engineering and Technology, 2013

Doctoral Committee Chairperson: Supriyo Bandyopadhyay

Commonwealth Professor, Department of Electrical and Computer Engineering

Virginia Commonwealth University
Richmond, Virginia
August 2019

# Acknowledgement

First of all, I would like to express my gratitude to my advisor, Professor Supriyo Bandyopadhyay. It has been a privilege to have been educated by him, not only for providing precious ideas, comments, and critiques with his profound knowledge in Spintronics and Straintronics but also for his exceptional ability to elucidate any complex topic. I am very much thankful to him for all the efforts that he has made for my personal development as a researcher. Spending all these years under his supervision, I have learnt a lot about conducting a fruitful research. I am also thankful to him not only to supervise me in my research projects while evolving as a researcher but also in finding the right directions and helping me out for my personal life. Without his invaluable help, guidance, encouragement and his endless patience, this thesis would not have been possible. I am also grateful to my co-advisors Professor Jayasimha Atulasimha and Professor Gary Atkinson for their valuable suggestions and constant support. I also appreciate the helpful comments and contributions from my other committee members, Prof. Shiv Khanna and Prof. Nathanial Kinsey.

I would like to thank my collaborator at VCU with whom I had the opportunity to work with; Md Mamun Al-Rashid, Dhritiman Bhattacharya and Professor Jayasimha Atulasimha from Dept. of Mechanical and Nuclear Engineering, VCU. I learnt a lot from the discussions I had with them during our work in collaboration. Special thanks to Professor Anjan Barman and his group members for their team work during the collaboration where I was introduced and learned a different technique for magnetization and its characterization. I also offer my thanks to Dr. Dmitry Pestov in Nanomaterials Characterization Center who helped me train on the characterization equipment.

I am grateful to my colleagues, Dr. Hasnain Ahmed and Dr. Ayan Biswas, for their mentoring and guidance during my first years of graduate study. Thanks to my other colleague in the lab, Justine

Drobitch, for her help with both simulation and experiments. I would also like to thank all the great staffs in the VCU College of Engineering, who have made this journey pleasant and remarkable.

Finally, and most importantly, I would like to thank my father Md Shamsuzzaman Sarker, my mother Shamsunnahar, my brother Ahnaf Abeed, my wife Mumtarina Akter, and my son Alhan Mahrus Abeed for their love and motivation. Their continuous support has made this journey pleasant, smooth and possible.

# Table of Contents

# List of Figures

Spin textures after withdrawal of stress showing that the errant pixels are no longer white. All pixels have turned approximately black. (d) the applied stress profile in time……………………17

**Figure 2.4:** Temporal evolution of the magnetization orientation of the (a) bottom and (b) top errant nanomagnet in Fig. 5 from $\theta \approx 48.6°$ to $\theta \approx 48.6°$. Since the magnetic field due to thermal noise is random, we ran six different simulations for each of the two nanomagnets. The six switching trajectories vary slightly but all result in transitioning to the correct pixel color corresponding to $\theta = 48.6°$. (c) The temporal evolution of the magnetization of the nanomagnet in the top right corner (row 1, column 7) in Fig. 2.3. This nanomagnet corresponds to an uncorrupted pixel, but because it too is subjected to global stress and thermal noise, its magnetization changes with time. However, it returns to its original state after a brief sojourn showing that the stress does not corrupt an uncorrupted pixel. The time to settle (image processing time) is ~3 nanoseconds………………………………………………………………………………...18

**Figure 2.5:** (a) Spin textures of an array of $7 \times 7$ nanomagnets representing white segment of an image where the entire fourth row has been corrupted and turned black. Application and subsequent withdrawal of global stress along the major axes corrects the corrupted row. (b) An array of black pixels in the black segment of an image where two consecutive rows have been corrupted and turned white. Stress application and withdrawal corrects both corrupted rows. (c) An array of white pixels where two non-consecutive rows have been corrupted and turned black. A stress cycle corrects both rows. (d) An array of black pixels where two non-consecutive rows have been corrupted and turned white. Again, a stress cycle corrects both rows…………………20

**Figure 2.6:** A $7 \times 7$ array corresponding to the black segment of an image with randomly corrupted pixels (black pixels turned white). Application and subsequent removal of global stress applied

The Fourier transform peaks shift to lower frequencies with decreasing bias magnetic field strength. There are multiple oscillation modes of various Fourier amplitudes. Out of those, the dominant mode (at all bias fields except 700 Oe) is denoted by F and its nearest modes $F_H$ and $F_L$. (c) Fourier transforms of the temporal evolution of the out-of-plane magnetization component at various bias magnetic fields simulated with MuMax3 where the amplitude of the periodically varying strain anisotropy energy density $K_0$ is assumed to be 22,500 J/m$^3$. The simulation has additional (weak) higher frequency peaks not observed in the experiment. The spectra in the two right panels are used to compare simulation with experiment……………………………………...107

**Figure 8.4:** Time-lapsed images of the micromagnetic distributions within the Co nanomagnet for 1ns time period obtained from MuMax3 simulations. Time is counted from the instant the time varying strain anisotropy is turned on. A bias magnetic field of 760 Oe is directed along the minor axis of the ellipse, pointing to the right. The magnetization is initially assumed to be oriented along the bias field and an out-of-plane square wave tickle field of 30 Oe is turned on at time t = 0 for 100 ps to set the magneto-dynamics in motion……………………………………………………110

**Figure 8.5:** (a) Calculated frequency spectrum of the time variation of the spatially-averaged out-of-plane magnetization component $\bar{M}_z(t)$ in an *unstrained* elliptical Co nanomagnet in the presence of a bias magnetic field of 1000 Oe directed along the ellipse's minor axis. The quantity $\bar{M}_z(t)$ is calculated from MuMax3. (b) Calculated spin-wave mode profile in the nanomagnet for the two peak frequencies in the spectrum at different bias fields. These profiles are calculated with the Dotmag code. Since the power is concentrated at the center in one mode and vertical edges at the other, they are a 'center mode' and an 'edge mode' and this nature is independent of the bias field in this range. The units of power and phase in this plot are dB and radians, respectively…112

# List of Tables

# Abstract

Title of Dissertation: STRAINTRONIC NANOMAGNETIC DEVICES FOR NON-BOOLEAN COMPUTING

By Md Ahsanul Abeed

Bachelor of Science in Electrical and Electronic Engineering

A Dissertation submitted in partial fulfillment of the requirements for the degree of Doctor of Philosophy in Engineering at Virginia Commonwealth University.

Virginia Commonwealth University, 2019

Major Director: Supriyo Bandyopadhyay

Commonwealth Professor, Department of Electrical and Computer Engineering

Nanomagnetic devices have been projected as an alternative to transistor-based switching devices due to their non-volatility and potentially superior energy-efficiency. The energy efficiency is enhanced by the use of straintronics to switch a nanomagnet's magnetization, which involves the application of a voltage to a piezoelectric layer to generate a strain which is ultimately transferred to an elastically coupled magnetostrictive nanomaget, causing magnetization rotation. The low energy dissipation and non-volatility characteristics make straintronic nanomagnets very attractive for both Boolean and non-Boolean computing applications.

There was relatively little research on straintronic switching in devices built with real nanomagnets that invariably have defects and imperfections, or their adaptation to non-Boolean computing, both

of which have been studied in this thesis. Detailed studies of the effects of nanomagnet material fabrication defects and surface roughness variation (found in real nanomagnets) on the switching process and ultimately device performance of those switches have been performed theoretically. The results of these studies place the viability of straintronics logic (Boolean) and/or memory in question.

With a view to analog computing and signal processing, analog spin wave based device operation has been evaluated in the presence of defects and it was found that defects impact their performance, which can be a major concern for the spin wave based device community. Additionally, the design challenge for low barrier nanomagnet which is the building block of binary stochastic neurons based probabilistic computing device in case of real nanomagnets has also been investigated. This study also cast some doubt on the efficacy of probabilistic computing devices.

Fortunately, there are some non-Boolean applications based on the collective action of array of nanomagnets which are very forgiving of material defects. One example is image processing using dipole coupled nanomagnets which is studied here and it showed promising result for noise correction and edge enhancement of corrupted pixels in an image. Moreover, a single magneto tunnel junction based microwave oscillator was proposed for the first time and theoretical simulations showed that it is capable of better performance compared to traditional microwave oscillators.

The experimental part of this thesis dealt with spin wave modes excited by surface acoustic waves, studied with time resolved magneto optic Kerr effect (TR-MOKE). New hybrid spin wave modes were observed for the first time. The effect of defects on these spin wave modes was also studied

theoretically and revealed that these modes are not immune to defects. An experiment was carried out to emulate simulated annealing in a system of dipole coupled magnetostrictive nanomagnets where strain served as the simulated annealing agent. This was a promising outcome and it is the first demonstration of the hardware variant of simulated annealing of a many body system based on magnetostrictive nanomagnets.

Finally, a giant spin Hall effect actuated surface acoustic wave antenna was demonstrated experimentally. This is the first observation of photon to phonon conversion using spin-orbit torque and although the observed conversion efficiency was poor (1%), it opened the pathway for a new acoustic radiator. These studies complement past work done in our group in the area of straintronics.

# Chapter 1: Introduction

The workhorse of modern electronic devices is the complementary metal oxide semiconductor field effect transistor (CMOS) which has two major shortcomings: volatility and excessive power consumption. Volatility implies that information (in the form of the device's conductance state) is not retained reliably in the device without frequent refresh cycles and is completely lost when the device is powered off. The excessive power consumption, on the other hand, accrues from the inevitable current flow that takes place when a CMOS device is switched from "off" to "on", or vice versa. In contrast, nanomagnetic devices, which use nanomagnetic switches to mimic the functions of CMOS switches, are both non-volatile and energy-efficient. No current flow is required to take place within the nanomagnet when it switches from one magnetization state to another, and the state information can be retained almost indefinitely in the nanomagnet without refresh cycles or external energy supply. These two features can make nanomagnetic switches superior to transistors. These switches are usually built using shape anisotropic single domain nanomagnets (with two stable magnetization orientations which can be used to encode the binary bits 0 and 1). Digital information processing is carried out by switching the magnetization between these two stable orientations in the same way that transistors process digital information by switching back and forth between two conductance states.

The energy dissipation in the nanomagnetic switch depends critically on how the switching action is carried out. Traditional switching schemes involving magnetic field, spin transfer torque, etc. dissipate excessive power which offsets any advantage that the nanomagnet may have over the CMOS transistor. To reduce the energy dissipation, a different approach based on a 2-phase multiferroic nanomagnet, comprising a single domain magnetostrictive layer elastically coupled to a piezoelectric layer, is used. A strain will be generated in the piezoelectric layer when an

electric field is applied across it and the elastic transfer of this strain to the magnetostrictive nanomagnet will rotate the magnetization of the nanomagnet via the well-known Villari effect (or the inverse magnetostriction effect). A schematic of this switch is shown in fig. 1.1. The maximum rotation angle of the magnetization is normally 90 degrees, but by engineering the stress pulse duration [1] or by applying uniaxial stress sequentially in two different directions [2, 3], full 180 degree rotation can be accomplished. This kind of nanomagnet switching scheme is predicted to be minimally dissipative (at least one order of magnitude less dissipative than other magnet switching schemes) and hence very desirable.
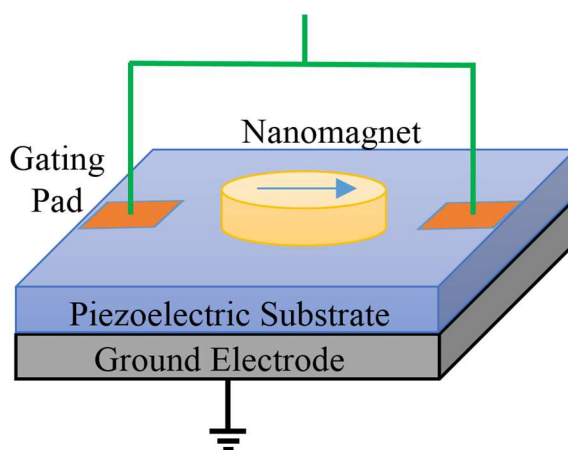


Fig. 1.1: Schematic of gating the nanomagnet delineated on top of piezoelectric substrate using external electric field.

Unfortunately, straintronic switching has an Achilles heel in that it is very error prone. The switching error probability is typically $>10^{-9}$ at room temperature [4], whereas for CMOS, this figure is less than $10^{-15}$. Another disadvantage that afflicts nanomagnetic switches in general is that they are usually integrated into a construct known as "magneto-tunneling junction" (MTJ). The MTJ has two ferromagnetic layers – one "hard" and the other "soft" – with a tunneling barrier interposed between them. A typical MTJ structure is shown in figure 1.2. The hard layer has a fixed magnetization and the soft layer's magnetization is free to rotate. It can be rotated with strain

if the MTJ is fabricated on a piezoelectric film, with the soft layer in elastic contact with the piezoelectric. The resistance of the MTJ is low when the two ferromagnetic layers have mutually parallel magnetizations and high when the magnetizations are antiparallel. The resistance of the MTJ can be switched between the high value (encoding one binary bit) and the low value (encoding the other binary bit) by rotating the magnetization of the free layer with strain to align antiparallel and parallel to the magnetization of the hard layer, respectively.
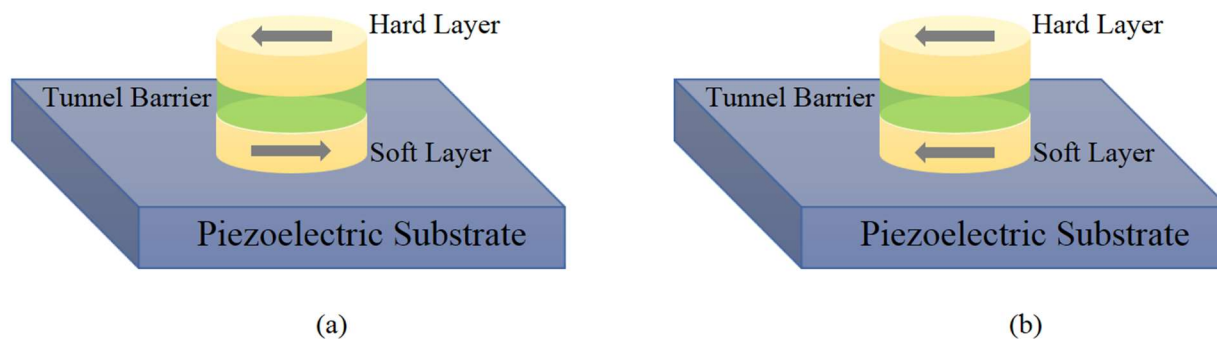


Fig. 1.2: Schematic of MTJ structure (a) high resistance state, (b) low resistance state.

The MTJ has the advantage of being an extremely energy-efficient switch because the switching action does not require current flow through the MTJ, but its disadvantage is that the ratio of the off-to-on resistance is relatively small (the maximum demonstrated at room temperature at the time of this writing is only ~7:1) [5] which is much smaller than the ratio of ~$10^5$:1 routinely found in CMOS transistors. Thus, nanomagnetic switches have two drawbacks: poor off/on ratio of the switch's resistance and the high switching error probability (poor reliability as a switch). Fortunately, there are some applications which are forgiving of poor off/on ratio and poor reliability. In those applications, MTJs can excel because of their potentially high energy-efficiency and non-volatility. One of them is image processing, which can benefit from replacing transistors with MTJs since the latter can reduce the energy dissipation per function and also retain the pixel information of a processed image owing to non-volatility. We have designed and

simulated a black and white application-specific image processor implemented with a two dimensional periodic array of MTJs where the pixel color (black or white) is encoded in the resistance state (on or off) of the MTJ [6]. This is a hardware based image processing scheme which is extremely fast (because no software and execution of instruction sets are involved) and energy efficient. Image pixels are encoded into the MTJ resistance states by first converting the pixel brightness (white or black) into voltage states with photodetectors (white = high voltage and black = low voltage) and then using the two different voltage levels to generate tensile and compressive stresses in the soft layer of the MTJ. Tensile stress will orient the soft layer's magnetization in one direction and compressive stress in another direction, so the two voltage levels (or equivalently the two pixel colors) will be mapped into two resistance states of the MTJ. When the input image pixels are mapped into the MTJ resistance states, the system goes into an excited state because dipole interactions between the soft layers of neighboring MTJs will prefer a certain arrangement of magnetizations which will not conform to the input pixels. This places the system in an excited state. The system cannot spontaneously decay to the ground state because of energy barriers within the soft layers of the MTJs (caused by their shape anisotropy). In other words, the system is stuck in a metastable state. A global stress erodes the energy barriers in every MTJ's soft layer and allows the system to reach the system ground state where the magnetizations of the soft layers (and hence the resistance states of the MTJs) assume different values. The pixel colors corresponding to the ground state MTJ resistances constitute the processed (output) image. Not any arbitrary processing can be accomplished using this (all hardware based) paradigm, but there are certain important image processing functions (e.g. edge enhancement detection) that can be implemented in this fashion. Note that no software is involved and it is the physics of interaction between the magnetization states of neighboring soft layers that elicits the image processing

activity. The global stress, which triggers the image processing action, can be generated with a voltage dropped across the piezoelectric substrate on which the MTJs are fabricated. An image containing an arbitrary number of black and white pixels can be processed in this fashion in few nanoseconds with very low energy cost. This (theoretical) project has been completed and published [6].

We have also studied theoretically switching errors that occur in strain-switched elliptical nanomagnets with in-plane magnetic anisotropy. This work was motivated by the experimental observation that straintronic switching is error-prone. The error rate found experimentally exceeds those calculated theoretically by several orders of magnitude. One possible explanation for thjs is that theoretical simulations assume ideal defect free nanomagnets, while real nanomagnets have structural defects which may strongly impact switching error probability. We examined theoretically the effect of material defects (such as voids, thickness variations, etc.) on switching errors of nanomagnets and found that defects increase the switching error rates dramatically [7]. This study revealed that straintronic switching is not robust against material defects. Curiously, for any type of defect, there is a critical stress value that minimizes the switching error probabilities [7]. This stress value is low enough in nanomagnets made of highly magnetostrictive materials, but may be too high to generate in nanomagnets made of materials with low magnetostriction. We have examined two different magnetostrictive materials: Terfenol-D and Cobalt, for both defect-free and defective nanomagnets, in case of static stress. We found that *localized* defects (such as a small hole or hillock) are more forgiving than *delocalized* (extended) defects such as thickness variation across a significant fraction of the nanomagnet surface. Finally, similar analysis is done for sinusoidal time varying stress generated by a surface acoustic wave and it and it was found that

time-varying stress application can reduce the switching error probability compared to constant stress for most cases [8].

In Chapter 4, several features of resonant spin wave modes in a nanomagnet (frequencies, magnetic field dependence of the frequencies, number of resonant modes) are studied in the presence of defects associated with thickness variations in the plane of the nanomagnets[9]. Here, it is observed that defects have a dramatic effect on spin wave modes: generating multiple frequencies of resonant spin wave modes, shifting the bias dependent frequencies, quenching of some frequencies etc. All these have serious consequences for many applications that rely on spin wave modes. There are some applications that have little tolerance for variations of spin wave frequencies, or their phase profiles – e.g. phase locked nano-oscillators for neuromorphic computing – and they are especially vulnerable. This study reveals that these applications will require almost defect-free nanomagnets.

In Chapter 5, challenges in designing nanomagnet based stochastic binary neurons (BSN) are studied. Because nanomagnetic switches are error-prone, they are not suitable for traditional Boolean computing hardware, but could be well-adapted to non-Boolean computing such as neural networks, probabilistic computing, belief networks, etc. Recently, probabilistic computing based on stochastic binary neurons has attracted much attention. Binary neurons are actually a class of probabilistic computing devices implemented using low barrier magnets (LBM). The term low barrier implies that the energy barrier separating the two stable magnetization states is purposely made small enough that thermal noise can make the magnetization fluctuate randomly with time. The random magnetization distribution can be utilized for computation. Recently the design of LBMs for binary stochastic neurons (BSN) is studied[10] and two important parameters that govern the BSN operation are highlighted as crucial parameters for design : the correlation time

$\tau_c$ , which is the *full width at half maximum* of the temporal autocorrelation, and the pinning current $I_p$, the spin-polarized current needed to pin the magnetization in the direction of the spin-polarization of the current due to spin transfer torque within a specified time. The response time of BSN is controlled by the correlation time. We found that in real LBMs, there are some design challenges due to *fabrication defects* which ultimately make of $\tau_c$ and $I_p$ defect sensitive [11]. Variation in $\tau_c$ and $I_p$ due to different types and location of defects make the design of LBMs for BSNs extremely challenging since $\tau_c$ and $I_p$ would become unpredictable. This may eventually impact the BSN applications of LBMs and make LBMs unsuitable for BSNs. This study is carried out to examine this possibility and different material defects are studied which mimic the imperfections found in actual nanomagnets fabricated using Electron Beam Lithography and E-beam Evaporation in our lab. We also calculate, the power spectral densities (PSDs) of magnetization fluctuations in LBMs to determine how sensitive they are to defects and small variations in shape that result in small variations in barrier height within the nanomagnet.

In Chapter 6, a Microwave Oscillator, based on the complex interplay between the strain anisotropy, shape anisotropy, dipolar magnetic field between soft and hard layer and spin transfer torque generated by the passage of spin polarized current through the soft layer, is studied theoretically [12]. This is a new analog application of magnetic devices to implement an oscillator with reduced footprint and cost compared to conventional oscillator based on operational amplifiers, capacitors and resistors. The designed oscillator exhibits narrow bandwidth, the oscillations are spectrally pure (almost sinusoidal) and the quality factor is ~5 times higher than that of spin torque nano-oscillators which will lead to higher radiation efficiency for antenna applications.

In Chapter 7, Probabilistic Computing based on Magneto Tunneling Junctions (MTJs) to generate

tunable correlation between two random bits streams is studied [13]. This is critical for graphical probabilistic circuit models which are more powerful than deep learning models, but require "programmable stochasticity". Traditional electronic implementation of a programmable correlator would require several components, but we have realized it with two dipole coupled magneto-tunneling junctions with magnetostrictive soft layers, fabricated on a piezoelectric substrate. The correlation can be tuned continuously between no correlation and perfect anti-correlation with an external voltage, which is convenient.

The study of ultrafast magnetization dynamics in a single magnetostrictive nanomagnet [14] is described in chapter 8. The nanomagnet is fabricated on a a poled (001) PMN-PT (piezoelectric) substrate using Electron Beam Lithography, e-beam evaporation and lift-off in our lab and further characterized by scanning electron microscope and magnetomotive force microscopy. The magnetization of the nanomagnet is made to precess by the combined effect of periodic strain and a bias magnetic field and the precession is monitored using time-resolved magneto-optical Kerr effect (TR-MOKE) measurements. The TR-MOKE measurement measures the time evolution of the polarization and intensity of reflected light from the nanomagnet. A pump beam of ~100 femtosecond pulse width causes the excitation of time varying strain in a piezoelectric substrate (on which the nanomagnet is deposited) due to the intense electric field (~1 MV/m) in the beam. This strain causes the magnetization of the nanomagnet to precess and that emits spin waves. The magnetization precession also causes the polarization and intensity of the light reflected from the magnet (the incident light is from a probe beam) to oscillate in time (Kerr oscillations). The Kerr oscillation frequency is correlated with the precessional frequency. A magnetic field is also present to induce Larmor precession of the magnetization. Thus, the precession is a combined effect of periodic strain and the bias magnetic field.

A probe beam periodically samples the magnet's reflectivity and the polarization (Kerr Signal) of the reflected light as a function of the delay between the pump and the probe to investigate the ultrafast magnetization dynamics. The observed spin wave modes associated with the magnetization precession are a mix of precessional motion around the bias magnetic field and the precessional motion induced by strain. The frequencies of these modes are in the neighborhood of 10 GHz, corresponding to ~100 ps time scale dynamics. The power and phase profile of the spin wave modes are also calculated from the data extracted from both experiment and simulation. The results obtained here for ultrafast magnetization dynamics in magnetostrictive nanomagnets subjected to periodic strain could be important in future implementation of ultrafast switching in straintronic magnetic storage and logic devices.

In chapter 9, a hardware emulation of simulated annealing in an interacting many body system is studied both theoretically and experimentally. If we have a two-dimensional arrangement of closely spaced elliptical nanomagnets with in-plane magnetic anisotropy, whose major axes are aligned along columns and minor axes along rows, then the dipole coupling will make the magnetic ordering "ferromagnetic" along the columns and "anti-ferromagnetic" along the rows. Noise and other perturbations can drive the system out of this ground state configuration and pin it in a metastable state where the magnetization orientations will not follow this pattern. Internal energy barriers, sufficiently larger than the thermal energy kT, will prevent the system from leaving the metastable state and decaying spontaneously to the ground state. These barriers can be temporarily eroded by globally straining the nanomagnets with time-varying strain if the nanomagnets are magnetostrictive, which will allow the system to return to ground state after strain is removed. This is a hardware variant of simulated annealing in an interacting many body system. Here, we demonstrate this function experimentally.

In chapter 10, a sub-wavelength "acoustic antenna" composed of magnetostrictive nanomagnets deposited on a piezoelectric substrate is demonstrated experimentally. It is actuated by spin-orbit torque from a platinum nanostrip that the nanomagnets are in contact with. Passage of alternating current through the nanostrip periodically flips the magnetizations of the nanomagnets because of the giant spin Hall effect. Because the nanomagnets are magnetostrictive, they expand/contract during the flipping, setting up alternating tensile and compressive strain in the piezoelectric substrate underneath. This leads to the generation of a surface acoustic wave. The measured radiation efficiency of the antenna is ~1%.

This thesis is a study of straintronic switches and is intended to lay the groundwork for a system of devices and components utilizing strain-switched nanomagnets for energy-efficient information processing. At the same the presence of defects and surface roughness variations in those nanomagnets are studied extensively in order to understand the different aspects contributing to different possible applications.

# Chapter 2: Image Processing using Dipole Coupled Magnetostrictive Nanomagnets

Hardware based image processing can be extremely fast and yet consumes little energy. Here, a magnetic system is proposed and analyzed for this purpose and it is shown that it can carry out specific image processing tasks in a few nanoseconds while consuming miniscule amount of energy. The choice of nanomagnets for image processing is motivated by the desire for energy efficiency. Traditional hardware platforms for image processing employ field-programmable gate arrays [15], diodes [16], nanowires [17] or quantum dots [18]. The image processing function is implemented via charge exchange between these elements, which always results in current flow and associated $I^2R$ power loss. In contrast, no current has to pass through nanomagnets in an image processing function, which eliminates the $I^2R$ loss in the device. Furthermore, the interaction between nanomagnets is "wireless" (no physical wires connect one nanomagnet to another) and is mediated by dipole interaction. Hence there is no energy loss in interconnects either, which further improves the energy efficiency. These considerations make nanomagnetic systems a very attractive choice for image processing.

## 2.1 Working Principle of Image Processing

Images containing only black and white pixels are considered only. We encode these two pixels colors, we need to have only two stable magnetization orientations which is easily achieved using nanomagnets in the shape of elliptical disks. A static fixed magnetic field is directed along the minor axis of the ellipse as shown in Fig. 2.1(a). That will ensure that the nanomagnet's magnetization will have only two stable orientations in the ellipse's plane as shown in Fig. 2.1 [19]. The angle φ between them is a function of the strength of the magnetic field and the eccentricity of the ellipse. It can be adjusted to ~90° by tuning the magnetic field strength [19][20]. Next consider a two-dimensional array of nanomagnets in a global magnetic field directed along the ellipses' minor axes as shown in Fig. 2.1(b).
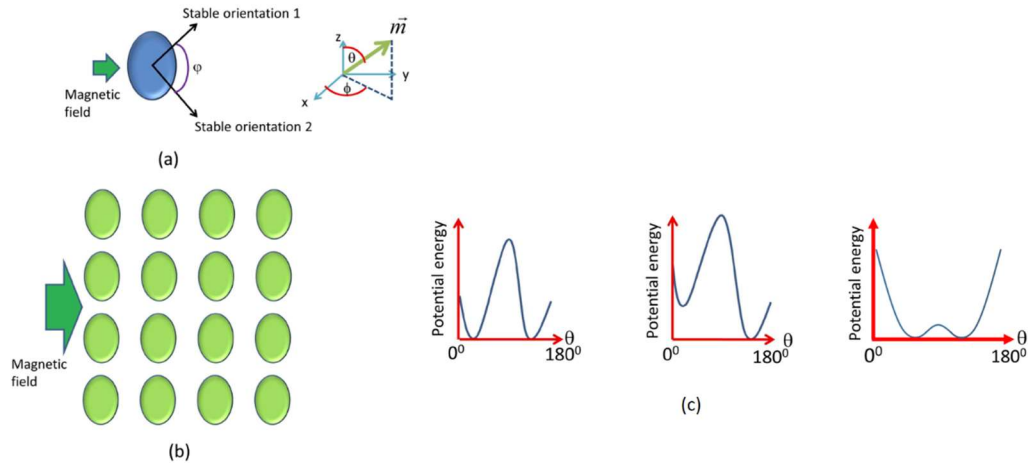
Fig. 2.1: (a) An isolated elliptical nanomagnet, placed in a magnetic field directed along the minor axis of the ellipse, has two stable magnetization orientations that are equally preferred. The angle φ between them can be adjusted by varying the strength of the magnetic field. (b) A two-dimensional array of elliptical nanomagnets in a global magnetic field. Dipole interaction makes one stable orientation preferred over the other and which is the preferred orientation is determined by the orientations of the neighbors. (c). Potential profile of an isolated nanomagnet(left), dipole coupled nanomagnets(center) and isolated nanomagnet in presence of external global magnetic field along minor axis.

Each nanomagnet will now experience a dipole field due to dipole interaction with its neighbors. This field depends, among other things, on the nanomagnet's own magnetization state, as well as the states of its neighbors. The effect of the dipole field on any nanomagnet is to make one of the two stable magnetization orientations preferred over the other. Therefore, the preferred color (black or white) of the pixel encoded in any nanomagnet will be dictated by the colors of the surrounding pixels. This dependency results in specific image processing functions which requires a nanomagnet to transition to its preferred magnetiztion orientation. However, this does not happen automatically. For the nanomagnet's magnetization to reorient in the more preferred direction, it must be able to transition to the lower energy minimum. That may not happen if there are energy barrier(s) separating the higher (local) energy minimum from the lower (global) energy minimum. In that case, an external agent must be employed to erode the energy barrier(s) temporarily and allow the system to migrate to the lower energy state, thus completing the image processing function. The external agent acts as a "clock" to trigger the image processing activity.

## 2.2 Stress as the Triggering Agent

Many external agents can act as the clock. However, the most energy-efficient clocking agent is mechanical strain [21][22] which lowers the potential barrier between the stable magnetization orientations in a magnetostrictive nanomagnet and switches the magnetization from the non-preferred orientation to the preferred one in the presence of inter-magnet dipole interaction. Strain is generated in the following way. The nanomagnets are delineated on a piezoelectric substrate and a voltage is applied across the latter with electrodes delineated on the surface of the substrate. By placing the electrodes in an appropriate fashion, one can generate biaxial strain (tensile along the major axis of the elliptical nanomagnet and compressive along the minor axis, or vice versa, depending on the polarity of the voltage). This strain is partially or wholly transferred to the nanomagnets and reorients each one's magnetization to the preferred direction [23]-[25], thus completing the image processing action.

## 2.3 Material Used

The magnetostrictive nanomagnets (soft layers of the MTJ) in this study are assumed to be made of Terfenol-D which is among the most magnetostrictive materials known. The dimensions of the elliptical nanomagnets are 100 nm (major axis), 60 nm (minor axis) and 16 nm (thickness). Table 2.1 lists the properties of the nanomagnets.

Table 2.1

NANOMAGNET PARAMETERS [26][27][28][29]

| Symbol | Quantity | Value |
|--------|----------|-------|
| $M_s$ | Saturation Magnetization | $8 \times 10^5$ A/m |
| A | Exchange Parameter | $9 \times 10^{-12}$ |
| $\lambda_s$ | Magnetostriction Coefficient | 600 ppm |
| B | Global Magnetic Field | 82 mT |

The magnetization orientation of a nanomagnet (or, equivalently, the pixel color encoded in that nanomagnet) is designated by the angle θ subtended with the major axis of the ellipse. If the z-axis is along the major axis of the ellipse and the y-axis is along the minor axis, then in spherical coordinates, θ is the polar angle and we will call the azimuthal angle φ. For the nanomagnet dimensions and the magnetic field strength given in Table 2.1, the two stable magnetization orientations are computed to be ( θ = 48.6˚, φ =90˚ ) and ( θ = 131.4˚ , φ = 90˚ ), shown in figure 2.1(c), following the method of [19]. The angular separation between them ( φ ) is 82.8˚ . These two orientations will encode "black" and "white", respectively. The color "black" is encoded in the θ = 48.6˚ state and the color "white" in the θ = 131.4˚ state.

## 2.4 Results and Discussion

Now, consider a black segment of an image consisting of 7 × 7 pixels where every, except one, pixel is black and the errant pixel is white. The white pixel represents noise or defect in the black segment of the image. The pixels are mapped into a 7 × 7 array of nanomagnets shown in Fig. 2.2(a) [using the writing scheme described later] where the vertical separation between the centers of two nearest neighbor nanomagnets is 150 nm and the horizontal separation is 285 nm.

Because of dipole interaction from the neighbors, the potential energy profile of the errant nanomagnet looks like that in Fig. 2.2(b), where the θ = 48.6˚ state is actually slightly lower in energy than the θ = 131.4˚ state and there is an energy barrier of 4.6 kT at θ = 90˚ separating the two minima. The dipole interaction has lifted the degeneracy of the two stable states and made the "black" state preferred over the "white". Dipole interaction actually also changes the two stable orientations slightly from θ =48.6˚, 131.4˚. But since this is a small effect, it will be continued to label the stable orientations as θ ≈ 48.6˚ and θ ≈ 131.4˚ states. It can be expected that the errant nanomagnet would prefer to migrate to the lower energy state and the corrupted white pixel would

spontaneously turn black, thereby auto-correcting and eliminating noise by virtue of the dipole interaction. This actually does happen in this case since the energy barrier separating the two minima is a mere 4.6 kT and thermal fluctuations can transcend this barrier. Therefore, the corrupted pixel auto-corrects.
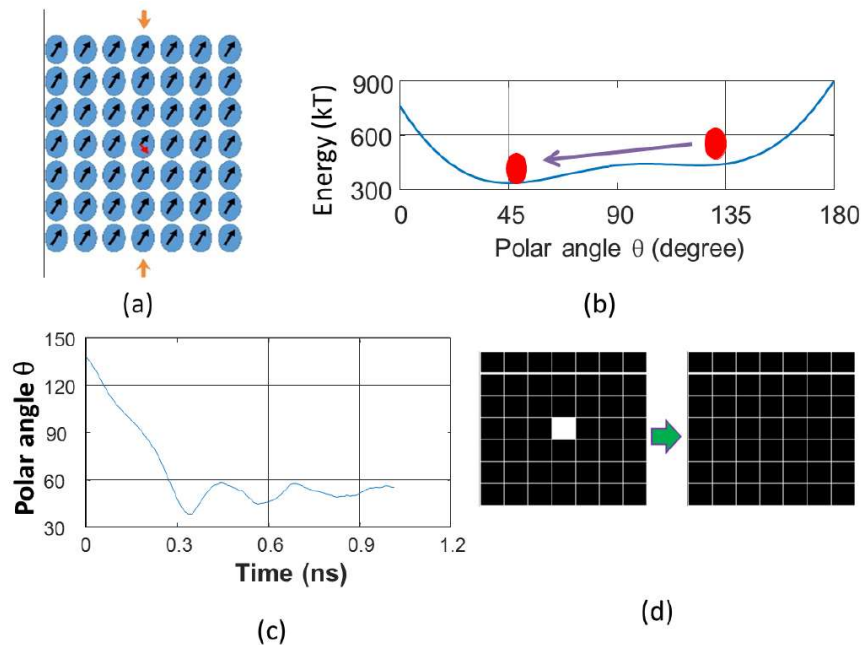


Fig. 2.2: (a) A 7 × 7 array of nanomagnets storing a 7 × 7 array of pixels (not to scale). All pixels are black except the one in the center which has turned white due to noise. (b) The potential energy profile of the errant nanomagnet in the presence of dipole interaction with the neighbors. The degeneracy between the two minima has been lifted by dipole interactions. (c) Thermal fluctuations are able to take the errant nanomagnet to the global minimum in ~0.4 nanoseconds without the application of any stress. (d) The corrupted white pixel spontaneously turns black, thereby automatically removing the noise.

However, this would not have happened if the barrier were much higher than 4.6 kT. In that case, the nanomagnet would have remained stuck in the higher energy metastable state (white pixel) and could not decay to the ground state (black pixel), thereby preventing error correction. This kind of situation is shown in fig. 2.3, where the spin textures of nanomagnets in a 7 × 7 array corresponding to the black segment ( 7 × 7 pixels) of an image is shown where two vertically neighboring pixels in the fourth column have been corrupted and become white.

In this case, thermal fluctuations alone cannot auto-correct the errant pixels since the barrier separating the two energy minima in the potential profiles of these two nanomagnets is too high for thermal fluctuations to overcome. However, application of a global compressive stress of magnitude 10.5 MPa along the major axes of the ellipses suppresses the energy barriers and rotates the magnetization of every nanomagnet. The stress adds an extra term to the potential energy of every nanomagnet: $E_{stress} = -(3/2) \lambda_s \sigma \Omega \cos^2\theta$ , where $\lambda_s$ s is the magnetostriction coefficient of the magnet (it is a positive quantity for Terfenol-D), $\sigma$ is the stress (positive for tension and negative for compression) and $\theta$ is the angle between the stress axis and magnetization, which also happens to be the polar angle of the magnetization vector. This energy term is minimum when $\theta = 90°$, which means that compressive stress would remove the energy barrier at $\theta = 90°$ and allow the corrupted pixel to auto-correct. Subsequent removal of stress changes the magnetization states of the two errant nanomagnets only, so the colors of the two corrupted pixels are restored to approximately the right color while the colors of the uncorrupted pixels are left practically intact.
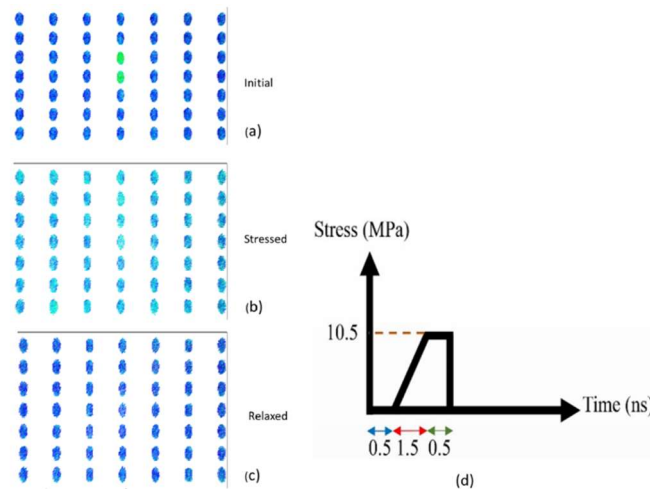


Fig. 2.3. (a) Spin texture of a 7 × 7 pixel array representing the black segment of an image where two consecutive pixels in the fourth column are of the wrong color. (b) Spin textures of the array after application of 10.5 MPa of compressive stress along the major axes of the ellipses. (c) Spin textures after withdrawal of stress showing that the errant pixels are no longer white. All pixels have turned approximately black. (d) the applied stress profile in time.

The micromagnetic simulations to obtain the results in Fig.2.3 were carried out with the MuMax3 package [30]. The cell size used in the simulation was progressively decreased until the results became independent of cell size. This cell size was 3 nm × 3 nm × 2 nm. Since the applied stress is global, it affects every nanomagnet in the array. Therefore, every pixel changes color - the corrupted ones change significantly from white to near-black, while the uncorrupted ones change slightly from black to near-black. In Fig. 2.4, we show the time evolutions of the magnetization orientations (polar angle θ) of the two nanomagnets encoding the corrupted pixels, as well as that of a nanomagnet encoding an uncorrupted pixel. The applied stress profile is shown in Fig. 2.3(d).



Fig. 2.4: Temporal evolution of the magnetization orientation of the (a) bottom and (b) top errant nanomagnet in Fig. 5 from θ ≈ 48.6˚ to θ ≈ 48.6˚. Since the magnetic field due to thermal noise is random, we ran six different simulations for each of the two nanomagnets. The six switching trajectories vary slightly but all result in transitioning to the correct pixel color corresponding to θ = 48.6˚. (c) The temporal evolution of the magnetization of the nanomagnet in the top right corner (row 1, column 7) in Fig. 2.3. This nanomagnet corresponds to an uncorrupted pixel, but because it too is subjected to global stress and thermal noise, its magnetization changes with time. However, it returns to its original state after a brief sojourn showing that the stress does not corrupt an uncorrupted pixel. The time to settle (image processing time) is ~3 nanoseconds.

Note that the uncorrupted nanomagnet returns close to its original state of $\theta = 48.6°$ after completion of the stress cycle while a corrupted one changes significantly from $\theta \approx 131.4°$ to $\theta \approx 48.6°$. The switching trajectories shown in Fig. 2.4 will vary from one run to another of the MuMax3 simulation because the field acting on the nanomagnets due to thermal noise is random in time. That is why we have plotted six different traces, each corresponding to a different simulation run. Although the trajectories vary somewhat because of thermal noise, each trajectory inevitably results in successful evolution of the errant nanomagnet from $\theta \approx 131.4°$ to $\theta \approx 48.6°$. These simulations are also repeated for the converse situation when the two corrupted pixels are black and the surrounding ones are white (this would correspond to the white segment of an image). The black pixels turn nearly white after stress application and the white pixels remain nearly white, showing that error correction is independent of pixel color.

In Fig. 2.5(a), it is shown that if an entire row is corrupted, then the application of global stress along the major axes of the elliptical nanomagnets can correct the corrupted row. In Fig. 2.5(b), it is shown that the same is true if two consecutive rows are corrupted. In Figs. 2.5(c) and 2.5(d), it is shown that this scheme can even correct two non-consecutive rows, regardless of whether the corrupted pixels are black or white. In Fig. 2.6, it is shown that even if random pixels are corrupted, as long as the corrupted pixels are a minority, application and withdrawal of global stress can correct the corrupted pixels. In Fig. 2.7, it is shown that if an image has two segments such that in one segment black pixels dominate and in the other white pixels are more abundant, then application of global stress turns the first segment all-black and the second segment all-white. This enhances the contrast between the two segments and sharpens the edge between them.

There are some cases where the approach fails, an example of which is shown in Fig. 2.8. What causes the failure in this case is the nature of dipole coupling. If the line joining the centers of two

nanomagnets is collinear with their major axis, then dipole coupling will tend to make their magnetizations mutually parallel (ferromagnetic ordering), whereas if that line is collinear with the minor axis, then dipole coupling will make their magnetizations anti-parallel (ant-ferromagnetic ordering).



Fig. 2.5: (a) Spin textures of an array of 7 × 7 nanomagnets representing white segment of an image where the entire fourth row has been corrupted and turned black. Application and subsequent withdrawal of global stress along the major axes corrects the corrupted row. (b) An array of black pixels in the black segment of an image where two consecutive rows have been corrupted and turned white. Stress application and withdrawal corrects both corrupted rows. (c) An array of white pixels where two non-consecutive rows have been corrupted and turned black. A stress cycle corrects both rows. (d) An array of black pixels where two non-consecutive rows have been corrupted and turned white. Again, a stress cycle corrects both rows.

Pre-stress     Under stress     Post stress

Fig. 2.6: A 7 × 7 array corresponding to the black segment of an image with randomly corrupted pixels (black pixels turned white). Application and subsequent removal of global stress applied along the major axes of the elliptical nanomagnets corrects the corrupted pixels and turns them all black.



Pre-stress     Under stress     Post-stress (relaxed) Edge-enhanced



Stress and withdraw
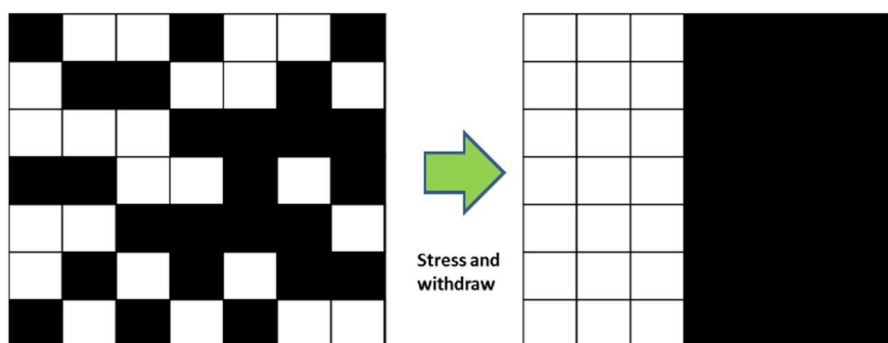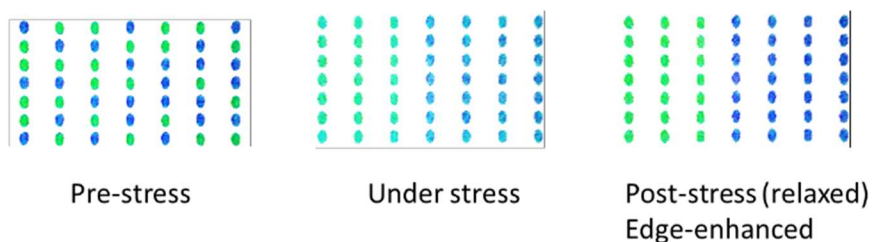
Fig. 2.7: Edge enhancement detection. The left segment (three columns) has majority white pixels and the right segment (four columns) has majority black segments. After application and removal of global stress applied along the major axes of the elliptical nanomagnets, the white-dominant segment turns all-white and the black-dominant segment turns all-black. This enhances the edge and contrast between the two segments.



Pre-stress     Stressed     Post-stress
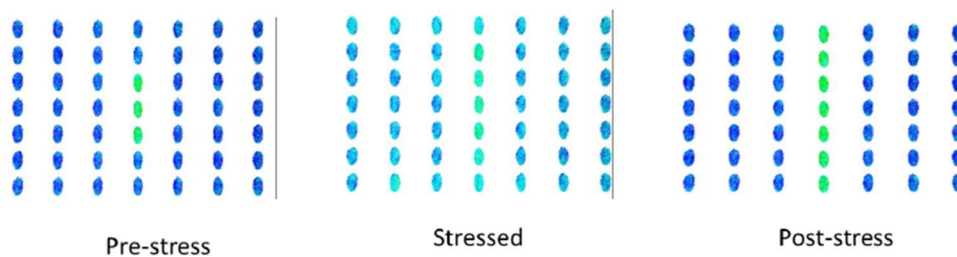
Fig. 2.8: Failure to correct pixels. The left panel shows a 7 × 7 array where three consecutive members of a column have been corrupted. Application and subsequent removal of global stress along the major axes of the ellipses corrupts the entire column.

The ferromagnetic coupling is stronger than the anti-ferromagnetic coupling [31]. Here, three consecutive errant nanomagnets are ferromagnetically coupled in the fourth column. There are two ferromagnetically coupled nanomagnets above and two below in that column which are in the correct state. The ferromagnetic coupling of the three in the incorrect states overwhelms that of the two above and two below in the correct state and ultimately corrupts the entire column to make it ferromagnetically ordered, i.e. every nanomagnet in the column is magnetized in the same direction, albeit the wrong direction. Thus, the approach fails in the rare case when consecutive pixels in a column are corrupted and the uncorrupted pixels above or below are fewer in number than the corrupted pixels.

## 2.5 Writing Pixel information in Nanomagnet

For this paradigm described to work, one must first be able to write pixel information into the magnetization states and then be able to read them. For the purpose of "writing", a skewed magneto-tunneling junction (MTJ) needs to be fabricated on top of the elliptical nanomagnet as shown in Fig. 2.9. The nanomagnet will act as the soft layer of the MTJ and the hard layer of the MTJ (implemented with a synthetic anti-ferromagnet) will be permanently magnetized along one of the two stable magnetization directions of the soft layer.
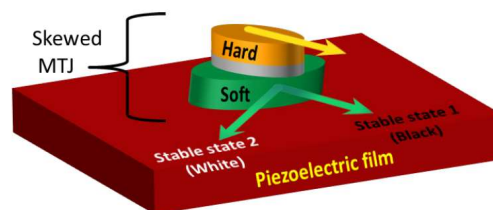


Fig. 2.9: A skewed magneto-tunneling junction whose soft layer has two stable magnetization orientations that correspond to black and white pixels. A magnetic field directed along the minor axis of the soft layer is present and not shown. The hard layer is permanently magnetized along one of the stable orientations. A black or white pixel state can be stored or written by applying a negative or positive voltage between the hard and soft layers with contacts not shown. The same contacts can be used to read the resistance of the MTJ and deduce the stored pixel color.

A negative potential applied between the hard layer and soft layer (negative polarity of the voltage source connected to the hard layer) will inject electrons from the hard into the soft layer and orient that latter's magnetization along that of the hard layer by spin-transfer torque. This will, say, write a black pixel state into the soft layer. Reversing the polarity of the potential will extract electrons from the soft layer into the hard layer and switch the magnetization of the soft layer to the other stable state, thus writing the white pixel. The actual pixel color can be converted to a voltage with a photodetector that generates a voltage proportional to the brightness (white pixels high voltage and black pixels low voltage). A level shifter then transduces a white pixel state to a positive voltage and a black pixel state to a negative voltage, resulting in direct conversion of pixel color to magnetization state. To "read" a stored pixel state, corresponding MTJ's resistance needs to be measured. A low resistance state will imply that the magnetizations of the hard and soft layer are parallel and hence the stored pixel is black, while a high resistance state will imply that the two magnetization states are approximately perpendicular and the stored pixel is white. Having established the read/write scheme, the next step is to proceed to discuss the image processing functionality.

## 2.6 Conclusion

In conclusion, a paradigm for removing image noise and edge enhancement detection using an array of dipole-coupled magnetostrictive nanomagnets is demostrated whose magnetizations are sensitive to stress. There is significant interest in all-hardware based image processing [9][10][11][12][31][32] because of the speed and convenience. The present system serves this purpose for specific applications. The time taken to complete the image processing tasks considered here is a few nanoseconds and will be relatively independent of image size (number of pixels) since corrupted pixels are corrected simultaneously and not sequentially, i.e. the processing

is parallel and not serial. Equally important, the energy dissipated to complete these tasks will be very small since very little energy is dissipated to switch the magnetization of magnetostrictive nanomagnets, delineated on a piezoelectric substrate, with electrically generated strain [33][34]. This results in an image processing paradigm with exceptionally low energy-delay product.

# Chapter 3: The Effect of Material Defects on Strain Induced Switching of Magnetostrictive Nanomagnets

Magneto-elastic (straintronic) switching of bistable magnetostrictive nanomagnets is an extremely energy-efficient switching methodology for (magnetic) binary switches that has recently attracted widespread attention because of its potential application in ultra-low-power digital computing hardware. Unfortunately, this modality of switching is also very error prone at room temperature. Theoretical studies of switching error probability of magneto-elastic switches have predicted probabilities ranging from $10^{-8} – 10^{-3}$ at room temperature for *ideal*, *defect-free* nanomagnets, but experiments with real nanomagnets show a much higher probability that exceeds 0.1 in some cases.

### 3.1 Motivation and Defect Modeling

Recent experiments on magneto-elastic switching has shown that the switching probability of magnetostrictive nanomagnets deposited on a piezoelectric substrate is relatively small when a voltage is applied to the piezoelectric to generate strain in the nanomagnets [3][34][35-37]. While there may be many reasons for the low switching rate, one obvious possibility is that material defects in the nanomagnets might impede switching. The difference between ideal nanomagnets and real nanomagnets is that the latter have structural defects acquired during the fabrication process. Fig. 3.1 shows atomic force micrographs of some Co nanomagnets fabricated in our lab. They are delineated on a piezoelectric substrate for magneto-elastic switching. These nanomagnets were fabricated by patterning a PMMA electron beam resist (spun on to the piezoelectric substrate) with e-beam lithography. The resist was developed and cobalt was evaporated within opened windows using electron beam evaporation, followed by lift off, to produce the nanomagnets. It is found that defects increase the switching error probability by *orders of magnitude* and this could at least partially explain why the error rates found in experiments vastly exceed those estimated from theoretical simulations of ideal specimens. This is a discouraging result and implies that unless pristine nanomagnets can be fabricated routinely, magneto-elastic switches may not be

suitable for Boolean logic and memory. This would temper some of the enthusiasm about magneto-elastic switches.
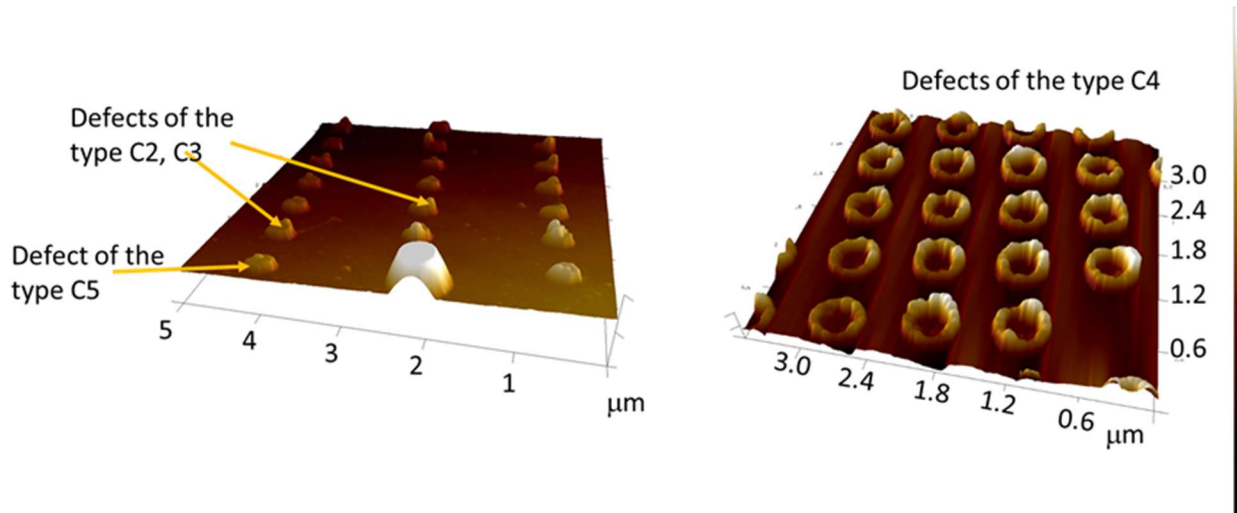


Fig. 3.1: Atomic force micrographs of nanomagnets showing the various types of thickness variations across the surface that can result from the fabrication process.

In all cases of fig. 3.1, thickness variations across the surface of the nanomagnets are observed. These variations are not specific to a given fabrication run, but show up in every run, although there are obviously slight variations between different runs. Some of them may be caused by the large surface roughness in piezoelectric substrates, which is typically ~ 3 nm. This is much worse than the surface roughness (< 0.3 nm) found in silicon substrates used to fabricate spin transfer torque memory. Unfortunately, magneto-elastic switches require a piezoelectric film or substrate which has a relatively large surface roughness. Thus, these defects might be unavoidable even under the most stringent fabrication control. We have classified the observed defects into six different classes, each one of which is approximated in the manner of Fig. 3.2.
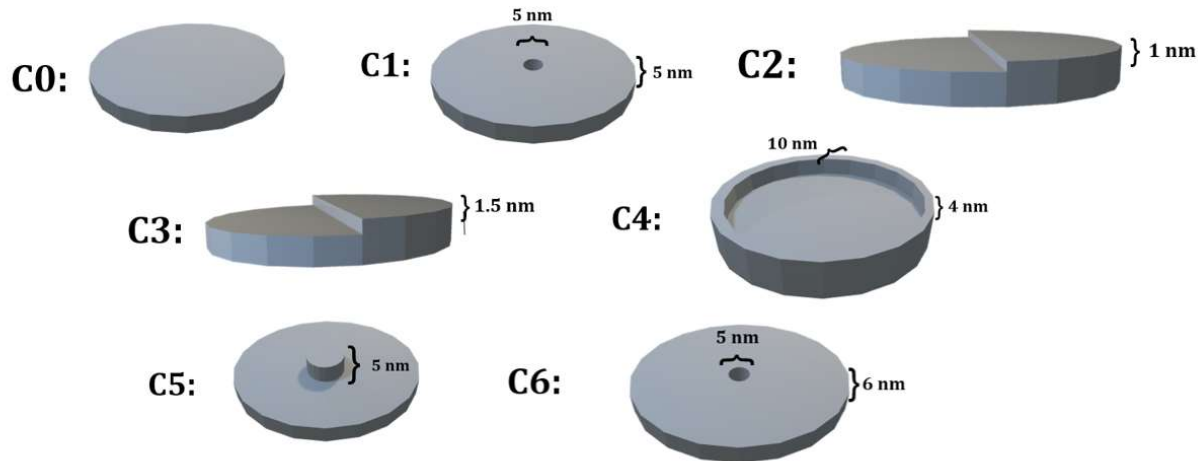
Fig. 3.2: The different types of thickness variations observed in Fig. 3.1 are approximated by six different configurations: C0 (no defect, an elliptical disk of major axis 100 nm, minor axis 90 nm and thickness 6 nm), C1 (a shallow hole 5 nm in diameter and 5 nm deep at the center, not observed in Fig. 3.1, but still commonplace), C2 and C3 (one half of the nanomagnet thicker than the other by 1 nm and 1.5 nm respectively), C4 (an annulus 10 nm thick and 4 nm high at the periphery; we kept the height and thickness uniform for ease of simulation. Later we show that this defect is the worst and increases the switching error probability dramatically. Introducing randomness in the height and thickness of the annulus will, if anything, exacerbate the error), C5 (a raised cylindrical region 5nm in diameter and 5 nm high), and C6 (a through hole 5 nm in diameter, not observed in Fig. 3.1).

At first, the role that material defects on switching failures is studied by simulating the effect of a physical void, or "hole", in the nanomagnet (one type of material defect, C6) on the switching probability in the presence of thermal noise.

## 3.2 Stress Induced Switching Dipole Coupled Nanomagnets

To begin with, the magneto-elastic switching of the magnetization of a magnetostrictive defect free nanomagnet in a dipole coupled pair of elliptical nanomagnets, one of which (left nanomagnet in Fig. 3.3) has higher eccentricity than the other is studied. The left nanomagnet is the "hard" nanomagnet because of its large shape anisotropy. It remains magnetized in one direction along its major axis and is not affected by (any reasonable amount of) stress since the stress anisotropy energy cannot overcome the large shape anisotropy energy in this nanomagnet and make its

magnetization rotate. The right nanomagnet is the "soft" nanomagnet whose magnetization can be affected by stress since it has a lower shape anisotropy energy barrier. The two nanomagnets are positioned such that the line joining their centers is collinear with their minor axes (hard axes). In this case, shape anisotropy would prefer that the magnetizations of the two nanomagnets lie along their major axes (easy axes) and dipole coupling between the two would prefer anti-ferromagnetic configuration such that the magnetizations of the two nanomagnets be mutually antiparallel.
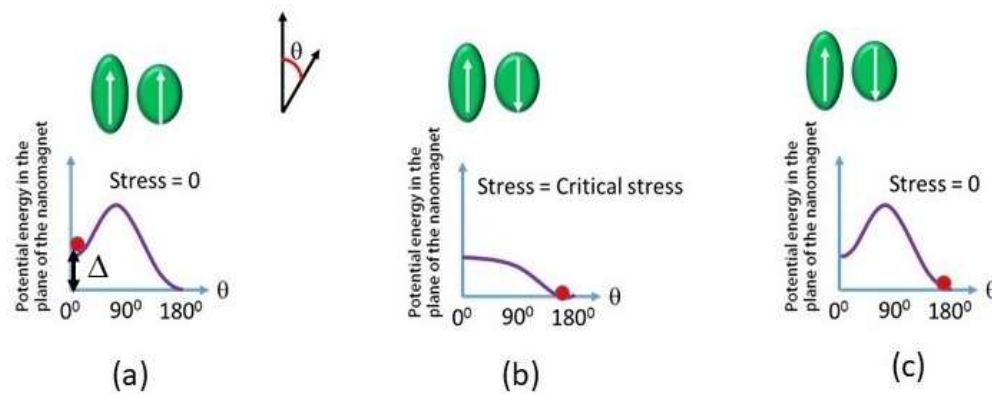


Fig. 3.3: (a) Two dipole-coupled elliptical magnetostrictive nanomagnets with in-plane anisotropy, the left more shape anisotropic than the right, are magnetized in the same direction along the easy axis with an external magnetic field. The potential profile of the right nanomagnet is shown under various stress conditions and the "ball" represents the state of the right nanomagnet determined by its magnetization orientation. The barrier in the potential profile is due to shape anisotropy and it is asymmetric due to dipole coupling with the left nanomagnet. When the right nanomagnet's magnetization is parallel to that of the left nanomagnet, the former nanomagnet is stuck in a metastable state and cannot transition to the ground state because of the intervening barrier; (b) the shape anisotropy energy barrier in the right nanomagnet is eroded (but not inverted) by applying *critical stress* (compressive or tensile) along the major axis. This allows the right nanomagnet to come out of the metastable state and reach the global energy minimum (ground state) and its magnetization flips to assume the antiparallel configuration; (c) the system remains in the global minimum state with the magnetizations antiparallel after stress is removed.

Let assume that both nanomagnets are magnetized in the same direction along their major axes with a strong magnetic field (Fig. 3.3(a)). This will place the soft nanomagnet in a metastable state. Its magnetization is aligned along the easy axis, but it is not the preferred orientation or lowest energy state since the magnetization is parallel (not antiparallel) to that of the hard nanomagnet.

The shape anisotropy energy barrier in the soft nanomagnet prevents its magnetization from flipping spontaneously and assuming the antiparallel orientation. Essentially, the energy barrier prevents the transition from the metastable state (parallel magnetizations) to the ground state (antiparallel magnetizations). This shape anisotropy energy barrier can be eroded by applying a critical stress that just erodes the barrier but does not invert it. The critical stress is the stress that makes the stress anisotropy energy equal to the energy barrier, and hence it is ideally defined by the relation $(3/2)\lambda_s\sigma_{crit}\Omega = E_b$ where $\lambda_s$ is the magnetostriction coefficient of the soft nanomagnet, $\Omega$ is the nanomagnet volume, $E_b$ is the shape anisotropy energy barrier and $\sigma_{crit}$ is the critical stress. The application of critical or super-critical stress will remove the energy barrier and allow the soft nanomagnet's magnetization to flip and assume the antiparallel orientation, thus transitioning the system from the metastable state to the ground state.

The application of "critical stress" actually results in more reliable switching than if "super-critical" (excess) stress is applied [38]. This is easy to understand. If excess stress is applied, then we would *invert* the potential barrier (instead of just eroding it), driving the system to the new energy minimum created at θ = 90º as shown in Fig. 3.4. Subsequent removal of stress would have more likely driven the system to the correct global minimum state at θ = 180º (because it is lower in energy than the local minimum state at θ = 0º), but still with some significant probability of going to the incorrect local minimum state at θ = 0º, as shown in Fig. 3.4, because the energy difference between the two states is only a few times $kT$ (for any reasonable dipole coupling strength). On the other hand, if critical stress is applied, then no energy minimum is ever created at θ = 90º (see Fig. 3.3) and hence the above problem does not arise. The energy minimum is created only at θ = 180º and therefore the probability of reaching the correct global minimum state

at θ = 180º is much higher than that in the case of super-critical stress [38]. Thus, tailoring the stress to the critical value is important for reliable magneto-elastic switching.
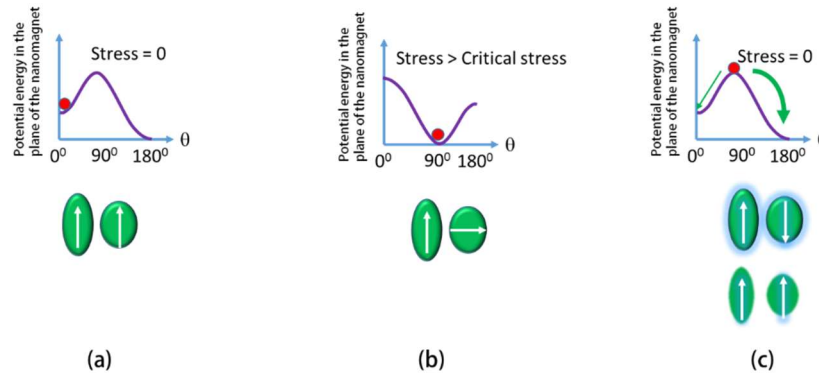


Fig. 3.4: (a) The right nanomagnet of Fig. 3.4 in the metastable state where its magnetization has been oriented parallel to that of the left nanomagnet by a magnetic field, (b) excess stress is applied to invert the shape anisotropy energy barrier and drive the magnetization of the right nanomagnet to the new energy minimum where it points along the minor axis of the ellipse (hard axis); (c) when stress is released, the magnetization of the right nanomagnet will prefer to align antiparallel to that of the left nanomagnet because of dipole coupling, but the probability of aligning parallel, albeit lower, is not small. Consequently, there is a significant probability of switching error if the nanomagnet is overstressed to "invert" the potential barrier as shown in Fig. 3.4(b).

The stress induced switching of the soft nanomagnet's magnetization to assume an orientation antiparallel to that of the hard nanomagnet implements the conditional dynamics of an inverter or a Boolean NOT gate. The magnetization orientation of the hard nanomagnet encodes the input bit and that of the soft nanomagnet the output bit. Since the ground state is the antiparallel configuration, the output bit is always the logic complement of the input bit as long as the system can migrate to the ground state. The stress acts as a "clock" to trigger the NOT operation by eroding the potential barrier and allowing the system to transition to the ground state. The operation of such a NOT gate, triggered by stress, or a surface acoustic wave, has been demonstrated experimentally [34, 39], but the switching probability as a function of stress magnitude has not been studied experimentally to test the hypothesis that critical stress produces the most reliable switching. The reason why it has not been studied is that the nanomagnets are usually stressed by

applying a voltage across an underlying piezoelectric thin film and they have relatively low endurance due to piezoelectric fatigue [40] and that makes it difficult to apply multiple cycles of stress to test the hypothesis.

Table 3.1 lists the critical stress values for a nanomagnet with a shape anisotropy energy barrier of 60 kT (room temperature) and volume 54000 nm$^3$ . We have assumed the bulk values of magnetostriction in amorphous materials. Materials with higher magnetostriction obviously require lower stress to switch.

Table 3.1: Material properties of Co, Ni, and Terfenol-D. Critical stress values for an elliptical nanomagnet with a shape anisotropy energy barrier of 60 kT and volume 54,000 nm$^3$. The magnetostriction values are taken from references [41, 42].

| Material | Magnetostriction ($\lambda_s$) (ppm) | Critical Stress (MPa) |
|---|---|---|
| Co | ~35 | 88.5 |
| Ni | ~35 | 88.5 |
| Terfenol-D | ~600 | 5.16 |

### 3.3 Stress Induced Switching of Defective Nanomagnets

When a material defect is present in a nanomagnet, the above analysis is more complex and the switching error probability changes drastically as the presence of defect greatly influences energy barrier of the nanomagnet. Here, defect type C6 is studied which is magneto-elastic switching in an elliptical magnetostrictive nanomagnet containing a material defect, e.g. a material void, implemented as a physical "hole" is studied. Initially it is assumed that a nanomagnet is in one of its stable orientations along the major axis (easy axis) and a magnetic field is applied in the opposite direction to make its magnetization flip as shown in fig. 3.5(a). The magnetic field however is too weak to overcome the shape anisotropy energy barrier separating the two stable orientations along the easy axis and hence uniaxial stress (of the correct sign) is applied along the

major axis of the ellipse to erode or invert the energy barrier and allow the nanomagnet to switch its magnetization to point in the direction of the magnetic field. The magnetic field can be viewed as the dipole coupling field due to the presence of a nearby elliptical nanomagnet whose major axis is parallel to the major axis of the test nanomagnet and the line joining their centers is collinear with their minor axes (i.e. the NOT gate). The switching of the magnetization of the test nanomagnet (with a hole in its center) due to the combined effect of the bias magnetic field and stress in the presence of thermal noise using the micromagnetic simulator MuMax3 [30] is studied. The procedure for incorporating stress and thermal noise in the simulations has been described in ref. [43].
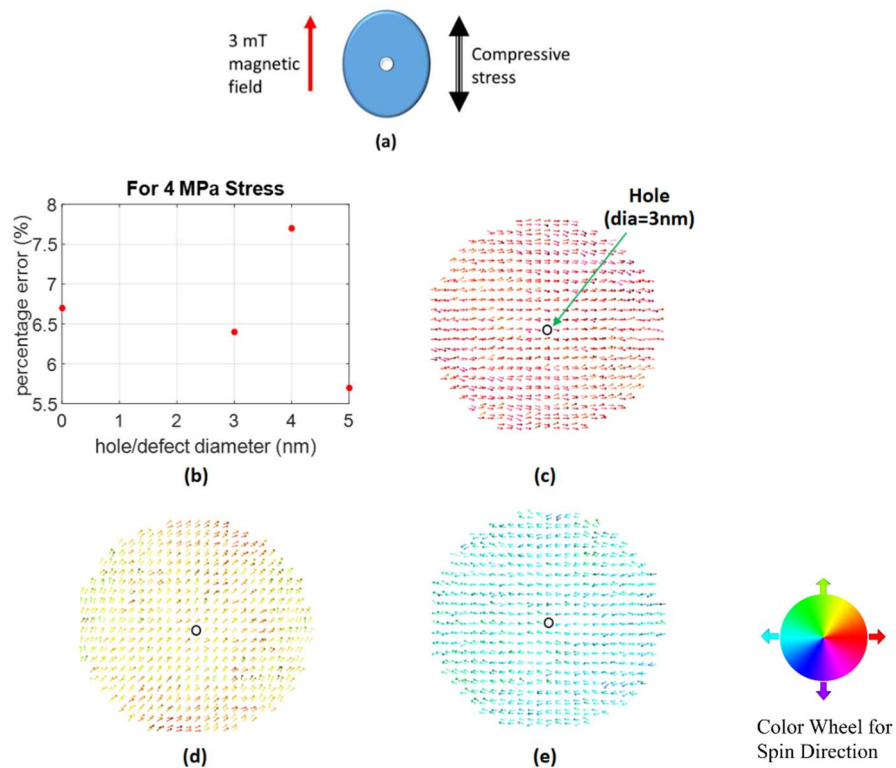


Fig. 3.5: (a) Nanomagnet with a hole at the center. A magnetic field of 3 mT is applied along the major axis to flip the magnetization and uniaxial compressive stress is also applied along the major axis to aid the flipping. (b) Switching error probability as a function of the hole diameter when the applied stress is 4 MPa; (c) Magnetization texture in the initial state (with a 3 nm diameter hole in the center); (d) Magnetization texture under a stress of 4 MPa; (e) Magnetization texture after release of stress.

The switching error probability is found as follows: At time $t = 0$, the magnetization points antiparallel to the bias magnetic field. We then turn on both the magnetic field and stress abruptly at time $t = 0$ and generate 1000 switching trajectories in MuMax3 under the combined effect of the bias magnetic field and stress. The simulations are carried out until each trajectory reaches a steady state and the magnetization aligns either parallel or antiparallel to the bias magnetic field. The time taken to reach steady state is ~1 ns. The fraction of trajectories that end up with the magnetization antiparallel to the magnetic field (fails to switch) is the switching error probability. The time step used in the simulations is 10 fs and the spatial resolution is 2 nm.

The test nanomagnet is assumed to be made of Terfenol-D and has major axis dimension 100 nm, minor axis dimension 90 nm and thickness 6 nm. The bias magnetic field has a flux density of 3 mT and uniaxial compressive stress is applied along the major axis to erode or invert the energy barrier in the nanomagnet. The critical stress for this nanomagnet is 2.26 MPa in the absence of the magnetic field (shape anisotropy barrier = 26.3 kT). The magnetic field will lower it to 0.78 MPa by lowering the barrier to ~9 kT.

A material defect is introduced in the form of a circular hole in the elliptical nanomagnet's center. The diameter of this hole is varied to study the switching error probability as a function of the hole diameter under three different stress magnitudes (sub-critical, near-critical and super-critical). The critical stress will be larger in the defective nanomagnet than in the defect-free nanomagnet since the energy barrier separating the two stable magnetization orientations is made larger by the hole (recall that the critical stress is proportional to the energy barrier). This happens because the energy barrier is due to shape anisotropy. The introduction of the hole makes the ellipse into an annulus and increases the effective shape anisotropy. Therefore, it is expected that the hole will increase the energy barrier and hence the critical stress.

## 3.4 Results and Discussion

The results of the simulations are shown in Figs. 3.5-3.8. In each of these figures, we show the switching error probability as a function of the hole diameter (0 nm, 3 nm, 4 nm and 5 nm) for stresses of 4 MPa (sub-critical), 8 MPa (near critical), 16 MPa (near critical) and 50 MPa (super-critical, excess stress).

The sub-critical stress is insufficient to make the stress anisotropy energy erode the energy barrier separating the two stable magnetization orientations in the presence of the 3 mT magnetic field, and hence, expectedly, the switching probability is small causing the error probability to be very large for sub-critical stress. The 8 MPa and 16 MPa stresses cause the minimum error probabilities – with or without the hole. Without the hole, none out of 1000 simulated switching trajectories failed to switch when 8 MPa or 16 MPa was applied, showing that the switching error probability is less than 0.1% for these two stress values in a defect-free nanomagnet. For a 3 nm diameter hole, the error probability is still less than 0.1% for 8 MPa stress (none of the 1000 trajectories failed to switch) and becomes 0.1% for 16 MPa stress (one out of 1,000 trajectories failed to switch). When the stress is increased to 50 MPa, the error probability increases for all hole diameters, showing that there is an optimum stress (for lowest switching error probability) even when there is a material defect (e.g. a physical hole) in the nanomagnet, except it is much higher in a defective nanomagnet than in a defect-free nanomagnet (recall that the calculated critical stress in a defect-free nanomagnet is 0.78 MPa).
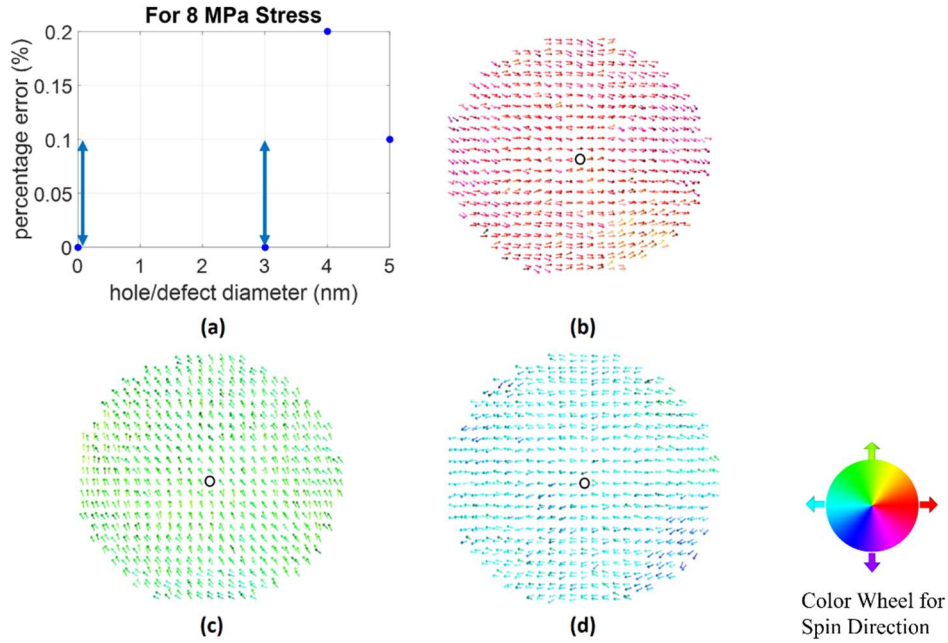
Fig. 3.6: (a) Switching error probability as a function of the hole diameter when the applied stress is 8 MPa; (b) Magnetization texture in the initial state (with a 3 nm diameter hole in the center); (c) Magnetization texture under a stress of 8 MPa; (d) Magnetization texture after release of stress.
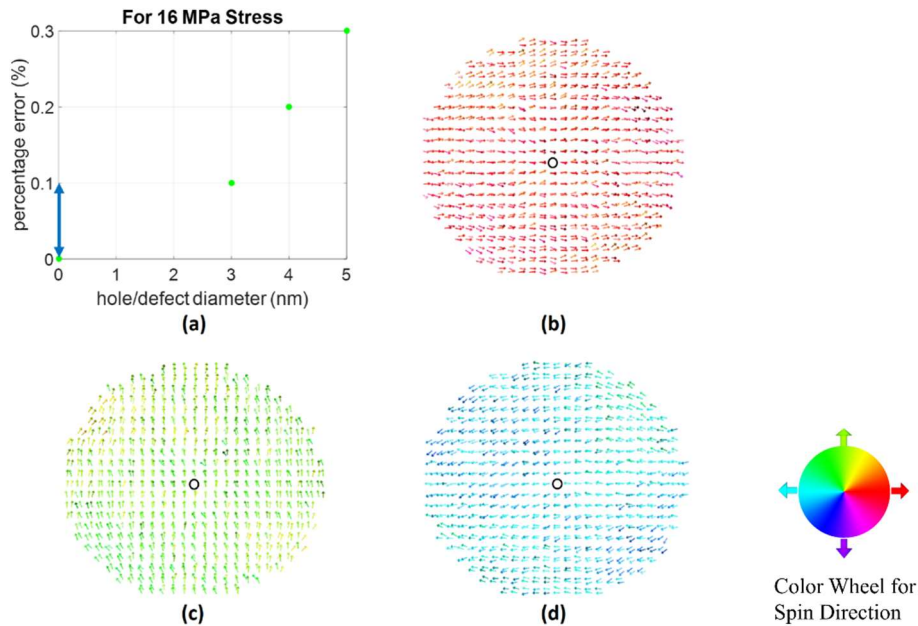


Fig. 3.7: (a) Switching error probability as a function of the hole diameter when the applied stress is 16 MPa; (b) Magnetization texture in the initial state (with a 3 nm diameter hole in the center); (c) Magnetization texture under a stress of 16 MPa; (d) Magnetization texture after release of stress
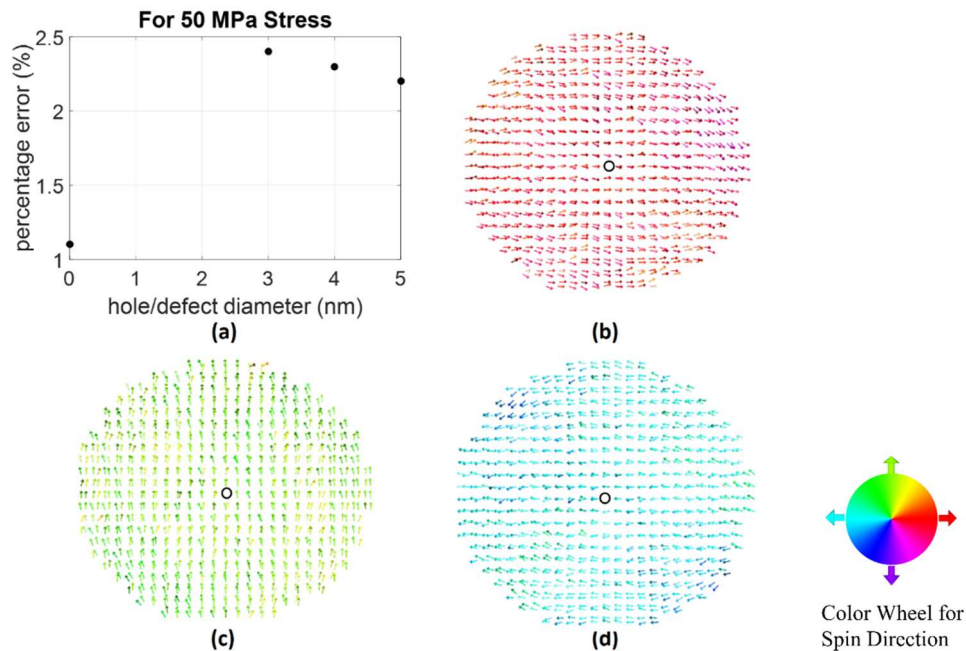
Fig. 3.8: (a) Switching error probability as a function of the hole diameter when the applied stress is 4 MPa; (b) Magnetization texture in the initial state (with a 3 nm diameter hole in the center); (c) Magnetization texture under a stress of 4 MPa; (d) Magnetization texture after release of stress

It is obvious from Figs. 3.5-3.8 that the switching error probability is sensitive to material defects since the probability always increases when there is a hole, provided the applied stress is either critical or super-critical (enough to erode or invert the barrier). Thus, magneto-elastic switching is not robust against material defects. These conclusions reinforce another recent work that uses different defect configuration to explain the critical role of defects in impeding magnetization control through the inverse magneto elastic (Villari) effect [44]. All this tells us that excellent material quality is required for reliable magneto-elastic switches.

An interesting observation is that for a given stress magnitude, the error probability does not increase monotonically with the diameter of the hole. This is not surprising. Different hole sizes produce different microscopic magnetization distribution within the nanomagnet at a given stress. It is entirely possible that the distribution corresponding to a smaller hole is more vulnerable to switching error than that corresponding to a larger hole. Thus, ensuring that defect size remains

small does not guarantee that the error probability will remain small as well when stress of a fixed magnitude is applied. There is no specific trend in the dependence of the error probability on hole diameter because the microscopic distributions of the magnetizations within the nanomagnet do not have a specific or predictable dependence on hole diameter at any given stress value.

In Fig. 3.9, we plot the error percentage as a function of stress for a 3-nm diameter hole located at the center of the nanomagnet. There is clearly a region of minimum error probability which establishes that there is a critical stress value for maximum error resilience. The same trend holds for other hole sizes (4 nm, 5 nm diameter) as well.
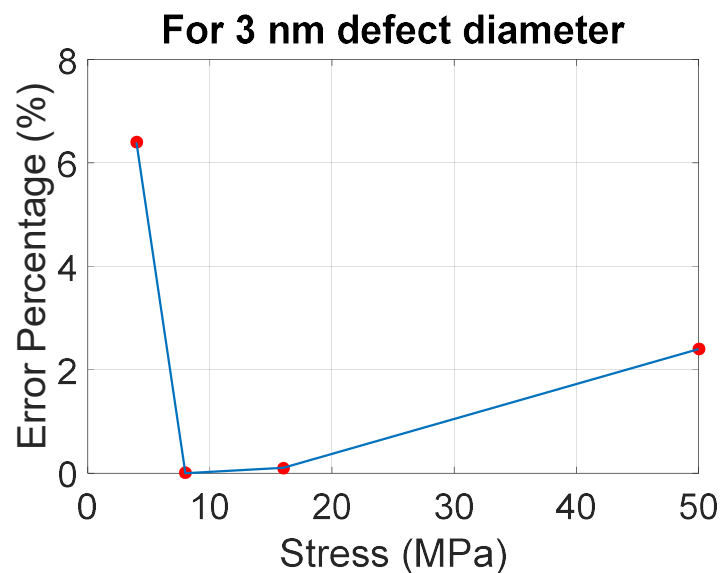


Fig. 3.9: Error probability versus stress for a 3 nm diameter hole. There is a region of stress that results in the lowest error probability and this region corresponds to the critical stress.

The study is also carried out for different locations of the defect in order to see any significant effect on the error probability. In Figs. 3.5-3.8, the hole is placed in the center of the nanomagnet. The effect of off-center holes is also investigated when the hole diameter is 3 nm and the applied stress is 4 MPa. In this case, the switching error probability is 6.4% when the hole is in the nanomagnet's center, and it changes to 7.2% when the hole is shifted along the major axis by 20

nm to the right. It changes to 7.4% when the hole is shifted by 20 nm along the minor axis to the top, and to 6.2% when the hole is shifted to a location (-10 nm, -10 nm), assuming that the center is at the origin. The magnetization distributions for these cases are shown in Fig. 3.10.

The reason hole location affects the error probability is because the latter is determined by the micromagnetic distributions within the nanomagnet at any given stress. Insofar as these distributions are altered by changing the location of the hole, it stands to reason that the hole position will affect the error probability.
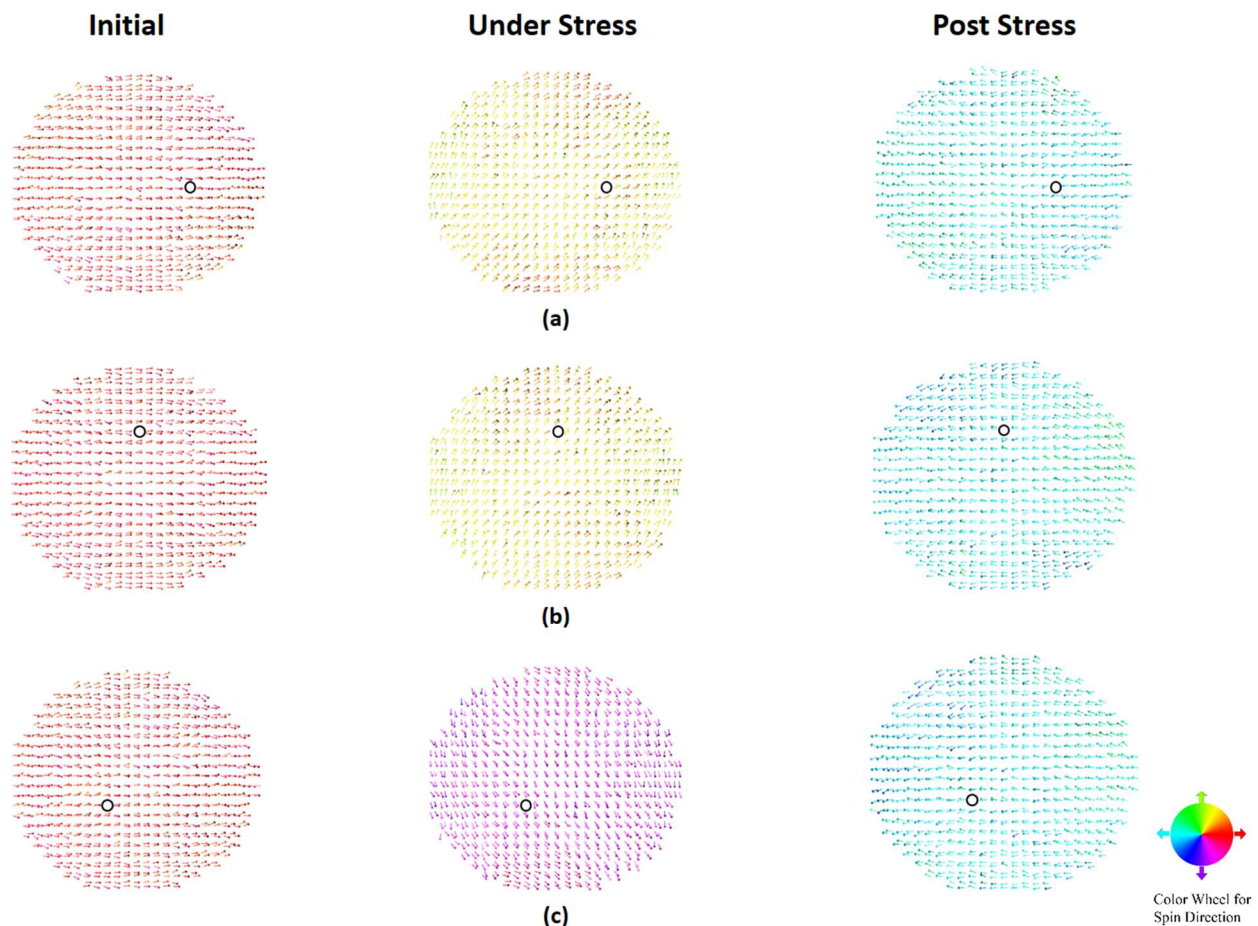


Fig. 3.10: Micromagnetic distributions when the hole is located: (a) 20 nm to the right of the center on the major axis, (b) 20 nm above the center on the minor axis, and (c) at the coordinate (-10 nm, -10 nm) assuming the center is the origin. The hole diameter is 3 nm and the applied stress is 4 MPa.

Next this study is extended for other types of common defects, including extended defects that are inherently different in influence than the localized point defect as shown in Fig. 3.2. All these are studied for static stress for two types of materials: Terfenol-D and Cobalt [8]. Next the effect of time-varying stress as opposed to static stress in various defective nanomagnets, for Cobalt only, are also studied for all the cases. In Figure 3.11, the switching error probability (i.e. failure of a nanomagnet to switch its magnetization from right to left under the action of the left pointing bias magnetic field) as a function of abrupt uniaxial stress applied along the major axis of the nanomagnet for a fixed duration of 1.5 ns is plotted. The material is *Terfenol-D* and the plots are for the defect-free and defective (C1-C6) cases. The maximum applied stress amplitude is 50 MPa. The Young's modulus of Terfenol-D is about 80 GPa and hence a 50 MPa stress would produce a strain of 625 ppm which is about the maximum a Terfenol-D nanomagnet can tolerate before stress relaxation via the formation of cracks and dislocations.

In Fig. 3.12, the switching error probability as a function of applied stress amplitude for *cobalt* nanomagnets, where once again the stress was applied for a fixed duration of 1.5 ns is plotted. The maximum stress amplitude that we consider for cobalt nanomagnets is 250 MPa. The Young's modulus of cobalt is 209 GPa and hence a stress of 250 MPa will produce a strain of 1200 ppm, which is about the maximum a cobalt nanomagnet can sustain before strain is relaxed through the formation of dislocations. We do not plot the results for defects C2 and C3 in the case of both Terfenol-D and cobalt because the shape anisotropy energy barrier in both nanomagnets with these defects becomes so low that just the bias magnetic field can always switch the magnetization at room temperature *without* the need for any stress to depress the shape anisotropy energy barrier. This is an interesting observation; the defect-free nanomagnet will not switch without stress, but the defective nanomagnets with C2 and C3 types of defects do because the energy barriers in these

nanomagnets are lower than that in a defect-free nanomagnet and low enough for the 3 mT magnetic field to overcome. This is one example where the defects may have a beneficial effect depending on the application.
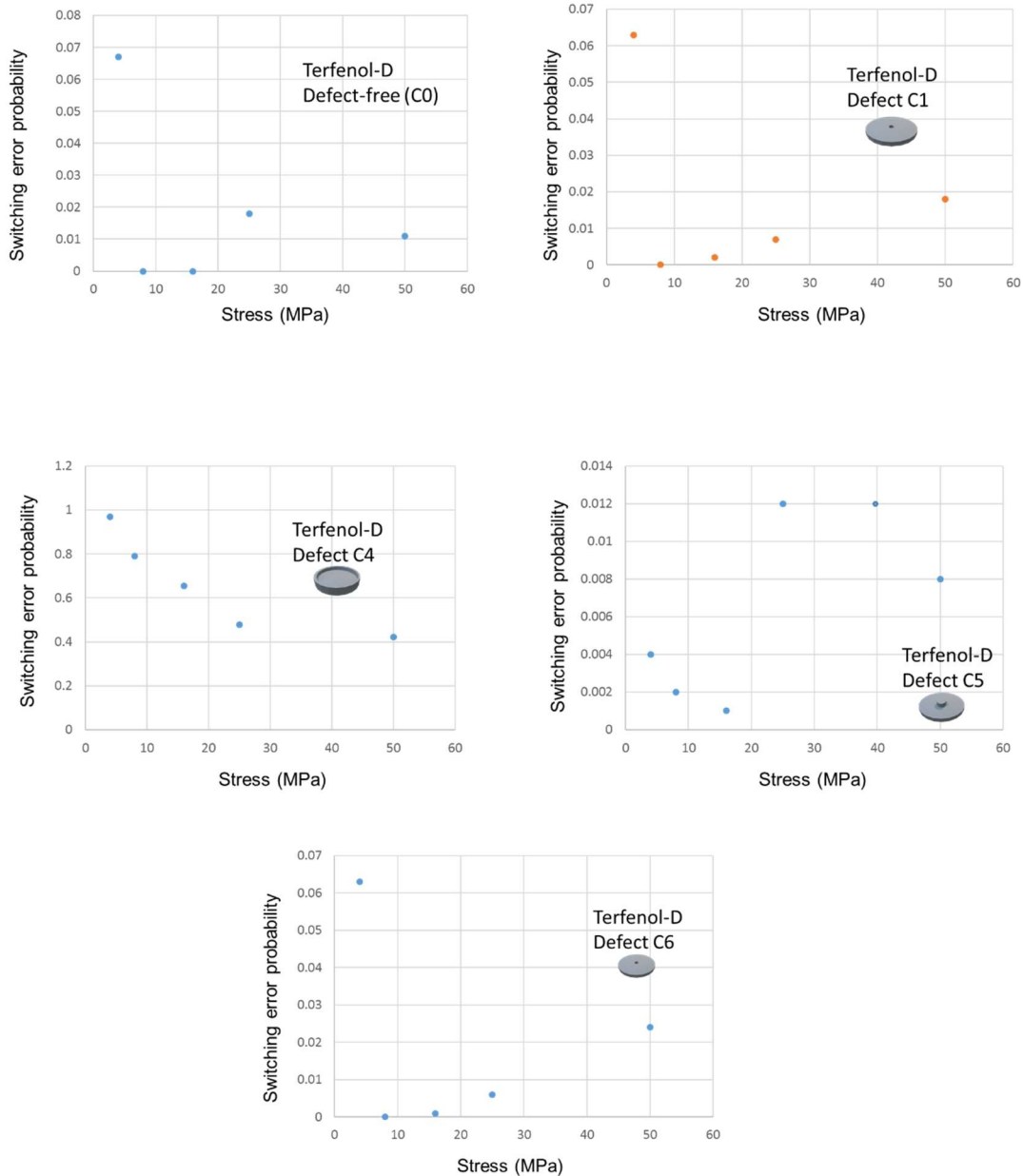


Fig. 3.11: Switching error probability at room temperature as a function of applied uniaxial stress for a Terfenol-D elliptical nanomagnet of nominal major axis 100 nm, minor axis 90 nm and thickness 6 nm. The plots are for the defect-free and defective nanomagnets with six different defects (C1-C6).

In every plot of both Figures 3.11 and 3.12, there is a range of stress where the switching error probability is *minimum*. This range is obviously where the "critical stress" is. Both under-stressing and over-stressing result in higher error probability than what is observed in the critical stress regime. Thus, this observation is consistent with the previous discussion. Note also that "localized" defects (e.g. a hole or a bump in the center – C1, C5 or C6) are less harmful than "delocalized/extended" defects (different thicknesses in different halves, or a rim – C2, C3, C4), because the error probabilities in the latter cases are much higher. The rim defect (C4) seems to be the worst offender producing the highest error probability.
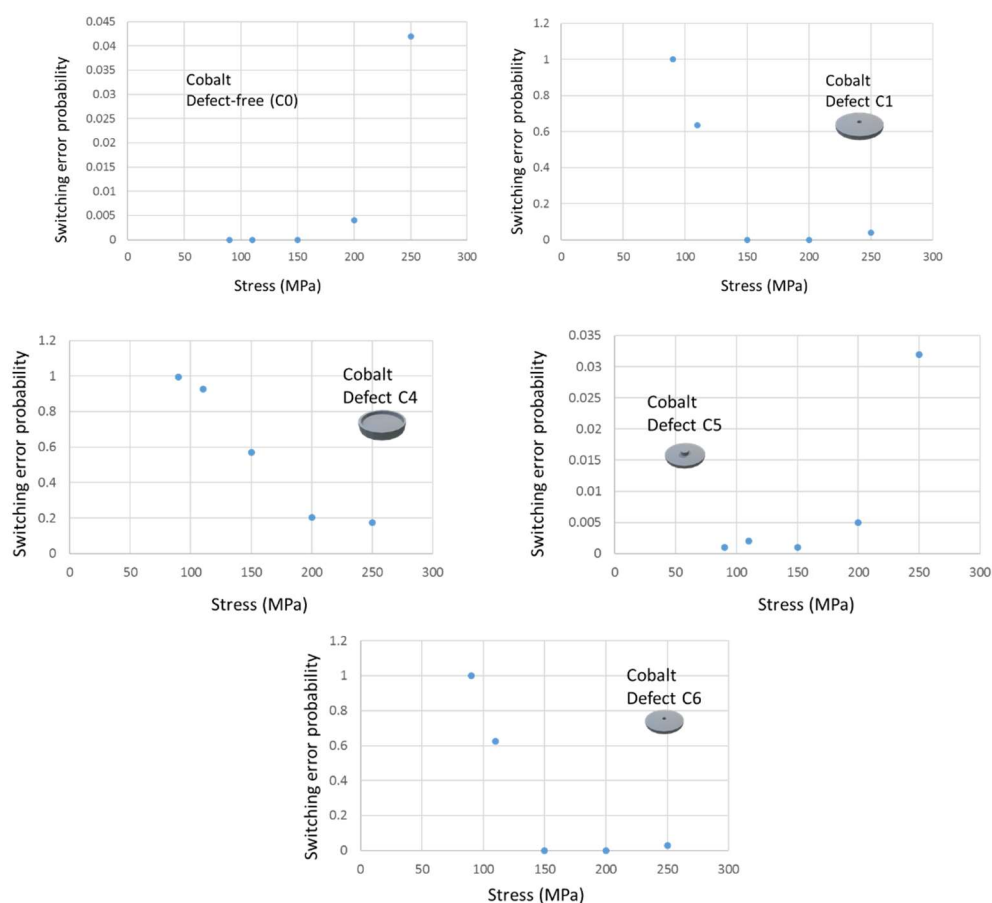


Fig. 3.12: Switching error probability at room temperature as a function of applied uniaxial stress for a cobalt elliptical nanomagnet of nominal major axis 100 nm, minor axis 90 nm and thickness 6 nm. The plots are for the defect-free and defective nanomagnets with defects C1, C4, C5 and C6. For C0 and C5, the error probabilities at 50 MPa stress are 0.997 and 0.998 respectively.

In Figure 3.13, the switching error probability as a function of the acoustic wave stress amplitude for each defect in cobalt, except C2 and C3, and for two different stress wave frequencies – 200 MHz and 1 GHz are plotted. Cases C2 and C3 are again ignored since these nanomagnets have very low energy barriers and their magnetizations can be flipped by the magnetic field alone, without the need for any stress. Also only two frequencies (and not more) are examined because of the excessive computational burden. For example, to simulate for one period at 200 MHz, we have to simulate for 5 ns with a time step of 0.1 ps. This requires 50,000 time steps. This needs to repeat for 1000 switching trajectories, which requires $50,000 \times 1,000 = 5 \times 10^7$ steps. Then, the entire exercise needs to repeated for 5 different nanomagnets with four different stress amplitudes, requiring $20 \times 5 \times 10^7 = 10^9$ steps for each frequency. This takes several weeks of run time on a special purpose computer for running MuMax3. Therefore, examining too many frequencies will be computationally prohibitive.

It is intriguing to find from Fig. 3.13 that for the lower frequency, time varying stress (of sufficient amplitude) is actually *more effective* in switching nanomagnets (both defect-free and defective) than static stress since the error probabilities are lower for all cases, except defect C4. For the 200 MHz sinusoidal stress, the error probability is < 0.001 (we simulated only 1000 trajectories and none of them failed) for all defects except C4, as long as the stress amplitude exceeds a threshold value. This is a promising result since it shows that switching with sinusoidal stress results in low error probabilities even in the presence of most types of defects. What this reveals is that gradual stressing and de-stressing is more effective than abrupt stressing and de-stressing, provided the frequency is slow enough (200 MHz) to allow the magnetization enough time to respond to the stress. If the frequency is too high (1 GHz), the magnetization does not have ample time to respond to the stress and this increases the failure probability. The defect C4 is an exception where, for any

given stress amplitude, the slow frequency results in *higher* error probability than the fast frequency. This tells us that the interplay between the temporal dynamics of magnetization and the temporal dynamics of stress is complex and that could result in counter-intuitive results in some cases.
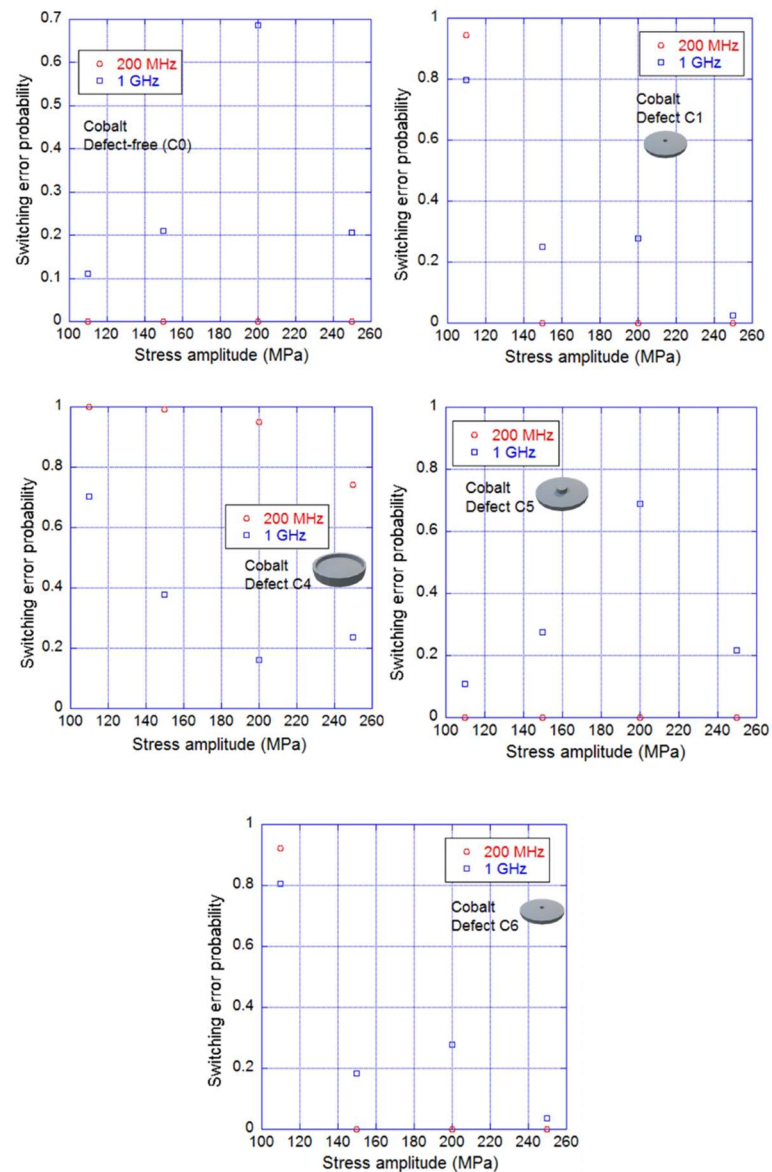


Fig. 3.13: Switching error probability at room temperature as a function of applied uniaxial stress amplitude of a surface acoustic wave of frequency 200 MHz and 1 GHz for a cobalt elliptical nanomagnet of nominal major axis 100 nm, minor axis 90 nm and thickness 6 nm. The plots are for the defect-free and defective nanomagnets with defects C1, C4, C5 and C6.

It is interesting to observe that in the case of high frequency (1 GHz), the switching error shows a non-monotonic dependence on stress amplitude and is higher at 200 MPa than at all other stress amplitudes. The exception to this is C4 for which the switching error is smaller at 200 MPa than at all other stress amplitudes considered. This, and other anomalous behaviors, sets C4 apart from other defects. The potential energy profile in the C4 nanomagnet may have complex features that is responsible for its odd behavior. The defect C4 is actually a frequent occurrence and it always results in a relatively high error probability.

### 3.5 Conclusion

In this chapter, it is shown that magneto-elastic switching is vulnerable to material voids; defects exacerbate switching failures in the presence of thermal noise. It is also shown that there exists a critical stress that results in the most reliable magneto-elastic switching in both defective and defect-free nanomagnets. There are however two primary concerns. The first is that defects and fabrication imperfections can make the switching much less reliable than what one might infer for defect-free nanomagnets because the critical stress value increases in the presence of defects. The second is that as one downscales nanomagnets to lateral dimensions of ~ 20 nm or less and thickness ~ 2 nm (which would be desirable for high-density non-volatile memory applications) while maintaining a fixed energy barrier $E_b$ for thermal stability, the critical stress (inversely proportional to nanomagnet volume) will become correspondingly higher and may be difficult, or impossible, to generate within the nanomagnet. Since the critical stress is higher in nanomagnets with a defect, the problem is more severe in the presence of defects. Thus, reliable magneto-elastic switching of nanomagnets with in-plane magnetic anisotropy may not have much tolerance for defects and may also suffer from serious scaling limitations. It is commonly believed in the magneto-elastic community that employing materials with higher magnetostriction (e.g. Terfenol-

D instead of cobalt) will lead to a larger effective switching field due to stress anisotropy and that may improve the switching probability. That may not be necessarily true when one considers bi-directional coupling between the piezoelectric and magnetostrictive components, but even if that were true, defects can *erase* any advantage of the higher magnetostriction material. For example, when defect of the type C4 is present, the switching error probability in the Terfenol-D nanomagnet is actually worse than that in the cobalt nanomagnet. Thus, it is more imperative to eliminate defects than to develop better magnetostricitve material because defects have a much larger influence on switching error rates than the material (magnetostriction). Researchers in the field of magneto-elastic switching should therefore prioritize eliminating defects over developing better materials with higher magnetostriction.It is also observed that *localized* defects (such as a small hole or hillock) are more forgiving than *delocalized* (extended) defects such as thickness variation across a significant fraction of the nanomagnet surface, or rim around the periphery. Delocalized defects have a much more deleterious effect on switching error than localized ones. However, even localized defects give rise to switching error probabilities that are too high for error-intolerant computing applications such as Boolean logic and memory. This seems to suggest that magneto-elastic switches may be better adapted to certain types of non-Boolean computing paradigms, particularly collective computational models where the collective activity of many nanomagnets working collaboratively elicit the computational activity (e.g. image processing). There, the failure of a single (or few) switch is not catastrophic.

Finally, it is found that sinusoidal time varying stress of the right frequency can reduce the switching error probability compared to constant stress for most cases. This is consistent with the observation in ref. [39] which found a very high success rate with time-varying stress. Thus, if

magneto-elastic switches are to be used in memory, writing with a time-varying stress [36-47], as opposed to a stress pulse of fixed amplitude, may be beneficial.

# Chapter 4: The effect of material defects on resonant spin wave modes in a nanomagnet

Spin wave modes in a nanomagnet govern its dynamical behavior. Magnetization reversal in a nanomagnet – a phenomenon that undergirds the operation of virtually all magnetic switching devices used in memory, logic, and non-Boolean computing – is mediated by two major types of collective excitations: spin waves and domain wall motion [45]. It is therefore imperative to understand the nature of spin wave excitations in a nanomagnet since it can determine the speed of magnetic reversal, as well as some other properties such as switching error rate. Today, spin waves have an even more important role to play since they are the central ingredients in spin wave logic [46][47], magnetic nano-oscillators for nanoscale microwave generators [48] and certain types of artificial neural networks [49].

Spin wave modes in nanomagnets have been a subject of research for about two decades [50]. Initially, interest was focused on understanding their behavior and damping inside individual nanomagnets and their dependence on size, shape and initial magnetic configuration [51-55]. Later, interest shifted towards understanding the collective dynamics in an array of nanodots [56][57], which emerged as a potential candidate for a two-dimensional magnonic crystal. Much work has been reported on the dependence of spin wave dynamics on the size and the shape of nanomagnets, the lattice constant, the lattice symmetry of the array, bias field strength and orientation, as well as binary and bi-component nature [58-64]. Important physics such as spin wave mode splitting, mode cross-over, dynamic dephasing, transition between various collective regimes, intrinsic and extrinsic dynamical configurational anisotropy, etc. have been reported. Energy efficient spin-wave device concepts have also been proposed based on shaped nanodot arrays [65]. Many of these studies have considered edge roughness and deformation of the nanomagnets and their effect on spin waves, but the influence of various types of defects in nanomagnets on spin wave modes and dynamics has remained unexplored.

In this chapter, the resonant spin wave modes in an elliptical nanomagnet in presence of different types of imperfections or "defects" are studied theoretically. Specifically, it is studied how the power and phase profiles of these modes are altered by small local variations in the nanomagnet thickness. This study reveals that defects (various types of thickness variations) can have significant effects on the spin wave modes. They can change the frequencies of the resonant modes which has serious consequences for microwave generators or phase locked oscillators used for neuromorphic computation [66]. They can also generate completely new modes or quench existing ones, and that can have consequences in many other applications as well.

## 4.1 Material Used and Defect Modeling

Defects (thickness variations) are usually unavoidable during the fabrication process. Fig. 4.1 (also shown in figure 3.1 in chapter 3) shows atomic force micrographs of nanomagnets fabricated in our lab with standard electron beam evaporation of Co into lithographically delineated windows opened in e-beam resist. The resists are patterned with electron beam lithography and the nanomagnets are produced by lift-off. The lateral dimensions of these nanomagnets are on the order of 100-300 nm and their thickness is on the order of 16 nm. Note that in Fig. 4.1, the nanomagnets have "rims", i.e. the thickness is much larger along the periphery than at the center. This type of defect is an aftermath of the lift-off process and is fairly common. Other types of defects will involve "voids" (missing material) or "mesas" (excess material) at certain locations on the nanomagnet's plane. The types of defects that we have studied are shown in Fig. 4.2. Note that defect type C4 approximates the structure shown in Fig. 4.1.
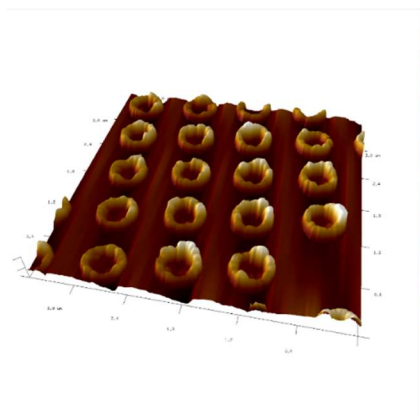
Fig. 4.1: Atomic force micrograph of an array of Co nanomagnets deposited on a substrate using electron beam lithography, electron beam evaporation of Co on to the patterned substrate, followed by lift-off. The nanomagnets have significant thickness variation, with the thickness being much larger in the periphery than in the center.
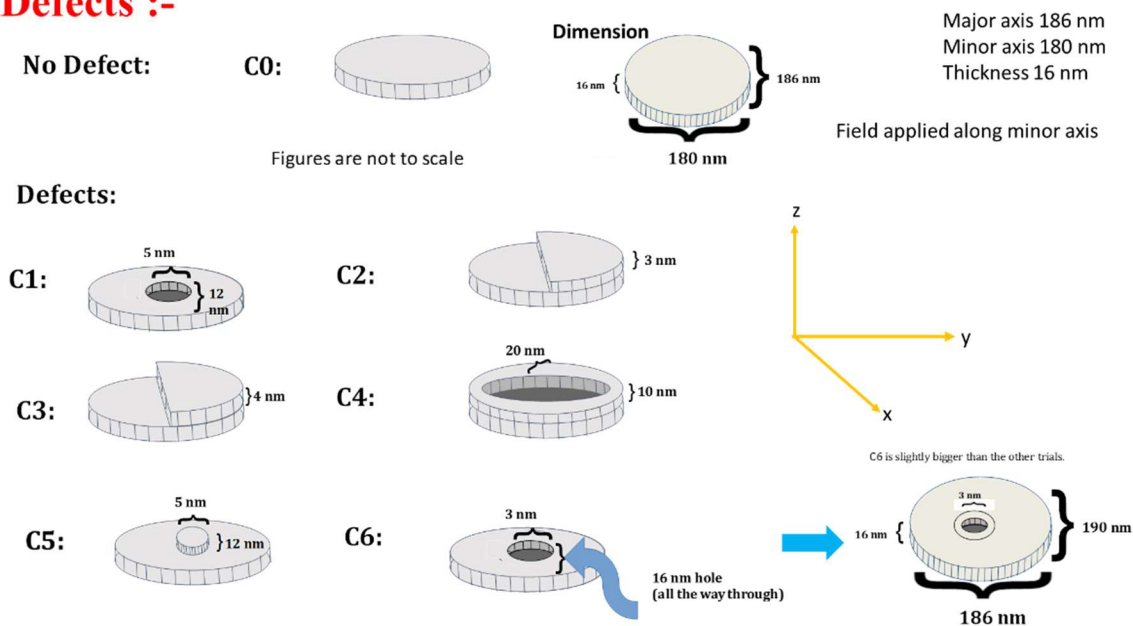


Fig. 4.2: Classification of defects in an elliptical cobalt nanomagnet of major axis dimension 186 nm, minor axis dimension 180 nm and thickness 16 nm: C0 (defect-free), C1 (hole in the center with diameter 5 nm and depth 12 nm), C2 (thickness variation where one half of the nanomagnet is 3 nm thicker, C3 (thickness variation where one half is 4 nm thicker), C4 (the periphery forms an annulus of width 20 nm and height 10 nm, C5 (thickness variation where a central circular region of diameter 5 nm is 12 nm thicker), and C6 (a through hole of 3 nm diameter at the nanomagnet's center; this nanomagnet dimension is slightly larger with major axis of 190 nm and minor axis of 186 nm). This figure is not drawn to scale.

## 4.2 Spin Wave Excitation

Spin waves can be excited in a nanomagnet in a variety of ways. One common approach is to apply a bias magnetic field in the plane of the nanomagnet and then induce precession of the magnetization around this field with an ultrashort laser pulse. This is easily achieved in a time-resolved magneto-optical Kerr effect (TR-MOKE) and ferromagnetic resonance set-up. The precession spawns confined spin waves in the nanomagnet. In order to study them, the simulation is done in the following method: cobalt nanomagnets are considered in the form of elliptical disks whose major axis dimension is 186 nm, minor axis is 180 nm and thickness is 16 nm. A bias magnetic field is applied along the minor axis. Then an out-of-plane magnetic field pulse of amplitude 30 Oe, rise time 10 ps, and duration 100 ps is applied perpendicular to the nanomagnet's plane to simulate the effect of the laser pulse. This out-of-plane field sets the precession of the magnetization about the bias field in motion.

## 4.3 Simulation, Results and Discussion

The time evolution of the nanomagnet's magnetization is tracked by using the micromagnetic simulator MuMax3 [30] which allows us to determine the out-of-plane micromagnetic component $M_z(x, y, z, t)$ at every coordinate point within the nanomagnet at every instant of time. The nanomagnet is discretized into cells of dimension $2 \times 2 \times 2$ nm$^3$. The cell size in all directions is kept well below the exchange length of cobalt to consider both dipolar and exchange interactions in the magnetization dynamics of nanoscale magnets as well as to accurately reproduce the shapes of the nanomagnets under study. The time step used is 1 ps. The magnetic parameters used for the simulation are: saturation magnetization $M_s$= 1100 emu/cm$^3$, gyromagnetic ratio $\gamma$ = 17.6 MHz/Oe and exchange stiffness constant $A_{ex}$= 3.0 × 10$^{-6}$ erg/cm. These parameters correspond to cobalt

nanomagnets. Spatially averaged over space is performed to find the out-of-plane magnetization component $\bar{M}_z(t)$ as a function of time.

The simulation is started by preparing the magnetic ground state upon applying the bias magnetic field ($H$) along the minor axis of the elliptical nanomagnet at time $t = 0$. The initial magnetization is assumed to have been directed along the major axis which is the easy axis. Next, the out-of-plane magnetic field pulse is applied and the time evolution of the out-of-plane magnetization $\bar{M}_z(t)$ is studied (associated with precession of the magnetization around the bias magnetic field) for 4 ns (4000 time steps).
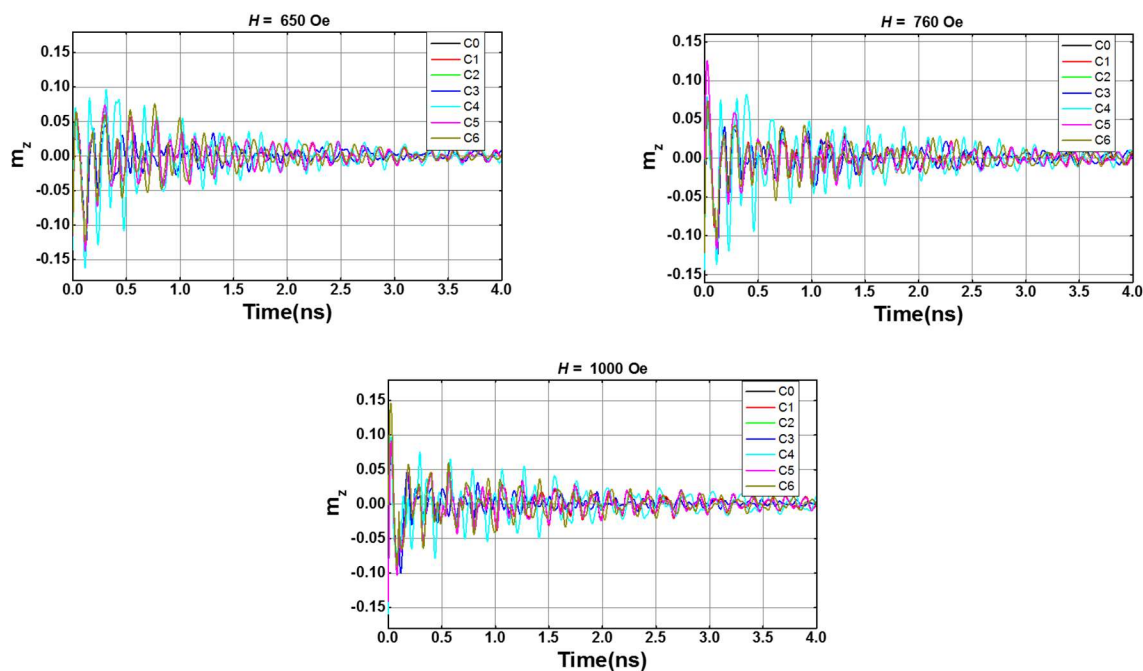


Fig. 4.3: The spatially averaged out-of-plane magnetization component as a function of time for the seven different (defect-free and defective) cobalt nanomagnets. The plots are for three different bias fields of strength 650 Oe, 760 Oe and 1000 Oe.

Fig. 4.3 shows $\bar{M}_z(t)$ versus $t$ for the seven different (defect-free and defective) nanomagnets at three different bias magnetic fields of strengths, $H = 650$ Oe, 760 Oe and 1000 Oe. Fast Fourier

transform (FFT) is performed for each of these "oscillations" to extract the dominant frequencies (frequency peaks) in the oscillation. These are the frequencies of the resonant spin wave modes in the nanomagnet. The frequency resolution in the FFT depends upon the total simulation time. Since the simulation time is 4 ns, the frequency resolution is 0.25 GHz.

Fig. 4.4 plots the Fourier spectra for the seven nanomagnets at three different bias fields. The peaks in these spectra correspond to the frequencies of the resonant spin wave modes in the seven nanomagnets.
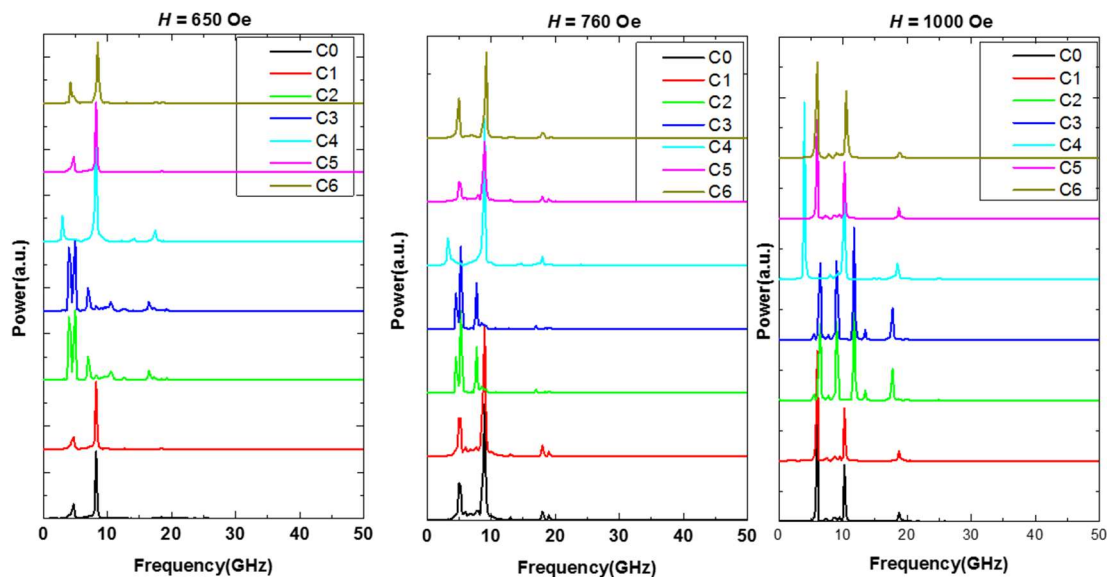


Fig. 4.4: Fast Fourier transforms of the $\bar{M}_z(t)$ versus $t$ oscillations for the seven different nanomagnets at three different bias field strengths ($H$). These are the frequencies of the dominant spin wave modes in the nanomagnets at the corresponding bias field.

There are three interesting features to note in Fig. 4.4. First, the spectral peaks, which are the frequencies of the resonant spin wave modes, are different in the seven different nanomagnets at the same bias magnetic field. This shows that *defects affect the frequencies of the resonant spin*

*wave modes* and that has important implications for spin wave microwave generators. Second, the bias field dependence of the resonant mode frequencies (peaks in the spectrum) are sensitive to defects. Thus, the "tunability" of the oscillation frequency with a magnetic field is affected by the presence of defects. Third, defects spawn some resonant modes that are absent in the defect-free nanomagnet. Conversely, defects can also quench resonant modes that are present in the defect-free nanomagnets.

In order to calculate the power and phase profiles of the spin wave modes, the following procedure is followed: the $z$-coordinate at a particular value $(z = z_m)$ is kept fixed and a discrete Fourier transform (FFT) of $M(x, y, z, t)|_{z=z_m}$ (obtained from MuMax3 simulation) is performed with respect to time to yield $\tilde{M}^{z_m}(f, x, y) = FFT[M^{z_m}(t, x, y, z)|_{z=z_m}]$. The fixed value of the $z$-coordinate $(z_m)$ is chosen to be at the surface of the nanomagnet. Using software *Dotmag* the plot $(x, y)$ spatial distribution of the power and phase of the spin waves at chosen frequencies $f_n$ on the surface of the nanomagnet$(z = z_m)$ are obtained according to the following relations [67][68].

$$P^{z_m, f_n}(x, y) = 20 \log_{10} \tilde{M}^{z_m}(f_n, x, y);$$
$$\phi^{z_m, f_n}(x, y) = \tan^{-1}\left(\frac{\mathrm{Im}\left(\tilde{M}^{z_m}(f_n, x, y)\right)}{\mathrm{Re}\left(\tilde{M}^{z_m}(f_n, x, y)\right)}\right), \qquad (1)$$

where $f_n$ is the frequency of a resonant mode. The power is expressed in dB and the minimum value of $\tilde{M}^{z_m}(f_n, x, y)$ is normalized to unity.

Figures 4.5-4.11 show the power and phase profiles of the resonant spin wave modes in the seven different nanomagnets. It is observed that four different types of modes: center mode (where power is localized at the center of the nanomagnet), edge mode (where power is localized at the edges),

quantized mode (where power is localized at discrete locations) and mixed quantized mode. For some mixed quantized mode, it is difficult to define exact quantized number due to its blurred and equivocal nature.

In a continuous thin film, there are three types of magnetostatic spin-waves. They are categorized based upon the relative orientation of the magnetization ($M$) and the wave vector ($k$) of the spin wave. I) <u>Damon-Eshbach (DE) mode</u> – In this mode magnetization and the wave vector both lie in the film plane and form an angle $\phi \approx 90°$. This is also known as magnetostatic surface wave (MSSW) mode [69]. II) <u>Backward Volume (BV) mode</u> - In this mode, the magnetization and the wave vector both are collinear and lie in the film plane [70]. III) <u>Forward Volume (FV) mode</u> - In the so-called magnetostatic forward volume mode (MSFVM) geometry the magnetization is perpendicular to the film [71]. In this system of nanomagnets, modes that are similar to the first two types of modes can exist since we apply the bias magnetic field in the plane of the sample. Nothing like the third type of mode can exist. Since the modes in the nanomagnets are not propagating modes, they are not exactly classifiable as DE or BV modes. The generated spin waves get reflected from the boundaries of the nanomagnets and form standing spin-wave modes similar to resonant cavity modes. Hence, they are called resonant modes. Because of their confined nature, instead of assigning wave vector to the modes, the number of nodal planes are counted and a mode quantization number is assigned to the observed modes. The quantization numbers are defined according to whether the quantization axis is along the magnetic field direction ($n$, in BV geometry) or perpendicular to the field direction ($m'$, in DE geometry). In some cases, the modes are quantized along the azimuthal axis. We name those as azimuthal modes with a corresponding quantization number ($m$).

From Figures 4.5-4.11, we see that certain types of defects (C1 and C5) are relatively innocuous and affect the resonant spin wave modes slightly. They do not spawn new modes or quench existing ones. The changes they introduce in the power and phase profiles are also moderate. Defect C6 is similar to C1, but unlike C1, this is a through hole which makes it more invasive (the size is also slightly larger). The through-hole spawns a new mode at 650 Oe bias magnetic field and quenches an existing mode at 760 Oe field. It does not alter the power profiles significantly, but affects the phase profiles much more. Defects C2 and C3 are associated with thickness variation across one-half of the nanomagnet's surface. These types of defect are found to be extremely invasive and spawn new resonant modes at all magnetic fields. They also alter the power and phase profiles of the resonant modes very perceptibly. Thickness variation across a significant fraction of a nanomagnet's surface is therefore more serious than having localized defects such as a "hole" (C1, C6) or a "hillock" (C5). Defect C4 is important since it is commonplace in nanomagnets fabricated by electron-beam evaporation of a ferromagnetic metal into a lithographically delineated window in an e-beam resist. Curiously, it is not as invasive as C2 and C3. Like C6, it changes the power profiles slightly, but affects the phase profiles much more. The frequency of the edge mode decreases significantly. It also quenches a quantized mode that appears in the defect-free nanomagnet at the intermediate field of 760 Oe.

Based on these observations, it appears that maintaining thickness uniformity across a significant fraction of the nanomagnet's surface would be critical in applications that require reproducibility of resonant spin wave power and phase profiles. Defects associated with thickness variations have a more serious effect on the resonant spin wave power and phase profiles than localized defects.
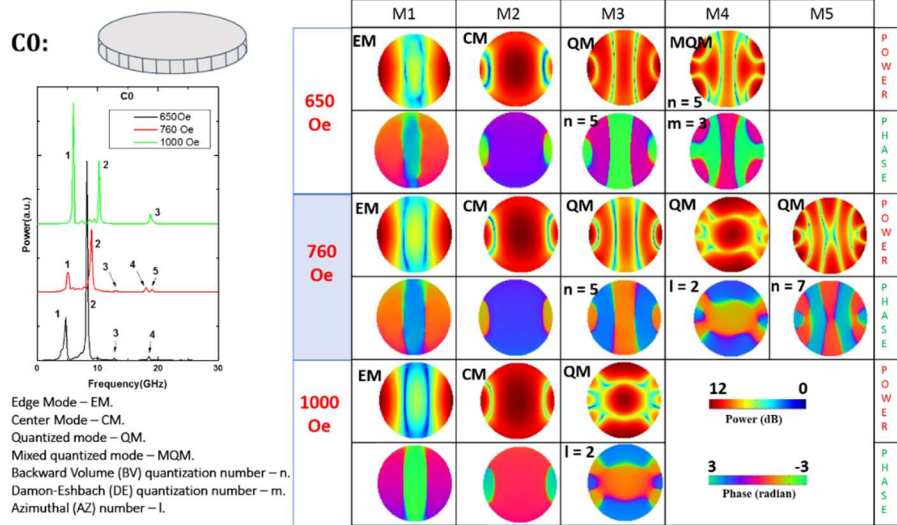
Fig. 4.5: Power (top row) and phase (bottom row) profiles of the resonant spin wave modes on the surface of the defect-free nanomagnet (C0) at three different bias magnetic fields. The left panel shows the Fourier transform spectra $\tilde{M}^{z_m}(f,x,y)$ at the three different fields in the defect-free nanomagnet and the right panel shows the power and phase distributions in space (profiles). The resonant modes are the ones that correspond to the peak frequencies in the Fourier transform spectra shown in the left panel and are labeled M1, M2, …These modes are either center mode, edge mode, quantized mode or mixed quantized mode. The phase varies from $-\pi\,(\approx -3)$to $\pi\,(\approx 3)$and the power varies from 0 to 12 dB.
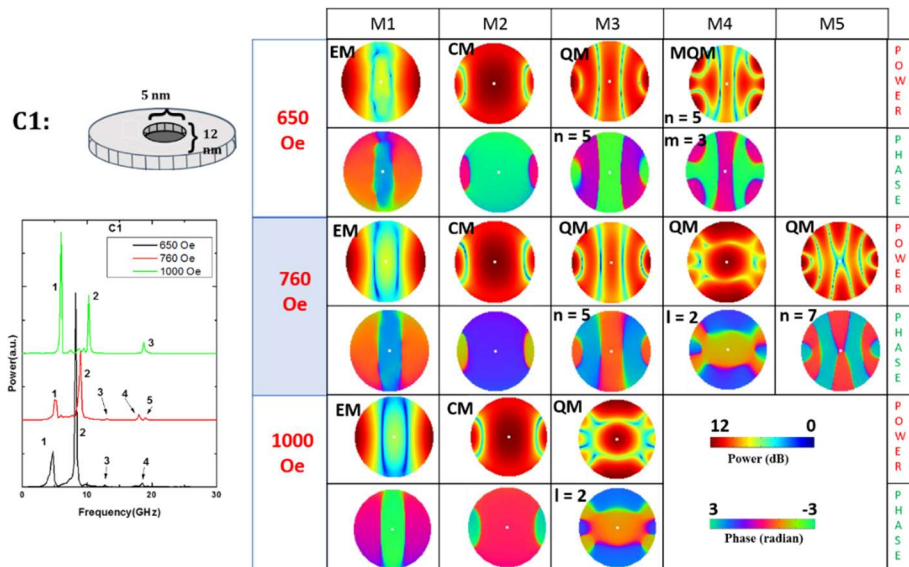


Fig. 4.6: Power (top row) and phase (bottom row) profiles of the resonant spin wave modes on the surface of the nanomagnet with defect of type C1 at three different bias magnetic fields. No new mode is spawned and none is quenched by the defect.
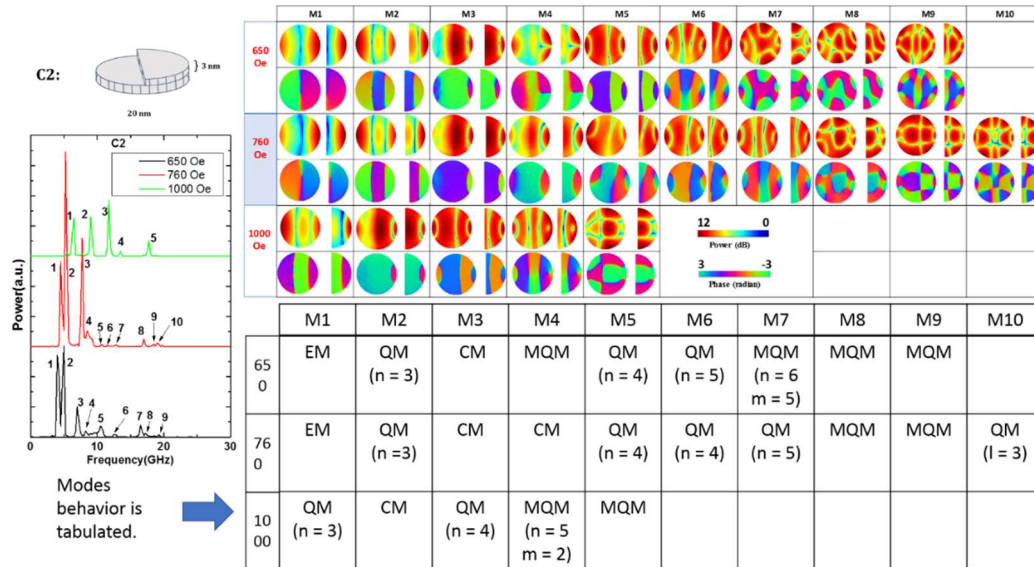
Fig. 4.7: Power and phase profiles of the resonant spin wave modes on the surface of the nanomagnet with defect C2 at three different bias fields. The top row shows the power profile and the bottom row the phase profile at any given bias field strength. The left panel shows the Fourier transform spectra $\tilde{M}^{z_m}(f, x, y)$ at three different bias magnetic fields. There are a large number of resonant modes in this case (magnet thickness varies), many of which are absent in the defect-free nanomagnet. Clearly, this type of defect spawns new modes.
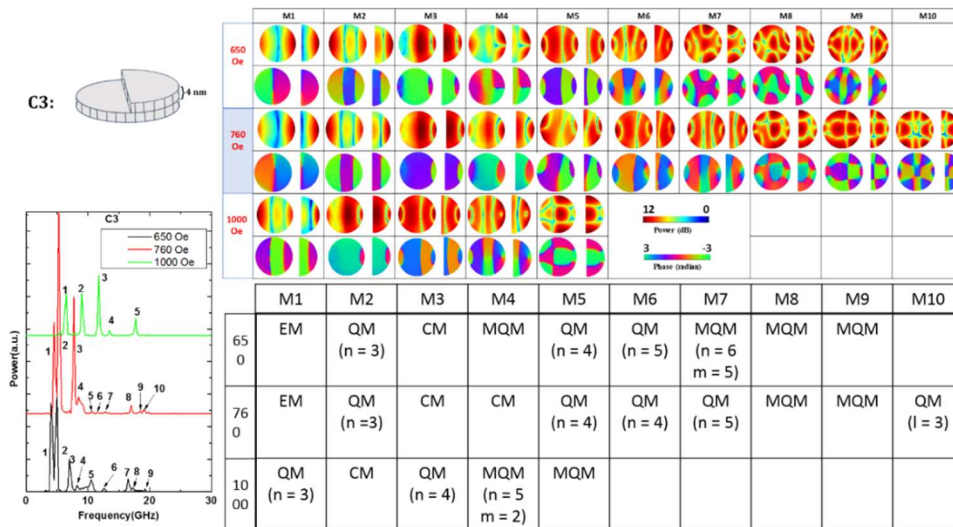


Fig. 4.8: Power (top row) and phase (bottom row) profiles of the resonant spin wave modes on the surface of the nanomagnet with defect C3 at three different bias fields. The left panel shows the Fourier transform spectra $\tilde{M}^{z_m}(f, x, y)$ at three different bias magnetic fields. New resonant modes are spawned by this defect.
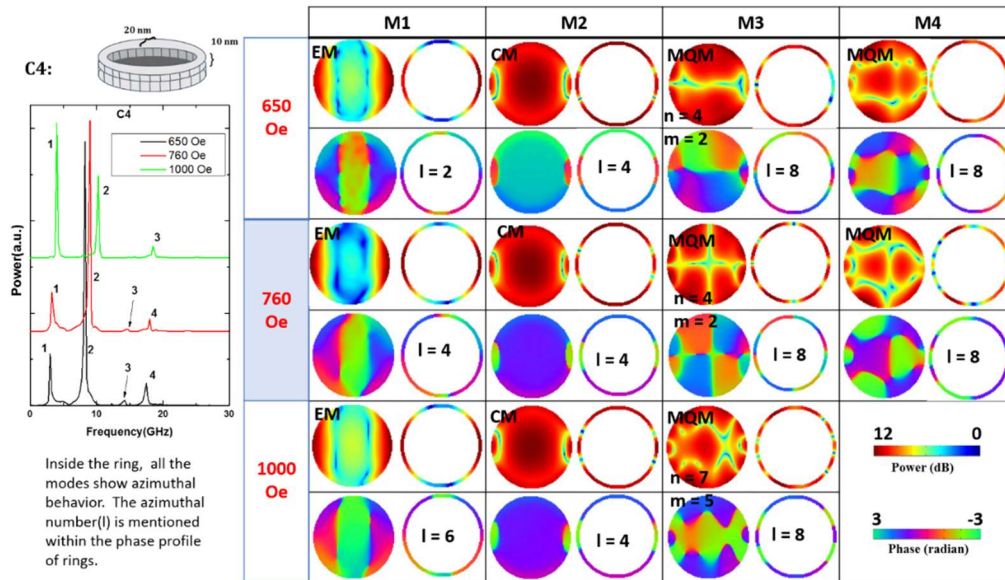
Fig. 4.9: Power (top row) and phase (bottom row) profiles of the resonant spin wave modes on the surface of the nanomagnet with defect C4 at three different bias magnetic fields. This is the case that most closely approximates the structure in Fig. 1. Here, we show, separately, the power and phase profiles in the surface of the nanomagnet (left) and in the surface of the 20 nm thick annulus (right). No new mode is spawned, but one is quenched.
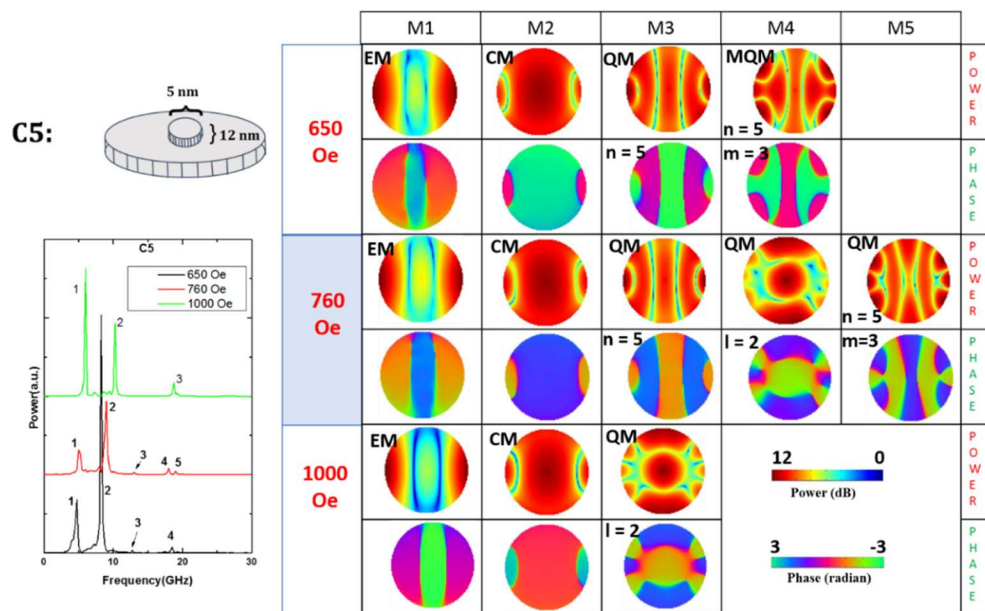


Fig. 4.10: Power (top row) and phase (bottom row) profiles of the resonant spin wave modes on the surface of the nanomagnet C5 at three different magnetic fields. No new modes are spawned and none quenched.
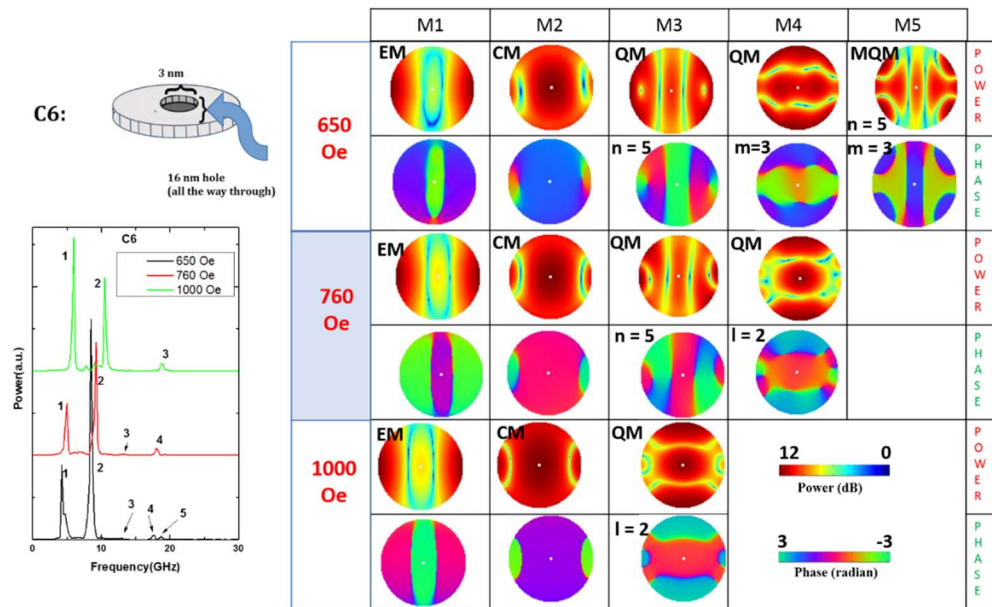
Fig. 4.11: Power (top row) and phase (bottom row) profiles of the resonant spin wave modes on the surface of the nanomagnet C6 at three different magnetic fields. A new mode is spawned at the low field and one is quenched at the intermediate field.

## 4.4 Conclusion

This study has shown that several features of resonant spin wave modes in a nanomagnet (frequencies, magnetic field dependence of the frequencies, number of resonant modes) are affected by the presence of defects associated with thickness variations in the plane of the nanomagnets. This has serious consequences for many applications that rely on spin wave modes. In the past, it was found that in magnetostricitve nanomagnets, strain-induced magnetization reversal (switching) probability is dramatically affected by the presence of defects [7]. Here, we have found that defects also have a dramatic effect on spin wave modes. Applications that have little tolerance for variations of spin wave frequencies, or their phase profiles – e.g. phase locked nano-oscillators for neuromorphic computing[5,22] – are especially vulnerable. These applications will require pristine (almost defect-free nanomagnets) that may challenge existing nanofabrication technology.

**Chapter 5: Low Barrier Nanomagnet Design for Binary Stochastic Neurons: Design Challenges for Real Nanomagnets with Fabrication Defects and Power Spectra of Magnetization Fluctuations in Low Barrier Nanomagnets**

Binary nanomagnets, with two stable magnetization directions, have long been thought of as potential replacements for transistor switches because they can be more energy-efficient in some circumstances and have the added boon of being non-volatile. They are switched between their two stable states with either current-controlled mechanisms (e.g. spin transfer torque [72], domain wall motion [73], giant spin Hall effect [74], spin diffusion from topological insulators [75], spin-orbit torque [76], etc.) or voltage-controlled mechanisms (e.g. voltage-controlled-magnetic-anisotropy (VCMA) [77], straintronics [78], etc.). The latter are more energy-efficient, but also more error-prone. Theoretical estimates of switching errors in magneto-elastic switching (straintronics) range from $10^{-3}$ [38] to as low as $10^{-8}$ [4], but experiments show a much larger error probability exceeding 0.1 [34][79]. Recently, it is shown that this large difference between theory and experiments accrues from the fact that real nanomagnets used in experiments invariably have structural defects and they exacerbate the switching error [8]. The error probability associated with VCMA switching is also relatively large and experiments show it to be $\sim 10^{-5}$ [80] or more.

Error probabilities this high will probably make these switches unusable for Boolean logic, and maybe even memory if we insist on low write energies (lower write energies lead to higher error rates). In logic, errors propagate and consequently the switching error probability of a switch should be less than $10^{-15}$ for logic applications [81]. Memory is more forgiving since errors do not propagate, but in order to avoid repetitive write/read/re-write operations, the error probability still needs to be below $10^{-9}$ [82]. Such low error probabilities may be out of reach for voltage-controlled binary nanomagnetic switches, and maybe a tall order for even current-controlled (more dissipative) ones if we wish to expend no more than $\sim 1$ fJ of write energy per bit. Using higher write energies might improve the write error probability, but high energies are undesirable in embedded applications. Because of this impasse, there has recently been increasing interest in

applying magnetic switches for *non-Boolean* applications such as in Bayesian inference engines [83][84], restricted Boltzmann machines [85], image processing [6][31], computer vision [86], neural networks [87][88], analog-to-digital converters [89], and probabilistic computing [90][91]. These applications can tolerate much larger error probabilities than Boolean logic or memory can.

## 5.1 Stochastic Binary Neurons Based on Low Barrier Magnets (LBM)

Probabilistic computing has attracted particular attention since it can leverage the thermally induced fluctuations in the magnetization of a nanomagnet (which would have caused unwanted errors in logic or memory devices) to actually elicit useful computational activity. Stochastic binary neurons are a class of probabilistic computing devices. They are implemented with low energy barrier nanomagnets (LBMs) where the energy barrier separating the two stable magnetization states is purposely made small enough that thermal noise can make the magnetization fluctuate randomly with time. This random magnetization distribution is utilized for computation [89][92][93]. One way to realize LBMs is to fashion them out of nearly circular ultrathin disks of small cross-section, resulting in low shape anisotropy energy barrier on the order of the thermal energy kT. These nanomagnets have in-plane magnetic anisotropy (IMA) and they may have an advantage over those with perpendicular magnetic anisotropy in BSNs [10]. If the normalized magnetization component $m_z(t)$ along any one direction (say, the z-direction) is monitored on the surface of the LBM, it will randomly vary between -1 and +1 with time $t$ because of thermal noise.

## 5.2 LBM Design Parameters and Their Sensitivity

Ref. [10] recently discussed the design of LBMs for binary stochastic neurons (BSN) and focused on two important parameters that govern the BSN operation: the correlation time $\tau_c$ and the pinning

current $I_p$. The former is the *full width at half maximum* of the temporal autocorrelation function which we define as

$$C(\tau) = \int\limits_{-\infty}^{\infty} dt \left[ m_z(t) m_z(t+\tau) \right], \qquad (1)$$

where $m_z(t)$ is the magnetization component along any chosen direction (say, the z-direction) at any time $t$. The latter is the magnitude of the spin-polarized current needed to pin the magnetization in the direction of the spin-polarization of the current due to spin transfer torque within a specified time. These two parameters are crucial in designing LBMs for BSNs. So in this chapter the design challenges of real LBMs due to sensitivity of $\tau_c$ and $I_p$ to small *fabrication defects* are explored. Strong sensitivity make the design of LBMs for BSNs extremely challenging since $\tau_c$ and $I_p$ would become unpredictable, given that defects are unpredictable. Particularly, the response time of BSNs, which is dependent on $\tau_c$, will vary randomly if the fabrication process is not well-controlled. This could be debilitating for BSN applications of LBMs and make LBMs unsuitable for BSNs. This study is carried out to examine this possibility. Finally the power spectral densities of magnetization fluctuations in amorphous nanomagnets with low shape anisotropy energy barriers on the order of the thermal energy kT is computed. They are also important since low barrier nanomagnets are attracting increasing attention for applications in stochastic computing.

## 5.3 Simulation Procedure

The simulation for the magnetization dynamics in a low barrier nanomagnet (LBM) made of cobalt is carried out using Mumax3. The LBM is a thin elliptical disk of small eccentricity (nearly circular) whose major axis dimension is 100 nm, minor axis dimension is 99.7 nm and thickness 6 nm. The calculated shape anisotropy energy barrier is 1.3 kT at room temperature because of the small eccentricity. We start with the magnetization having components

$\left[ m_z\left(t=0\right)=0.99;\ m_x\left(t=0\right)=0.141;\ m_y\left(t=0\right)=0 \right]$ initially, with the *z*-axis being along the major axis, and simulate its temporal evolution in the presence of a random thermal field given by

$$\vec{H}_{th}\left(t\right)=H_x\left(t\right)\hat{x}+H_y\left(t\right)\hat{y}+H_z\left(t\right)\hat{z}$$
$$H_i\left(t\right)=\sqrt{\frac{2\alpha kT}{\gamma\left(1+\alpha^2\right)\mu_0 M_s \Omega \Delta t}}G_{0,i}^i\left(t\right)\qquad \left(i=x,y,z\right) \quad , \quad (2)$$

where α is the Gilbert damping factor of cobalt (α = 0.01), $G_{0,i}^i\left(t\right)$ is a Gaussian of zero mean and unit standard deviation, $\gamma=2\mu_B\mu_0/\hbar$ , μB is the Bohr magneton, μ0 is the permeability of free space, $M_s$ is the saturation magnetization of cobalt ($1.1\times10^6$ A/m) [94], Ω is the nanomagnet volume and Δ*t* is the time step used in the simulation (0.1 ps). We ignore magneto-crystalline anisotropy, assuming that the nanomagnet is amorphous. The simulation is carried out with the micromagnetic simulator MuMax3 [30]. We assumed that the exchange constant of cobalt is $3\times10^{-11}$ J/m [95]. The simulation is carried out for 1 ns, which provides more than enough statistics to calculate the auto-correlation function in Equation (1). All calculations are carried out for room temperature (300 K). In this study, the temporal dynamics of the magnetization in a defect-free nanomagnet (C0) and nanomagnets with six different types of defects (C1-C6) is simulated as shown in Fig. 5.1. These defects are commonplace in nanomagnets that have been fabricated in our lab with electron-beam patterning of a resist, followed by development, evaporation of (ferromagnetic) metal and lift-off as shown in Fig. 3.1 of the Chapter 3 which shows atomic force micrographs of such fabricated nanomagnets. The idealizations in Fig. 4.1 closely approximate some of the defects observed experimentally. The MuMax3 simulations allow us to determine the normalized magnetization component $m_z\left(t\right)$ at any instant of time *t* in any nanomagnet, and that allows us to calculate all quantities of interest.
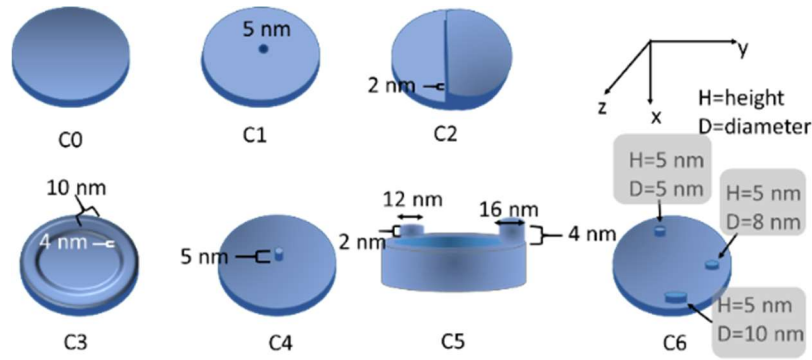
Fig. 5.1: Defect-free and defective nanomagnets. The dimensions of the nanomagnets are: major axis = 100 nm, minor axis = 99.7 nm, thickness = 6 nm. C1 has a 5-nm diameter hole in the center. C2 has two halves with two different thicknesses – one with a thickness of 6 nm and the other with a thickness of 8 nm. C3 has an annulus along the circumference of width 10 nm and height 4 nm. C4 has a cylindrical hillock in the center of diameter 5 nm and height 5 nm. C5 is similar to C3, except the width and height of the annulus varies at two arbitrary locations. In one location the annulus is replaced by a cylinder 8 nm tall and 16 nm in diameter and in another location by a cylinder 6 nm tall and 12 nm in diameter. The defect C6 consists of cylinders of arbitrary dimensions located at arbitrary locations on the surface. This emulates random surface roughness. This figure is not to scale.

## 5.4 Results and Discussion

In Fig. 5.2, the autocorrelation function [Equation (1)] for a defect-free nanomagnet (C0) along with those for nanomagnets with defects C1-C6 is plotted. Clearly, there are vast differences between the auto-correlation functions for a defect-free nanomagnet and some defective nanomagnets. Table 5.1 lists the correlation times $\tau_c$ calculated for the defect-free and defective nanomagnets. The magnitudes of the (perpendicular-to-plane) spin-polarized current which stabilizes (or pins) the magnetization in the direction of the spin polarization of the current owing to spin transfer torque is also obtained from the simulation data. The pinning current will depend on the time allocated for the pinning to occur, which we have arbitrarily chosen to be 5 ns. It is found that the pinning currents for the defect-free and defective nanomagnets to assess how much defects influence the pinning current.
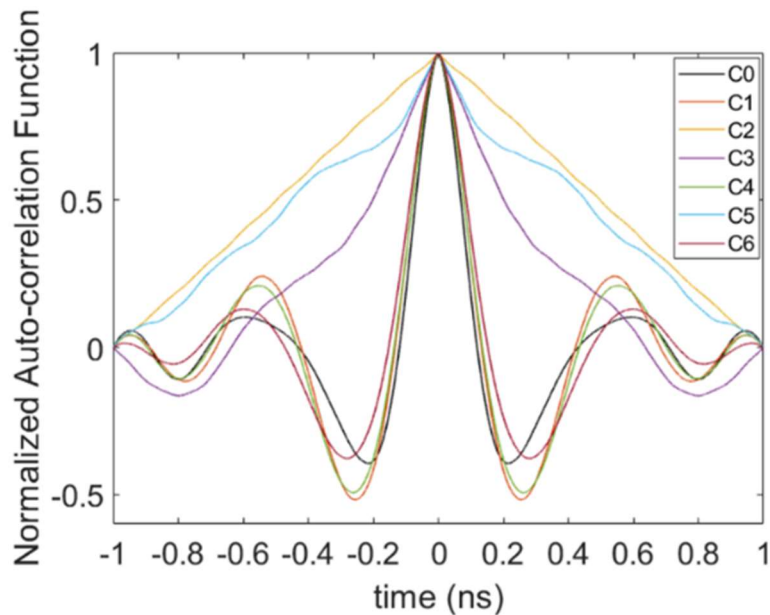
Fig. 5.2: The normalized temporal auto-correlation functions (defined in Equation (1)) plotted as a function of time for defect-free and defective LBMs. All LBMs in this plot are nominally identical, except they have different defects. Their auto-correlation functions are very different – both qualitatively and quantitatively – showing that this parameter is unpredictable in real LBMs that have random defects. Single (C1 and C4), and multiple (C6) *localized* defects do not change the auto-correlation functions by much, but *delocalized* (extended) defects (C2, C3 and C5) affect the auto-correlation functions drastically.

Table 5.1: Correlation times $\tau_c$ for various defects

| Type of defect | Correlation time (ns) |
|:---:|:---:|
| C0 | 0.139 |
| C1 | 0.158 |
| C2 | 0.995 |
| C3 | 0.403 |
| C4 | 0.157 |
| C5 | 0.905 |
| C6 | 0.173 |

To find the pinning currents, a 100% spin polarized current is passed, whose spin polarization is in the –z direction, perpendicular to the plane of the nanomagnet. The current is assumed to retain its spin polarization throughout the magnet since the spin diffusion length in cobalt at room temperature is $38 \pm 12$ nm [96] and the magnet thickness is only 6 nm. We pass the current for 5 ns (which would be the typical clock period in a neural circuit) and plot the z-component of

magnetization as a function of the current magnitude at the completion of 5 ns of current passage (i.e. at the end of the assumed clock period). This is shown in Figure 5.3.
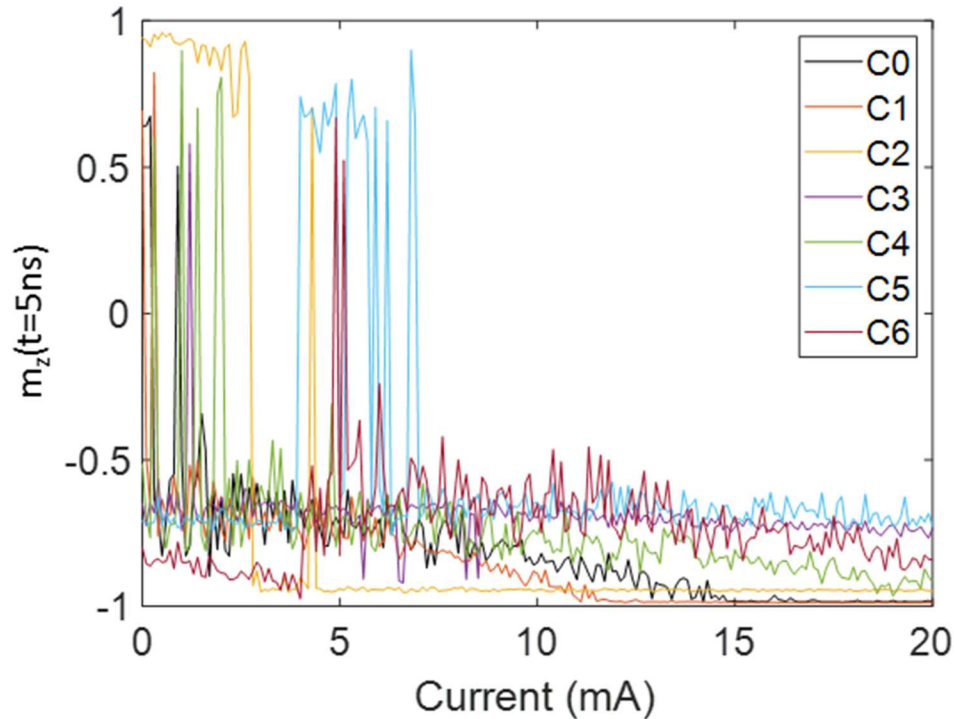


Fig. 5.3 : Normalized magnetization component in the direction opposite to that of current spin polarization after 5 ns of current passage as a function of the current magnitude for defect-free and defective nanomagnets.

The pinning current is the minimum current that can pin the magnetization close to the –z-direction (direction of the current's spin polarization) within the allotted 5 ns. At low values of the current, the magnetization component does not settle to the –z-direction definitively after 5 ns, but it does so beyond a threshold current (except for some defects), and this threshold current is the "pinning current".

In Fig. 5.3, we see that the normalized magnetization component in the direction of pinning at the end of 5 ns of current passage [$m_z$(t=5 ns)] fluctuates (between almost -1 and +1) at low current levels, i.e. the magnetization does not pin *monotonically* with increasing current. This feature is

not just due to thermal noise, although noise also plays a role. It is a consequence of the magneto-dynamics which consists of precession and damping. When the current is turned on, the magnetization begins to precess and gradually align along the pinning direction owing to the damping caused by the current. At low current levels, the damping is weak and hence the precession would not have died out within 5 ns. If we take a snapshot at the end of 5 ns, the magnetization component in the pinning direction [$m_z$(t=5 ns)] will depend on what angle the magnetization has rotated through at the end of 5 ns and that depends on the interplay between the precessional and damping dynamics, which does not have a monotonic dependence on current. As a result, $m_z$(t=5 ns) need not vary monotonically with current and the pinning need not occur monotonically. Thermal noise exacerbates this effect, resulting in the low current fluctuations seen in Fig. 5.3. At high current levels (large Slonczewski torque), the damping is strong enough to have aligned the magnetization in the pinning direction after 5 ns, which is why we would not see the fluctuations at higher current. It is also observed that for defects C3 and C5, the magnetization does not settle in the direction of the current's spin polarization, i.e. $m_z \approx -1$, after 5 ns, even when the current is as large as 20 mA. Instead the z-component of the magnetization seems to saturate to a value that is approximately – 0.7, after the current exceeds ~8 mA. The y-component however does not saturate and continues to change if we vary the current (no pinning). For defect C6, the z-component does not settle into any value up to a current of 20 mA, but clearly trends towards a value of -1 as the current is increased (it might ultimately settle at close to -1, i.e. get pinned, if the value of current exceeded above 20 mA). For all other defects, (and the defect-free nanomagnet), the z-component of the magnetization does settle to a value close to -1 (indicating that the magnetization has been pinned in the direction of the current's spin polarization) after the current exceeds a threshold value. Clearly, for defects C3 and C5 (C5 is similar to C3 in geometry),

current up to 20 mA cannot pin the magnetization in the direction of the spin polarization of the current (i.e. make $m_z \approx -1$) in 5 ns, indicating that there may be no reasonable pinning current for these types of defect, if no more than 5 ns is allowed for pinning. These types of defects may not allow pinning within a reasonable time with a reasonable current. On the other hand, defect C6, which represents surface roughness, may allow pinning at the end of 5 ns, but would require a very large current (> 20 mA). Thus, the pinning current magnitude – or if pinning is even possible – within a given time depends on the nature of the defects. Defects can either increase or decrease the pinning current, which can vary over almost an order of magnitude because of the defects. This attests to the unpredictability of the pinning current when defects are present. Table 5.2 lists the pinning currents (for 5 ns pinning duration) for various types of defects which are determined from Figs. 5.3. In Fig. 5.4, the time variation of the z-component of the magnetization (between 0 and 5 ns) is plotted for the defect-free and defective nanomagnets when the corresponding pinning current (taken from Table 5.2) is injected to align the magnetization in the direction of the current's spin polarization. In the case of defects C3 and C5, there is no pinning. So, the minimum current that stabilizes the z-component of the magnetization (albeit not in the desired direction) is used.

Table 5.2: Pinning currents for various defects that pin within 5 ns

| Type of defect | Pinning Current (mA) |
| --- | --- |
| C0 | 14.8 |
| C1 | 11.9 |
| C2 | 3.1 |
| C3 | --- |
| C4 | 19 |
| C5 | --- |
| C3 | >20 |
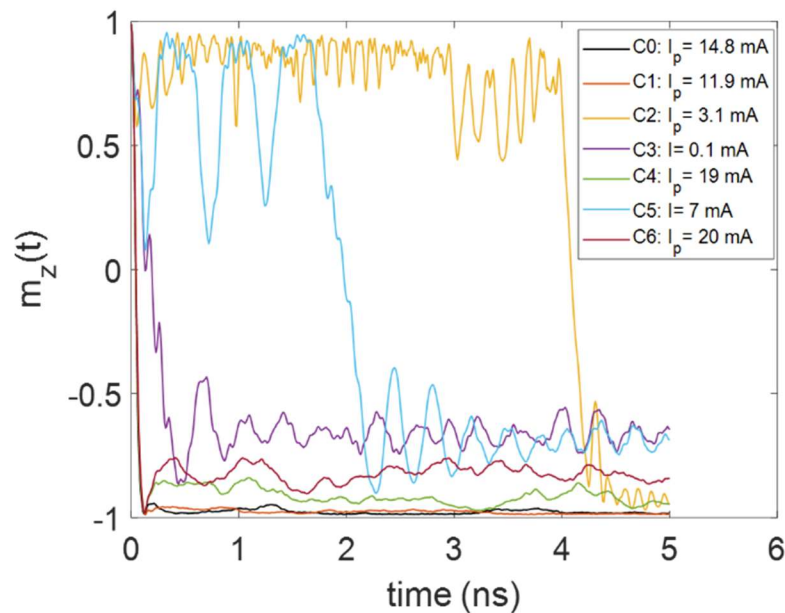
Fig. 5.4: Normalized magnetization component in the direction of spin polarization of the injected current as a function of time at different current magnitudes for the seven different types of nanomagnets (defective and defect-free).

Note that for all defects except C2 and C5, the z-component of the magnetization saturates to a steady-state value very quickly (<0.5 ns) when the pinning current is passed. The defect C2 takes much longer (>4.3 ns) and C5 takes > 2 ns. C2 has two different thicknesses in two different halves and is an extended (delocalized) defect like C3, C5 and C6. This plot shows that the "pinning time" is also affected by defects.

Next, the power spectral densities of magnetization fluctuations in amorphous nanomagnets with low shape anisotropy energy barriers on the order of the thermal energy kT is computed. Three interesting features have emerged from these calculations: (i) the fluctuations produce colored noise with a prominent spectral peak, (ii) the peak frequency and the spectrum are almost independent of the energy barrier height in the nanomagnet, and (iii) small localized structural defects in the nanomagnets do not affect the power spectrum significantly, although extended defects do. These results show that the power spectrum of the magnetization fluctuation is

surprisingly robust against small variations in the energy barrier height and the presence of localized structural defects in a low barrier nanomagnet.

In Fig. 5.5, the auto-correlation functions and power spectral densities (PSDs) of the magnetization fluctuations of two LBMs with slightly different dimensions having energy barriers of 1.3 kT and 2.2 kT are shown. According to the Wiener-Khinchin Theorem, the power spectral density of the magnetization fluctuation is the Fourier transform of the auto-correlation function:

$$S(f) = \int_{-\infty}^{\infty} d\tau\, C(t) e^{-i2\pi f} \qquad (3)$$

Note that even though the barrier heights differ by ~70%, the auto-correlation functions differ very slightly, showing that it is relatively insensitive to barrier height. The auto-correlation function therefore cannot be engineered by engineering the barrier height since the latter has very little effect.
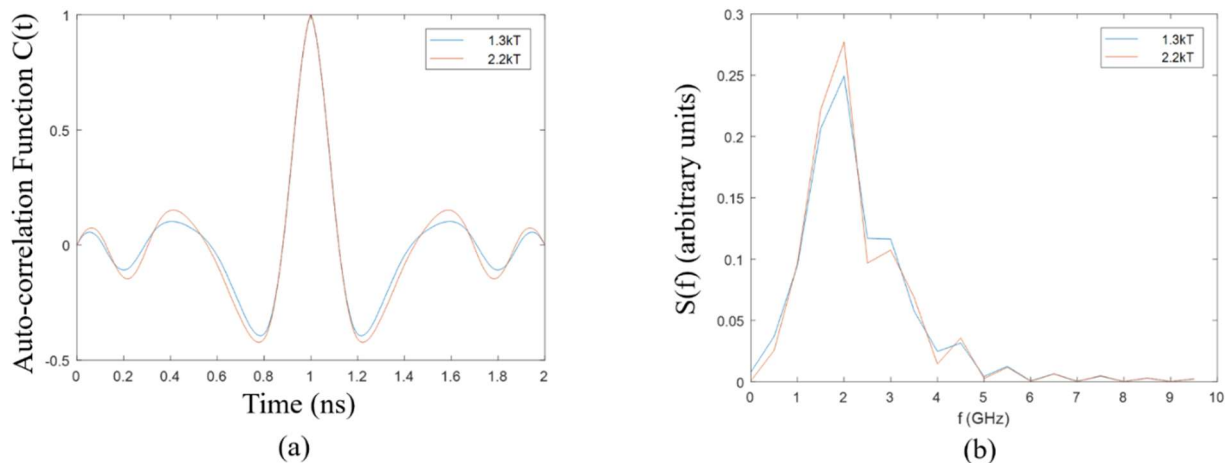


Fig. 5.5: (a) Normalized auto-correlation functions of two LBMs with energy barriers of 1.3 kT and 2.2 kT, (b) Power spectral densities of two LBMs with energy barriers of 1.3 kT and 2.2 kT.

The PSDs are practically indistinguishable, showing that the power spectra of the magnetization fluctuations are not particularly sensitive to the energy barrier height. Fig. 5.6 also shows that the noise associated with the magnetization fluctuation is "colored" with a well-defined peak that is,

again, fairly insensitive to the barrier height. These results show that the power spectrum of the magnetization fluctuations is robust against reasonable variations in the energy barrier height. Finally, it is investigated that if the power spectrum can be affected by the presence of structural defects in the nanomagnets. To this end, four different types of structural defects depicted are considered in the insets of Fig 5.6. The power spectra do not change much in the presence of localized defects, but change very significantly when extended defects are present.
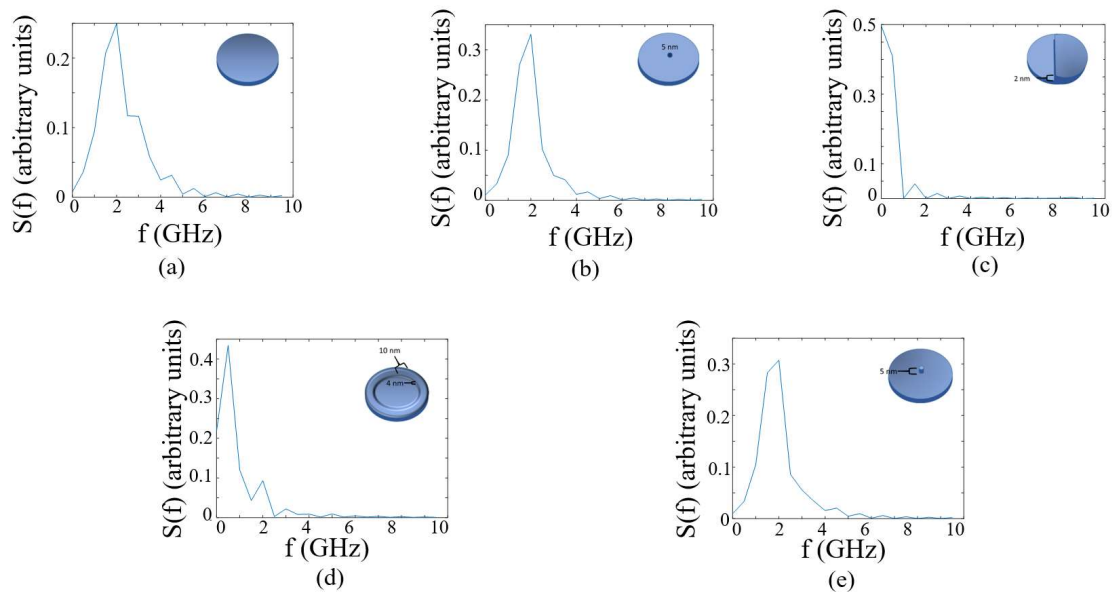


Fig. 5.6: Power spectral densities for: (a) defect-free nanomagnet, (b) a defective nanomagnet with a 5-nm diameter through hole in the center, (c) a defective nanomagnet where the thickness in one half is 6 nm and the other 8 nm, (d) a defective nanomagnet with an annulus around the periphery whose width is 10 nm and height 4 nm, and (e) a defective nanomagnet with a 5 nm diameter and 5 nm tall cylindrical hillock at the center.

## 5.5 Conclusion

In this chapter. it is shown that defects can increase or decrease both the correlation time $\tau_c$ and the pinning current $I_p$ and make them vary randomly by nearly an order of magnitude. That makes the parameters of BSNs designed with LBMs very difficult to control. Either LBMs will have to be fabricated with extremely tight control (defect-free) or they may suffer from poor yield. Ref.

[10] discussed a different genre of BSNs that are controlled more by transistor characteristics than nanomagnet characteristics. They may be more immune to fabrication defects than those which rely critically on nanomagnet characteristics. So to conclude, this study has shown that unavoidable fabrication defects may introduce wide variability in the characteristics of LBMs that are utilized in BSNs [10] or other constructs like analog-to-digital converters [89]. While stochastic computing is generally more tolerant of variabilities than deterministic computing (e.g. Boolean computing) [97], whether variability spanning an order of magnitude is tolerable remains an open question and needs to be addressed. Some defects are more harmful than others; for example, the defect of type C3 (rim around the circumference) or C5 (which is similar to C3), does not even allow one to pin the magnetization with any reasonable current in a reasonable time. Generally speaking, extended (delocalized) defects like C2, C3, C5 affect the auto-correlation function much more than localized defects like C1, C4 and C6, and consequently they have a much more severe effect on the correlation time. Delocalized defects may be less common than the localized ones, but their effect is also much more debilitating, and that makes them more of a concern than localized defects. Finally, it is shown that the noise associated with random fluctuations of the magnetization in a low barrier nanomagnet due to Gaussian thermal noise is colored with a well-defined peak. The noise spectrum is quite insensitive to changes in the barrier height and is also not much affected by localized defects, but they are affected very perceptibly by extended defects. In the past, we have shown that defects can significantly affect switching characteristics of [8] and spin wave modes [9] in nanomagnets with large energy barriers (few tens of kT). Here, it is shown that localized defects have little effect on the power spectral densities of magnetization fluctuations in nanomagnets of low barrier (~kT), although extended defects have a much more significant effect.

# Chapter 6: A Proposal of Microwave Oscillator Based on a Single Straintronic Magneto-tunneling Junction

There is growing interest in exploring nanomagnetic devices as potential replacements for electronic devices (e.g. transistors) in digital switching circuits and systems. A special class of nanomagnetic devices are switched with electrically generated mechanical strain leading to electrical control of magnetism. Straintronics is the field of switching the magnetization of a magnetostrictive nanomagnet, elastically coupled to an underlying piezoelectric film, with mechanical strain generated by applying a small voltage across the piezoelectric. This phenomenon can be exploited to realize extremely energy-efficient binary switches and a host of other digital systems that dissipate miniscule amounts of energy to operate [98]. What is less known, however, is that these same systems have another striking advantage, namely, their device characteristics may allow for combining the functionalities of multiple traditional devices into one single element. That would reduce device count significantly in both analog and digital circuits. Recently, it was shown theoretically that a *single* straintronic magneto-tunneling junction (s-MTJ), whose soft layer is a two-phase multiferroic composed of a magnetostrictive layer and a piezoelectric layer, can implement a ternary content-addressable memory cell [99] which would normally require 16 transistors to implement [100]. A single s-MTJ can also implement restricted Boltzmann machines which are unsupervised learning models of computation suitable to extract features from high-dimensional data [85].

In this chapter, it is shown that a *single* straintronic magneto-tunneling junction with a passive resistor can act as a microwave oscillator whose traditional implementation would have required microwave operational amplifiers, capacitors and resistors [101]. In contrast, a *single* s-MTJ (Fig. 6.1) can realize the same functionality with just a single passive resistor. This reduces device footprint and cost, while improving device reliability. This is a new analog application of magnetic devices where magnetic interactions (interaction between the shape anisotropy, strain anisotropy,

dipolar coupling field and spin transfer torque in the soft layer of the s-MTJ) are exploited to implement an oscillator with reduced footprint.

Magneto-tunneling junctions have been used extensively in the past for microwave spin-torque nano-oscillators (STNO) [102] which rely on magnetization precession induced by a spin polarized current. The principle of operation of the device analyzed here is different and relies on a feedback between strain, dipole coupling, shape anisotropy and spin polarized current delivering spin transfer torque in the soft layer of an MTJ. Unlike STNOs which typically have quality factors (ratio of resonant frequency to bandwidth) of 10 or less [102], the device presented here theoretically has a quality factor exceeding 50 according to the results of our simulations. This is due to the narrow bandwidth which is caused by the fact that the oscillations are spectrally pure (almost sinusoidal). The high quality factor is a significant advantage in antenna applications because it leads to higher radiation efficiency.

## 6.1 Working Principle of Straintronic Microwave Oscillator

To understand how a single s-MTJ can implement microwave oscillator, consider the s-MTJ in Fig. 6.1 whose hard and soft layers have in-plane magnetic anisotropy. The two layers are shaped into elliptical disks and their major axes (easy axes) are collinear. The hard layer is permanently magnetized in one direction along its major axis (along the +y-axis). It is made of a synthetic anti-ferromagnet and engineered to produce a weak (but non-zero) dipole coupling field on the soft layer. In this configuration, the dipole coupling field in the soft layer is constant and oriented along the latter's major axis in the direction opposite to the magnetization of the hard layer [103], i.e. along the –y-direction. Therefore, we can write the dipole coupling field as

$$\vec{H}_{\text{dipole}} = -H_d \hat{y} \qquad (1)$$

where $H_d$ is a constant that depends on the composition of the hard layer.
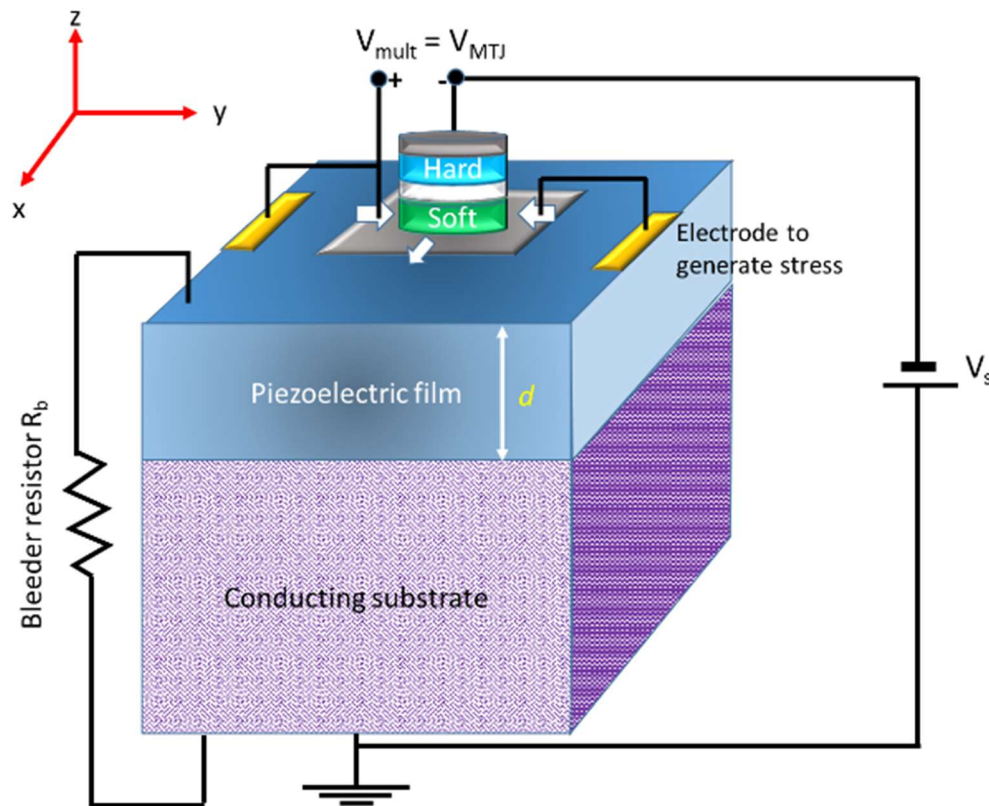


Fig. 6.1: A microwave oscillator implemented with a single straintronic magneto-tunneling junction (MTJ) and a passive resistor. The output voltage of the device is $V_{mult}$ which is the voltage dropped over the MTJ. The strain generated in the elliptical MTJ soft layer due to the voltage dropped over the piezoelectric is biaxial (compressive along the major axis and tensile along the minor axis). The white arrows show the strain directions. The piezoelectric layer is poled in the vertically up direction. The lateral dimension of the soft layer, the spacing between the edge of the soft layer and the nearest electrode, and the piezoelectric film thickness are all approximately the same and that generates biaxial strain in the soft layer [23].

When no current is passing through the s-MTJ, the magnetizations of the hard and soft layers will be mutually antiparallel owing to the dipole coupling field and the MTJ will be in the high resistance state. If we now turn on the voltage supply $V_s$ (with the polarity shown in Fig. 1b), spin-polarized electrons will be injected from the hard layer into the soft layer and they will gradually turn the soft layer's magnetization in the direction of the hard layer's magnetization because of the generated spin transfer torque. This will take the MTJ toward the low resistance state.

Note that the voltage dropped over the piezoelectric film is

$$V_{piezo} = \frac{R_{piezo}\|R_b}{R_{piezo}\|R_b+R_{MTJ}} \qquad (2)$$

where $R_{piezo}$ is the resistance of the piezoelectric film between the s-MTJ soft layer and the conducting substrate, $R_b$ is the resistance of a current bleeder resistor in parallel with the piezoelectric film as shown in Fig. 1, and $R_{MTJ}$ is the resistance of the s-MTJ. The resistance of the conducting substrate is assumed to be negligible. Equation (2) shows that when the s-MTJ goes into the low resistance state $(R_{MTJ} \rightarrow \text{low})$, the voltage dropped over the piezoelectric film $V_{piezo}$ increases and that generates sufficient strain in that film which is partially transferred to the soft layer. Since the soft layer is magnetostrictive, this strain will rotate its magnetization away from the major axis toward the minor axis because of the Villari effect, as long as the product of the strain and magnetostriction coefficient is negative (i.e. strain will have to be compressive if the magnetostriction coefficient of the soft layer is positive and tensile if the magnetostriction coefficient is negative). This rotation, which increases the angle between the magnetizations of the hard and soft layer, will increase the resistance of the MTJ and reduce the spin polarized current flowing through it (for a constant supply voltage $V_s$). At that point, the dipole coupling effect can overcome the reduced spin transfer torque associated with the reduced current and swing the soft layer's magnetization toward an orientation antiparallel to that of the hard layer, causing the MTJ resistance to approach the high resistance state. Once that happens, the voltage dropped over the piezoelectric film falls (see Equation (2) again) and the strain in the soft layer subsides. However, the spin polarized current still flows through the soft magnet, and over sufficient time, will transfer enough torque to the soft layer's magnetization to make it once again attempt to align parallel to the hard layer's magnetization. This will take the MTJ back to the low resistance state and the

process repeats itself. The MTJ resistance $R_{MTJ}$ therefore continuously oscillates between the high and low states. This will make the voltage $V_{MTJ}$ dropped over the MTJ $\left[ V_{MTJ} = \dfrac{V_S R_{MTJ}}{(R_{piezo}\|R_b + R_{MTJ})} \right]$ also continuously oscillate between two values, resulting in an oscillator. This is operating principle of the s-MTJ based oscillator.

## 6.2 Simulation Procedure and Material Used

In order to simulate the temporal dynamics of the oscillator, the magnetodynamics of the soft layer under the combined effects of strain anisotropy, shape anisotropy, dipolar coupling field and spin transfer torque is introduced and simulated. This will yield the time variations of $R_{MTJ}$ and $V_{MTJ}$, which is the output of the oscillator. To do this, the stochastic Landau-Lifshitz-Gilbert (LLG) equation is solved, assuming that the magneto-dynamics of the soft layer can be described within the macrospin approximation. It is understood that the soft layer can be multi-domain, but we avoided the more accurate stochastic micromagnetic simulations in the presence of thermal noise since it will overwhelm our computational resources and would produce only small quantitative differences, while the qualitative results will not change. The LLG equation describing the magnetodynamics of the soft layer is:

$$\frac{d\vec{m}(t)}{dt} = -\gamma \vec{m}(t) \times \vec{H}_{\text{total}}(t) + \alpha \left( \vec{m}(t) \times \frac{d\vec{m}(t)}{dt} \right) + a\vec{m}(t) \times \left( \frac{\eta \vec{I}_s(t)\mu_B}{q M_s \Omega} \times \vec{m}(t) \right) + b\frac{\eta \vec{I}_s(t)\mu_B}{q M_s \Omega} \times \vec{m}(t) \tag{3}$$

where

$$\hat{m}(t) = m_x(t)\hat{x} + m_y(t)\hat{y} + m_z(t)\hat{z} \qquad \left[ m_x^2(t) + m_y^2(t) + m_z^2(t) = 1 \right]$$

$$\vec{H}_{\text{total}} = \vec{H}_{\text{demag}} + \vec{H}_{\text{stress}} + \vec{H}_{\text{dipole}} + \vec{H}_{\text{thermal}}$$

$$\vec{H}_{\text{demag}} = -M_s N_{d-xx} m_x(t)\hat{x} - M_s N_{d-yy} m_y(t)\hat{y} - M_s N_{d-zz} m_z(t)\hat{z}$$

$$\vec{H}_{\text{stress}} = \frac{3}{\mu_0 M_s} \left( \lambda_s \sigma_{yy}(t) m_y(t) \right) \hat{y}$$

$$\vec{H}_{\text{dipole}} = -H_d \hat{y} \qquad \left[ \text{constant independent of time} \right]$$

$$\vec{H}_{\text{thermal}} = \sqrt{\frac{2\alpha kT}{\gamma(1+\alpha^2)\mu_0 M_s \Omega(\Delta t)}} \left[ G^x_{(0,1)}(t)\hat{x} + G^y_{(0,1)}(t)\hat{y} + G^z_{(0,1)}(t)\hat{z} \right]$$

The last term in the right-hand side of Equation (3) is the field-like spin transfer torque and the second to last term is the Slonczewski torque. The coefficients $a$ and $b$ depend on device configurations and following [104], we will use the values $a=1$, $b=0.3$. Here $\hat{m}(t)$ is the time-varying magnetization vector in the soft layer normalized to unity, $m_x(t)$, $m_y(t)$ and $m_z(t)$ are its time-varying components along the x-, y- and z-axis, $\vec{H}_{\text{demag}}$ is the demagnetizing field in the soft layer due to shape anisotropy, $\vec{H}_{\text{stress}}$ is the magnetic field caused by stress in the magnetostrictive soft layer, $\vec{H}_{\text{dipole}}$ is the dipole coupling field given in Equation (1) and $\vec{H}_{\text{thermal}}$ is the random magnetic field due to thermal noise. The different parameters in Equation (3) are: $\gamma = 2\mu_B\mu_0/\hbar$, $\alpha$ is the Gilbert damping constant, $\mu_0$ is the magnetic permeability of free space, $M_s$ is the saturation magnetization of the magnetostrictive soft layer, $kT$ is the thermal energy, $\lambda_s$ is the magnetostriction coefficient of the soft layer, $\Omega$ is the volume of the soft layer which is given by $\Omega = (\pi/4)a_1a_2a_3$ $[a_1 = \text{major axis}, a_2 = \text{minor axis and } a_3 = \text{thickness}]$, $\sigma_{yy}(t)$ is the uniaxial time-varying stress created in the soft layer by the voltage dropped over the piezoelectric film, $\Delta t$ is the time step used in the simulation, and $G^x_{(0,1)}(t)$, $G^x_{(0,1)}(t)$ and $G^x_{(0,1)}(t)$ are three uncorrelated Gaussians with zero mean and unit standard deviation [78]. The quantities $N_{d-xx}, N_{d-yy}, N_{d-zz}$ $\left[ N_{d-xx} + N_{d-yy} + N_{d-zz} = 1 \right]$ are calculated from the dimensions of the elliptical soft layer following the prescription of ref. [94]. We assume that the charge current injected from the hard layer into the soft layer is $\vec{I}_s(t)$ and that the spin polarization in the current is $\eta$. The spin current is given by

$$\eta\vec{I}_s(t) = \eta|\vec{I}_s(t)|\hat{y} \quad \text{where} \quad |\vec{I}_s(t)| = \frac{V_s}{R_{MTJ}(t) + R_{piezo}\|R_b} = \frac{V_s}{R_P + \frac{\Delta R}{2}(1 - m_y(t)) + R_{piezo}\|R_b}. \quad (4)$$

Here, $R_P$ is the low resistance of the MTJ (when the magnetizations of the hard and soft layers are closest to being parallel) and $R_{AP}$ is the high resistance when the two magnetizations are closest to being anti-parallel. The quantity $\Delta R = R_{AP} - R_P$. The stress generated in the soft layer is actually biaxial (compressive along the major axis and tensile along the minor axis for the power supply voltage polarity shown in Fig. 6.1, as long as the piezoelectric is poled in the vertically down direction). The conditions for such stress generation, discussed extensively in ref. [23], are stated in the caption of Fig. 6.1. Since the effect of biaxial stress is difficult to incorporate in the LLG equation, we have approximated the stress as uniaxial along the major axis. Note that tensile stress along the minor axis has the same effect on magnetization as compressive stress along the major axis (and vice versa); hence, we can combine the two effects into the effect of a single uniaxial stress along the major axis. The uniaxial strain generated in the piezoelectric is the product of the electric field in the piezoelectric film along its thickness (generated by $V_{piezo}$) and its $d_{31}$ coefficient, and we assume that it is fully transferred to the soft layer. The uniaxial stress in the soft layer is therefore given by

$$\sigma_{yy}(t) = d_{31} Y \frac{R_{piezo}\|R_b}{R_{piezo}\|R_b + R_{MTJ}(t)} \frac{V_s}{d} = d_{31} Y \frac{R_{piezo}\|R_b}{R_{piezo}\|R_b + R_P + \frac{\Delta R}{2}\left(1 - m_y(t)\right)} \frac{V_s}{d} \qquad , \qquad (5)$$

where $d$ is the thickness of the piezoelectric film and $Y$ is the Young's modulus of the soft layer material. Finally, the voltage drop over the s-MTJ, is the *oscillator output voltage* and it is given by

$$V_{\text{oscillator}}(t) = V_{MTJ}(t) = V_s \frac{R_{MTJ}(t)}{R_{piezo}\|R_b + R_{MTJ}(t)} = V_s \frac{R_p + (\Delta R/2)\left(1 - m_y(t)\right)}{R_{piezo}\|R_b + R_p + (\Delta R/2)\left(1 - m_y(t)\right)}. \qquad (6)$$

We will assume a tunneling magnetoresistance ratio (TMR) of 500% [5], which will make

$\Delta R = 5R_p$. Using the vector identity $\vec{a} \times (\vec{b} \times \vec{c}) = \vec{b}(\vec{a} \bullet \vec{c}) - \vec{c}(\vec{a} \bullet \vec{b})$, we can recast the vector

equation in Equation (3) as

$$\left(1+\alpha^2\right)\frac{d\vec{m}(t)}{dt} = -\gamma\left(\vec{m}(t) \times \vec{H}_{\text{total}}(t)\right) - \gamma\alpha\left[\vec{m}(t)\left(\vec{m}(t) \bullet \vec{H}_{\text{total}}(t)\right) - \vec{H}_{\text{total}}(t)\right]$$
$$- \left(\alpha a - b\right)\left(\frac{\eta\vec{I}_s(t)\mu_B}{qM_s\Omega} \times \vec{m}(t)\right) + \left(a + \alpha b\right)\frac{\eta I_s(t)\mu_B}{qM_s\Omega}\left[\hat{y} - \vec{m}(t)m_y(t)\right]. \quad (7)$$

This vector equation can be recast as three coupled scalar equations in the three Cartesian

components of the magnetization vector:

$$(1+\alpha^2)\frac{dm_x(t)}{dt} = -\gamma\left[m_y(t)H_z(t) - m_z(t)H_y(t)\right] - \alpha\gamma\left[m_x(t)\left[m_x(t)H_x(t) + m_y(t)H_y(t) + m_z(t)H_z(t)\right] - H_x(t)\right]$$
$$- (a\alpha - b)\frac{\eta I_s(t)m_z(t)\mu_B}{qM_s\Omega} - (a + \alpha b)\frac{\eta I_s(t)m_x(t)m_y(t)\mu_B}{qM_s\Omega}$$

$$(1+\alpha^2)\frac{dm_y(t)}{dt} = -\gamma\left[m_z(t)H_x(t) - m_x(t)H_z(t)\right] - \alpha\gamma\left[m_y(t)\left[m_x(t)H_x(t) + m_y(t)H_y(t) + m_z(t)H_z(t)\right] - H_y(t)\right], \quad (8)$$
$$+ (a + \alpha b)\frac{\eta I_s(t)\mu_B}{qM_s\Omega}(1 - m_y^2(t))$$

$$(1+\alpha^2)\frac{dm_z(t)}{dt} = -\gamma\left[m_x(t)H_y(t) - m_y(t)H_x(t)\right] - \alpha\gamma\left[m_z(t)\left[m_x(t)H_x(t) + m_y(t)H_y(t) + m_z(t)H_z(t)\right] - H_z(t)\right]$$
$$+ (a\alpha - b)\frac{\eta I_s(t)m_x(t)\mu_B}{qM_s\Omega} - (a + \alpha b)\frac{\eta I_s(t)m_z(t)m_y(t)\mu_B}{qM_s\Omega}$$

where

$$H_x = -M_s N_{d-xx} m_x(t) + \sqrt{\frac{2\alpha kT}{\gamma(1+\alpha^2)\mu_0 M_s \Omega(\Delta t)}}G^x_{(0,1)}(t)$$

$$H_y = -M_s N_{d-yy} m_y(t) + \sqrt{\frac{2\alpha kT}{\gamma(1+\alpha^2)\mu_0 M_s \Omega(\Delta t)}}G^y_{(0,1)}(t) + \frac{3}{\mu_0 M_s}\left(\lambda_s \sigma_y(t) m_y(t)\right)\hat{y} - H_d\hat{y} \quad . \quad (9)$$

$$H_z = -M_s N_{d-zz} m_z(t) + \sqrt{\frac{2\alpha kT}{\gamma(1+\alpha^2)\mu_0 M_s \Omega(\Delta t)}}G^z_{(0,1)}(t)$$

The quantity $\Delta t$ is the time step used in solving Equation (8) numerically. Equation (8) is solved

numerically to find the magnetization component $m_y(t)$ as a function of time and then use Equation

(6) to find $V_{\text{oscillator}}(t)$ as a function of time. In the simulation, $\Delta t = 0.1$ ps is taken and it is verified

that a smaller value does not change anything perceptibly. It is assumed that the soft layer of the

MTJ is made of Terfenol-D and used the material and device parameters in Table 6.1. The hard

layer (fashioned out of a synthetic antiferromagnet, such as FeCoB with Rh spacer layers [105])

has the same geometry as the soft layer. The adhesion layer at the bottom of the MTJ stack is

assumed to be thin enough to not impede strain transfer from the underlying piezoelectric into the

soft layer. The top layer above the hard layer is intended to prevent oxidation of the hard layer.

**Table 6.1: Material and device parameters**

| | |
|---|---|
| Saturation magnetization ($M_s$) | $8 \times 10^5$ A/m |
| Magnetostriction coefficient $\lambda_s$) | $600 \times 10^{-6}$ |
| s-MTJ resistance in the parallel state ($R_p$) | 13.33 ohms |
| Piezoelectric film resistance in parallel with the bleeder resistance $\left( R_{piezo} \parallel R_b \right)$ | 25.4 ohms |
| Elliptical soft layer's major axis ($a_1$) | 800 nm |
| Elliptical soft layer's minor axis ($a_2$) | 700 nm |
| Elliptical soft layer's thickness ($a_3$) | 2.2 nm |
| Supply voltage ($V_s$) | 12 V |
| Gilbert damping constant ($\alpha$) | 0.01 |
| Spin polarization in the current ($\eta$) | 0.3 |
| Piezoelectric film thickness ($d$) | 1 μm |
| Young's modulus of soft layer ($Y$) | 80 GPa |
| Piezoelectric coefficient ($d_{31}$) | 300 pm/V |
| Dipole coupling field ($H_d$) | 7957 A/m (10 mT) |

## 6.3 Results and Discussion

The stochastic simulation of the magnetodynamics of the soft layer (Equation (8)) is carried

assuming that the supply voltage $V_s$ is turned on at time $t = 0$. The initial orientation of the

magnetization at $t = 0$ is close to the –y-direction because of dipole coupling with the hard layer

whose magnetization is in the +y-direction. We therefore take the initial values of the soft layer's

magnetization components as $m_x(t=0)=0.045, m_y(t=0)=-0.999, m_z(t=0)=0.001$. The initial

point was not at $m_y(t=0)=-1$ since that is a stagnation point where the torque on the magnetization

due to the spin polarized current, shape anisotropy, strain and dipole coupling, vanishes. The

thermal noise field can dislodge the magnetization from the stagnation point. At 0 K, there is no

thermal noise and hence the magnetization would have been stuck at –y-axis had we used the initial

condition $m_y(t=0)=-1$. In Fig. 6.2, it is shown that the temporal variations of the magnetization

components $m_x(t), m_y(t), m_z(t)$ at 0 K temperature when there is no thermal noise and the dipole

coupling field strength $H_d$ is 7957 A/m (10 mT). This figure shows that the magnetization oscillates

by nearly the full $180^0$ (between the parallel and anti-parallel configurations) since $m_y(t)$ varies

between -0.9394 and 0.9009. Note also that as expected, the magnetization lifts out of the soft

layer's plane during the oscillation since $m_z(t)$ varies between -0.52 and 0.52.
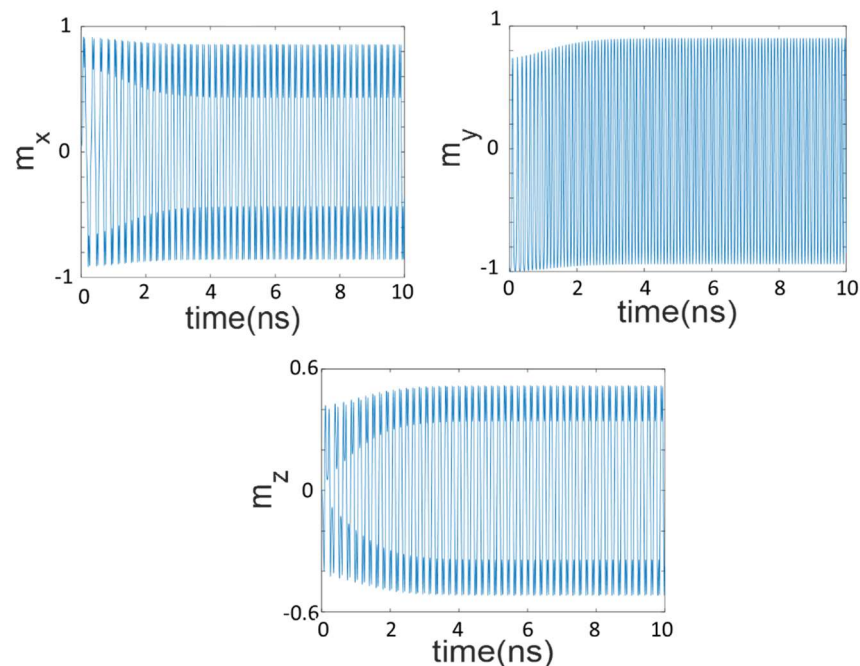


Fig. 6.2: Temporal variations of the magnetization components in the soft layer at 0 K temperature. Note that it takes almost 3 ns to reach steady state amplitude.

In Fig. 6.3(a), it is shown how $R_{MTJ}$ varies with time at 0 K. Note that the maximum and minimum values of $R_{MTJ}$ do not vary by a factor of 6 (despite the assumed TMR of 500%) since the magnetization of the soft layer never reaches either the full antiparallel direction or the full parallel direction during its swing ($m_y(t)$ varies between -0.9394and 0.9009). The maximum and minimum values of the s-MTJ resistance differ by a factor of ~4.7, instead of 6.
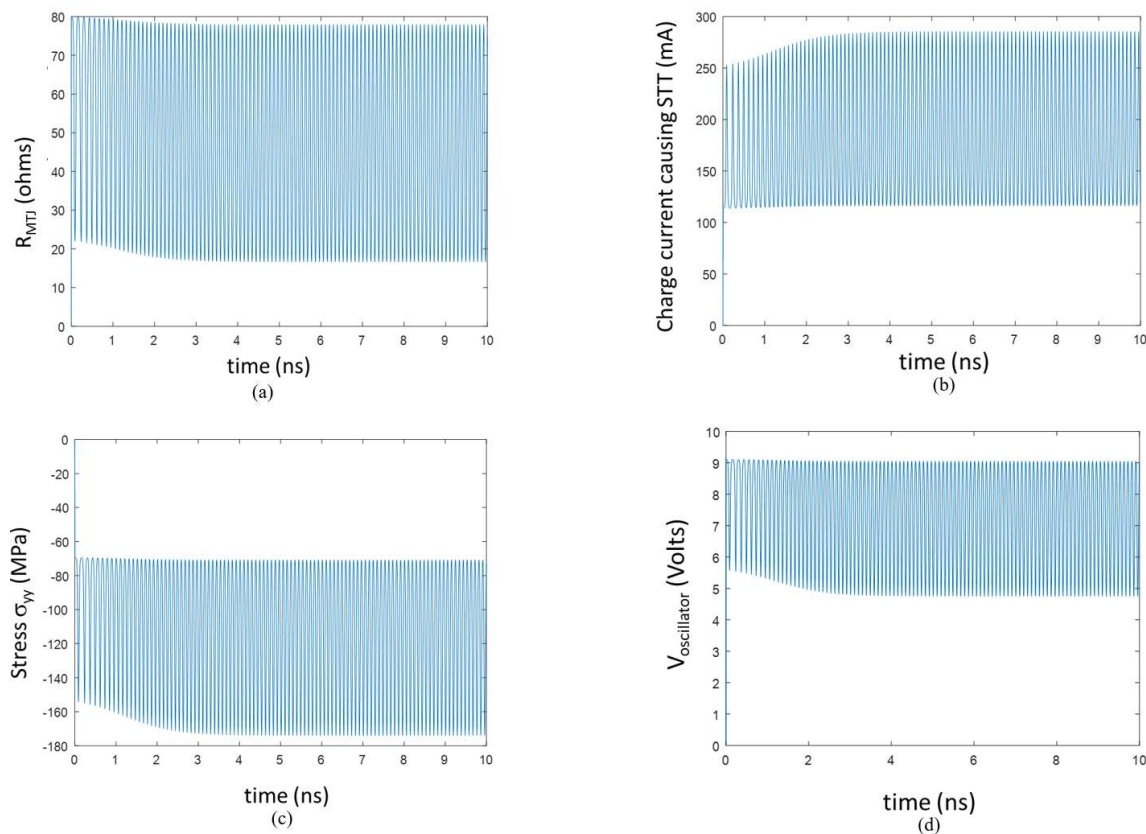


Fig. 6.3: (a) Variation of the resistance of the s-MTJ with time at 0 K temperature, (b) Variation of the current through the s-MTJ with time at 0 K. This current delivers the spin transfer torque, (c) Variation of the uniaxial stress in the soft layer as a function of time at 0 K, (d) Variation of the voltage across the s-MTJ (the oscillator output voltage) as a function of time at 0 K. There is a dc offset of ~7.4 V, while the oscillatory peak-to-peak amplitude is slightly over 4.3 V. It takes about 3 ns to reach steady-state amplitude for all the oscillatory signals.

In Fig. 6.3(b), it is shown how the charge current flowing through the MTJ varies with time. The peak current density is $6.5 \times 10^{11}$ A/m$^2$ which is high, but not completely unreasonable since current densities of this order have been used in MTJs [102][106][107]. Reducing it would have required

reducing the power supply voltage $V_s$. Unfortunately, a lower power supply voltage is not able to sustain the oscillations. Moreover, in the presence of noise at room temperature, random fluctuations in the thermally averaged oscillation amplitude show up if the power supply voltage is lower than a minimum threshold value. The threshold voltage is determined by the complex interaction between the shape anisotropy, strain anisotropy, STT and dipole coupling field. For the parameters that we chose for the s-MTJ, the threshold voltage is 12 V, which results in the current density is $6.5 \times 10^{11}$ A/m$^2$. Any lower current density will not sustain the oscillations or be able to counter the effect of room temperature thermal noise.

One likely approach to reduce the threshold current density is to increase the area of the s-MTJ while keeping the soft layer's volume constant. This does decrease the threshold current density somewhat, but not in inverse proportion to the area. We chose the s-MTJ surface area $\left[ (\pi/4) \times 700\,\mathrm{nm} \times 800\,\mathrm{nm} \right]$ such that it remains sub-micron in lateral dimensions, but not so small as to make the threshold current density too high. Micron scale MTJs have been fabricated by many groups [35][108]. In Fig. 6.3(c), it is shown how the uniaxial stress $\sigma_{yy}(t)$ along the major axis of the soft layer varies with time – all at 0 K when there is no thermal noise. Note that the maximum compressive stress generated in the soft layer is about 175 MPa. Since the Young's modulus of Terfenol D is 80 GPa, the maximum strain generated in the soft layer is 0.2%. There are reports of 0.6% strain generation in piezoelectric materials [109]; hence, this value is reasonable. Finally, in Fig. 6.3(d), it is shown how the oscillator output voltage $V_{\mathrm{oscillator}}(t)$ varies with time at 0 K.

In Fig. 6.4, the "average" $V_{\mathrm{oscillator}}(t)$ as a function of time at 300 K in the presence of thermal noise is shown. The averaging is carried out over 1000 trajectories (simulation results) shown in Fig. 6.5, each trajectory is slightly different from the other owing to random thermal noise. Note from Fig. 6.4 that thermal noise does not inhibit the oscillator operation, but introduces a very

slight fluctuation in the amplitude. To understand the origin of this fluctuation, we have plotted the oscillations of the 1000 different trajectories in Fig. 6.5. Note that the different trajectories are slightly phase-shifted from each other, which is what leads to the smearing. Hence, averaging over them causes a slight random fluctuation in the amplitude of the oscillation seen in Fig. 6.4. The fluctuation is however less than 5% of the amplitude and hence not inhibitory. Note that in all cases, it takes about 3 ns to reach steady-state amplitude. This is the time taken by the complex interaction between shape anisotropy, stress anisotropy, dipole field and spin transfer torque to reach steady state.
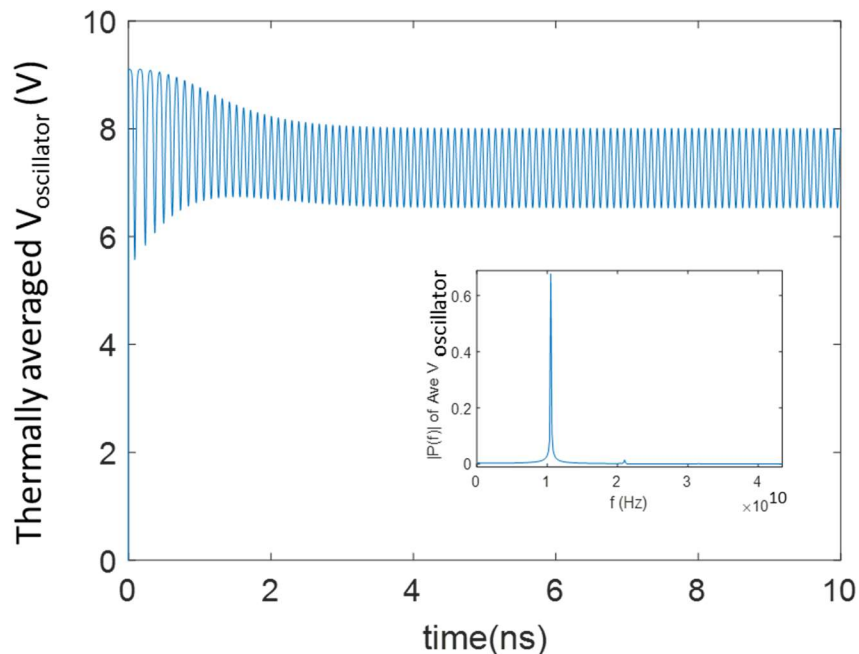


Fig. 6.4: Thermally averaged variation in the oscillator voltage as a function of time at 300 K in the presence of thermal noise. This plot has been obtained by averaging 1000 trajectories (results of simulations) which are all slightly different from each other because of the randomness of the noise field. It again takes about 3 ns to reach steady state amplitude. The steady state period is ~100 ps (frequency = 10.52 GHz, wavelength = 3 mm). The dc offset is still about 7.3 V and the steady state peak-to-peak amplitude is 1.5 V. The inset shows the Fourier spectra of the oscillations after suppressing the dc component. The fundamental frequency is 10.52 GHz and there is a second harmonic at ~21 GHz whose amplitude is ~60 times less than that of the fundamental. Surprisingly the output is spectrally pure and this is almost a monochromatic (ideal) oscillator. The resonant frequency is 10.52 GHz and the bandwidth (full width at half maximum) is ~200 MHz, leading to a quality factor of 52.6.
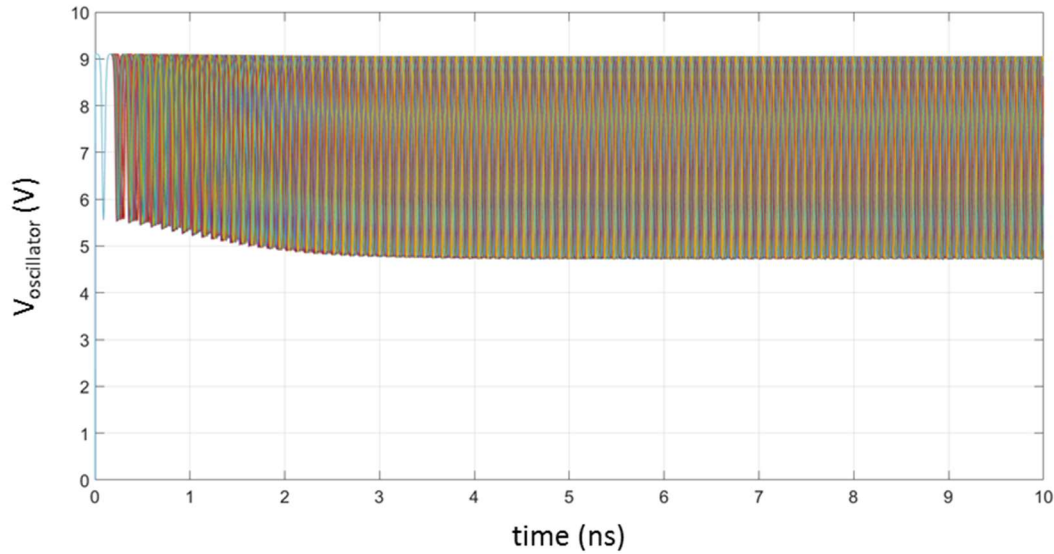
Fig. 6.5: Oscillator voltage as a function of time at 300 K. Here, 1000 different trajectories have been plotted and clearly there is some spread among the trajectories because of thermal noise. The plot in Fig. 6.4 was obtained by averaging over these trajectories.

It is that the oscillator operation is sensitive to the choice of various parameters such as the supply voltage $V_s$, the dipole coupling field $H_d$, $R_{piezo} \parallel R_b$ and $R_p$. There are certain "windows" for these quantities where the oscillations show up. Outside these windows, the oscillations are suppressed. This is not surprising. The phenomenon underlying the operation of this device depends on a delicate balance between the magnetodynamics due to STT current, dipole coupling field, shape anisotropy (demagnetizing) field and strain, and the complex *interaction* between them. The STT current tries to align the magnetization along the soft layer's major axis in the direction of the hard layer's magnetization, the strain tries to align the magnetization perpendicular to the major axis, while the dipole coupling field tries to align the magnetization along the major axis anti-parallel to the direction of the hard layer's magnetization. Thus, the three different agents attempt to align the magnetization along three different directions and it is the complex interaction between these agents that cause the magnetization direction to oscillate in time. Clearly, too high a stress will pin

the magnetization permanently along the minor axis, too high STT will pin the magnetization parallel to the hard layer's magnetization and too high dipole coupling will pin the magnetization anti-parallel to the hard layer's magnetization. Only the right balance between these agents will make the magnetization oscillate. Because of the need for this delicate balance, the oscillator operation is sensitive to the choice of device parameters. The sensitivity is not a serious impediment since the device parameters like the dipole coupling field and the power supply voltage can be easily tuned and hence calibrated. The dipole field acts as a constant field along the major axis of the soft layer and is directed opposite to the magnetization of the hard layer. Therefore, this field can be easily tuned with an external in-plane magnetic field directed along the major axis of the soft layer. Similarly, the power supply voltage can also be tuned and calibrated. The dipole coupling field strength is given by

$$H_d = \xi \frac{M_s \Omega}{4\pi r^3}, \qquad (10)$$

where $r$ is the center-to-center separation between the hard and soft layers along the z-axis and $\xi$ is a suppression factor $(0 \leq \xi \leq 1)$ due to the use of a synthetic antiferromagnet for the hard layer, which suppresses dipole interaction. We assume that the spacer layer of the MTJ is 2 nm thick and the hard layer is 10 nm thick (because it consists of multiple layers), which would make $r = 8.1$ nm. Using the values in Table 6.1 for $M_s$ and $\Omega$, we find that for $H_d$ to be 7957 A/m (10 mT), $\xi \approx 4.3 \times 10^{-6}$. Again, there is no criticality associated with the value of $\xi$ since the dipole coupling field can be tuned by an in-plane magnetic field directed along the major axis of the elliptical soft layer.

The power dissipated in the oscillator is mostly static (dc) power and is ~ 182 mA $\times$ 12 V = 2.18 W. The rms ac power output is ~ 30 mW. A single oscillator device that outputs 30 mW at microwave frequency is quite attractive.

## 6.4 Conclusion

In conclusion, here it is shown that a single straintronic magneto-tunneling junction (with a passive resistor) can implement a microwave oscillator with excellent quality factor which would have taken multiple electronic components to implement in traditional electronics. In particular, one would have needed microwave components which are expensive. Thus, the magnetic implementation has several advantages, such as lower cost and reduced device footprint. The operation is sensitive to the choice of the supply voltage and the dipolar coupling field for any given MTJ specification, but these quantities can be easily tuned with external agents to calibrate a prototype for optimal operation.

# Chapter 7: Magnetic Hardware to Generate Random Bit Streams with Tunable Correlation for Probabilistic Computing

There is significant interest in generating two or more bit streams with tunable amount of correlation between them for stochastic computing arithmetic circuits, graphical circuit models, computer vision and image processing applications [110-113]. They are normally produced with *software* (which is slow and consumes excessive processor and memory resources) or with complex *hardware* that involves shift registers, Boolean logic gates, random number generators, multiplexers, binary counters, comparators, etc. [113]. These hardware platforms consume large footprints on a chip, dissipate enormous amounts of energy and are expensive. In this chapter, it is discussed how two-bit streams with *controlled amount of correlation* can be generated with two magneto-tunneling junctions whose soft layers are dipole-coupled and one of them is magneto-elastically coupled to an underlying piezoelectric substrate.

## 7.1 Working Principle

Fig. 7.1 shows the system to generate two-bit streams with controlled amount of correlation. It consists of two magneto-tunneling junctions (MTJs) of elliptical cross-section whose major and minor axes are mutually parallel. They are fabricated on a poled piezoelectric film deposited on a conducting substrate. Two electrodes are delineated on the piezoelectric film (flanking the soft layer of MTJ B) with appropriate dimensions and spacing to generate biaxial strain underneath the magnetostrictive soft layer of MTJ B when a voltage is applied between the electrodes and the bottom conducting substrate [23][24]. By varying the voltage, we can vary the magnitude of the strain experienced by the magnetostrictive soft layer of MTJ B. The soft layer of MTJ A will also experience some strain when MTJ B is strained, but its magnetization will be determined by a current pulse injected into it, which will override any strain effect. The spacing between the MTJs is made sufficiently small to have significant dipole coupling between the two soft layers. The two

binary bits (Bit A and Bit B) are encoded in the resistance states of the two MTJs – high resistance is bit 1 and low resistance bit 0.
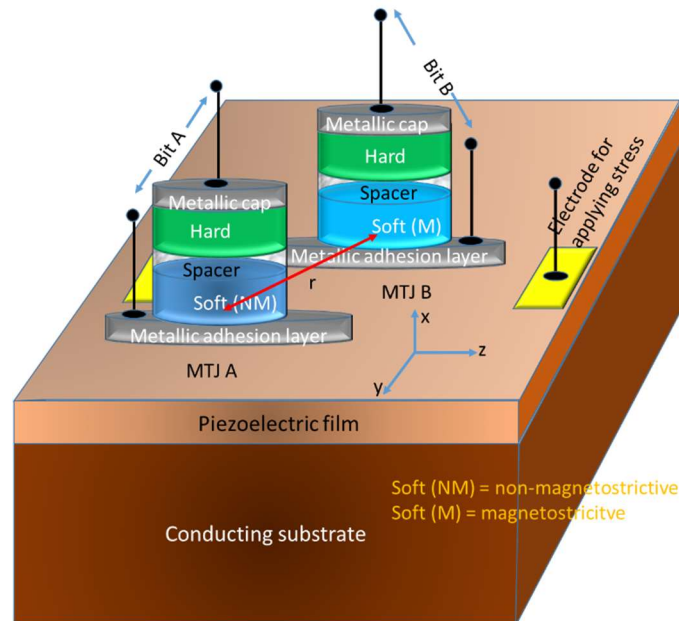


Fig. 7.1: A magneto-elastic system for generating two random bits with controlled amount of correlation.

To generate a random Bit A, a voltage (or current) pulse of random polarity to MTJ A is applied. Depending on the polarity of the pulse, a spin polarized current will flow through the soft layer of MTJ A which will either turn the magnetization of the soft layer of MTJ A parallel to the direction of the magnetization of its hard layer (Bit A = 0), or antiparallel (Bit A = 1). Thus, random Bit A can be generated with a voltage or current pulse of random polarity. To generate the random Bit B that is *controllably correlated* with Bit A, it is not required to apply any voltage pulse to MTJ B. Instead, the dipole coupling between the soft layers of MTJ A and MTJ B is used to set the value of the Bit B, depending on the value of Bit A. One would expect that dipole coupling would always make the magnetization of the soft layer of MTJ B become antiparallel to the magnetization of the soft layer of MTJ A, resulting in perfect (anti-) correlation between bits A and B, but this

does not happen. There is a shape anisotropy energy barrier within the soft layer of MTJ B, which will *have to be overcome* by dipole coupling to make its magnetization rotate from its initial orientation (if it was not initially antiparallel) to become antiparallel to that of the soft layer of MTJ A. If the energy barrier cannot be overcome, then bit B will remain in its previous state and not be anti-correlated with bit A which is elucidated in Fig. 7.2.
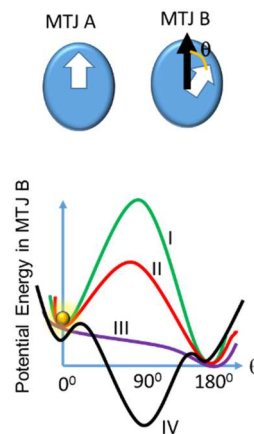


Fig.7.2: Potential energy as a function of magnetization orientation within the soft layer of MTJ B in the presence of dipole coupling with MTJ A whose magnetization is oriented as shown in the top panel. The potential profile is asymmetric because of the dipole coupling. (I) No stress applied, (II) sub-critical stress applied, (III) critical stress applied, and (IV) super-critical stress applied. The ball indicates the initial magnetization state.

Suppose the magnetization of the soft layer of MTJ B was initially at $\theta = 0^0$ (see Fig. 7.2 for the definition of $\theta$) and the magnetization of MTJ A became oriented along $\theta = 0^0$ by the current pulse. This places the two soft layers in the parallel configuration. The potential energy profile in the soft layer of MTJ B as a function of its magnetization orientation will look like curve I in the lower panel in Fig. 2. The system will be stuck in the metastable state (local energy minimum) at $\theta = 0^0$ (keeping MTJ A and MTJ B parallel) and not be able to transition to the global energy minimum at $\theta = 180^0$ (where MTJ A and MTJ B will be mutually anti-parallel) because of the intervening potential energy barrier. In this case, bit B will not be able to respond to bit A and the two bits will be *uncorrelated*. However, if varying degree of stress is applied, then the energy barrier will be

depressed by varying degree and thus be able to tune the probability that the system can transition to the ground state at $\theta = 180^0$ where the two MTJs will be anti-parallel and hence anti-correlated. Thus, by varying the voltage applied to the two electrodes in Fig. 7.1, which varies the stress produced in the soft layer of MTJ B, *the correlation between bits A and B* can be varied from no correlation to perfect (anti-) correlation. From Fig. 7.2, it is observed that stress affects the energy barrier in different ways. Looking at the potential profiles, one would understand that if the initial magnetization state in MTJ B is parallel to the magnetization of MTJ A, which means that the initial state is at $\theta = 0^0$ as shown by the ball in Fig. 7.2, then the maximum likelihood that the magnetization of MTJ B will flip in response to the magnetization state of MTJ A (i.e. the ball will roll down to $\theta = 180^0$) will occur when the applied stress is the *critical stress*. Thus, the correlation between bits A and B will exhibit a *non-monotonic behavior as a function of stress*. The two bits will be maximally anti-correlated under critical stress and the anti-correlation will drop off as we apply either sub-critical or super-critical stress.

## 7.2 Simulation using MATLAB

The magneto-dynamics within the soft layers of both MTJ A and MTJ B are simulated in the presence of thermal noise by solving *coupled* stochastic Landau-Lifshitz-Gilbert (s-LLG) equations which is the same as shown in chapter 6 and so the details are not mentioned here anymore. The soft layers are made of Terfenol-D [114][115] nanomagnets and have dimensions of major axis = 100 nm, minor axis = 90 nm and thickness = 15 nm. The shape anisotropy energy barrier within the nanomagnet is 378 kT at room temperature. The *correlation parameter* is defined as:

$$C = \langle A \times B \rangle \tag{1}$$

where *A* is the value of bit A (either +1 or -1) and *B* is the value of bit B (also either +1 or -1). We use -1 instead of 0 to represent the logic complement of the binary bit 1. The angular brackets denote ensemble average. The ensemble averaging is carried out over 1000 switching trajectories generated in our simulator. The switching trajectories are generated in the following manner.

For MTJ A, we assume that the magnetization of its soft layer is initially pointing in the +z-direction. We then pass a spin polarized current, with spin polarization in the –z-direction and magnitude varying between 30 and 40 mA (above the critical current for switching) and simulate the magneto-dynamics of the soft layer of MTJ A which yields its magnetization as a function of time $m_A(t)$ At the same time, we simulate the magneto-dynamics in the soft layer of MTJ B which depends on dipole coupling and hence on $m_A(t)$. This determines the magnetization $m_B(t)$ in MTJ B, which in turn, influences the magnetization in MTJ A through dipole coupling. Thus, the coupled s-LLG equations are solved. The simulations are carried out until the magnetizations of both soft layers reach steady state, at which point they are either approximately parallel or antiparallel. If they are parallel, then $A \times B = +1$, whereas if they are antiparallel, then $A \times B = -1$. The value of $A \times B$ is averaged over the 1000 trials to calculate the correlation parameter defined in Equation (2). A value of C = 1 indicates no correlation, a value of C = -1 indicates perfect anti-correlation, and intermediate values indicate partial correlation.

### 7.3 Results and Discussion

In Fig. 7.3, the plots of the correlation function as a function of the stress for different spin polarized currents delivering spin transfer torque (STT) in the soft layer of MJTJ A (no current is injected into MTJ B) and for four different center-to-center separations between the soft layers of MTJ A and MTJ B are shown. There are several features of interest. First and foremost, we can

vary the correlation parameter from +1 (no correlation) to -1 (perfect correlation) continuously by varying the stress applied with the voltage impressed between the shorted electrodes in Fig. 7.1 and the conducting substrate. Thus, we can control the correlation with an external voltage. That allows for perfect tunability of the correlation.
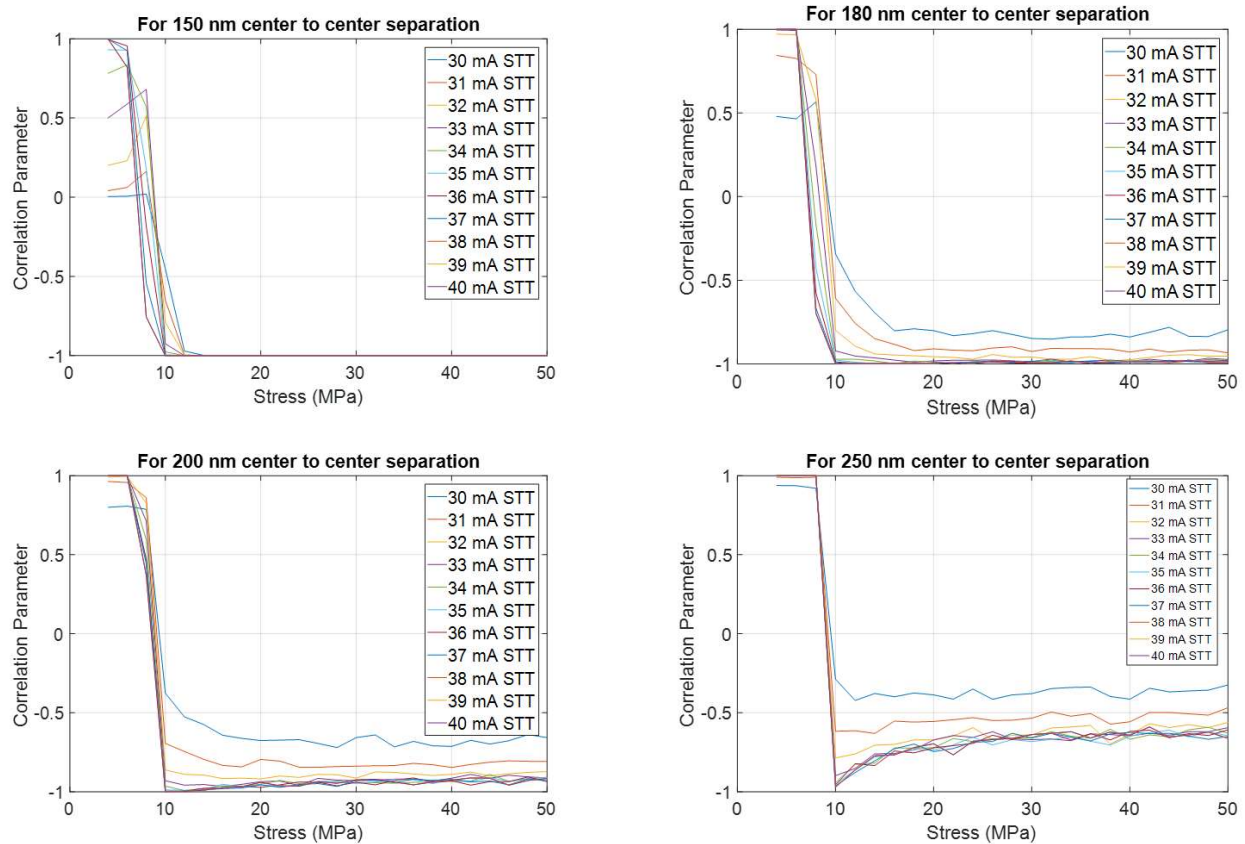


Fig. 7.3: Correlation parameter as a function of stress for different spin polarized currents and for four different spatial separations between MTJ A and MTJ

There are also other interesting features. The anti-correlation decreases with increasing separation between the MTJs (i.e. decreasing dipole coupling strength), which is obvious since the anti-correlation is caused by dipole coupling. There is also a clear dependence on the STT current injected into MTJ A. A low current may not succeed in "writing" the state of Bit A reliably and a manifestation of that is the failure to reach perfect anti-correlation at high stress values when the

STT current is low. This feature becomes increasingly prominent with increasing separation between the MTJs (decreasing dipole coupling strength). The current densities used here are high ($\sim 5 \times 10^{12}$ A/m$^2$), but this is a consequence of the materials and geometry chosen. Engineering the current densities to lower values is possible, but not an objective of this work. Another very interesting feature clearly observed at higher inter-MTJ separations (bottom panels in Fig. 7.3) is that the anti-correlation becomes maximum at a certain stress value (note the non-monotonic behavior). This is the "critical stress" discussed earlier and it is clearly visible in these cases.

## 7.4 Conclusion

In this chapter, it is shown how to generate two bit streams, one of which is random and the other controllably correlated with the first. These bit streams have applications in various areas of stochastic computing. While their traditional electronic implementation would require several components, here we have shown how they can be realized with two dipole coupled magneto-tunneling junctions with magnetostrictive soft layers, fabricated on a piezoelectric substrate. The correlation can be tuned continuously between no correlation and perfect anti-correlation with an external voltage, which is convenient.

**Chapter 8: Experimental Demonstration of Hybrid magneto-dynamical modes in a single magnetostrictive nanomagnet on a piezoelectric substrate**

The intrinsic dynamics of a single nanomagnet [60][116] have attracted significant attention owing to their fundamental importance and their role in determining the spatio-temporal limits of precessional switching. In this chapter, the study of ultrafast magnetization dynamics in a single magnetostrictive nanomagnet fabricated on a piezoelectric substrate, performed using time-resolved magneto-optical Kerr effect (TR-MOKE) measurements is reported. Usual TR-MOKE measurement [54][68] utilizes a femtosecond laser pump beam, or a pulsed magnetic field generated by a photoconductive switch triggered by a femtosecond laser, to excite the magnetization of a magnet to precess about a bias magnetic field. A probe beam then periodically samples the magnet's reflectivity and the polarization (Kerr Signal) of the reflected light as a function of the delay between the pump and the probe to investigate the ultrafast magnetization dynamics. The linear magneto-optical Kerr rotation is proportional to the sample magnetization. This can also provide information about the time varying polarization of the substrate. Thus, by measuring Kerr rotation as a function of time, magnetization dynamics over different time-scales are observed. The time-varying reflectivity can provide information about charge and phonon dynamics. The simple picture changes when the pump beam causes additional excitations in the magnetization state. Consider the case when the magnet is deposited on a poled piezoelectric substrate. The electric field in the pulsed pump beam generates time-varying surface charges in the substrate, which will generate an alternating electric field. Since PMN-PT is piezoelectric, this field, in turn, will generate periodic (compressive and tensile) strain in the substrate from $d_{33}$ and/or $d_{31}$ coupling. Additional periodic strain can be generated from the differential thermal expansions of the magnet and the substrate due to periodic heating by the pulsed pump beam. These strains will generate surface acoustic waves (SAWs) in the substrate [39][117-120] which will periodically expand and contract the magnet. If the magnet is magnetostrictive, then this will

periodically change its magnetization owing to the Villari effect [120][121]. The complex interaction of the two magneto-dynamics - precessional and SAW-induced - gives rise to multiple hybrid oscillation modes (each with its own frequency) in the out-of-plane component of the magnet's magnetization, which then induce corresponding oscillations in the magnet's reflectivity and polarization of the reflected light (Kerr signal). They are the object of this study.

The current study was aimed at understanding ultrafast (~100 ps time scale) magneto-dynamics in the presence of both SAW-induced magnetization rotation and precession around an external magnetic field. This study revealed a rich plethora of hybrid magneto-dynamical modes that arise from the dynamical mixing of the SAW (periodic strain) induced magnetization evolution and precessional motion. It is found that the spin waves in the nanomagnet associated with these modes exhibit complex power and phase profiles.

## 8.1 Fabrication and Characterization of Nanomagnets

To investigate the hybrid modes experimentally, an array of slightly elliptical (eccentricity $\approx 1$) Co nanomagnets (magnetostriction $\lambda_s$ = 40-60 ppm) are fabricated on a piezoelectric (001) PMN-PT substrate ($d_{33}$>2000 pC/N) using electron-beam lithography and electron beam evaporation of Co, followed by lift-off. Two different electron-beam resists of different molecular weights were used to facilitate lift off. Prior to fabrication, the PMN-PT substrate was poled with a high electric field in the direction of the major axes of the elliptical nanomagnets. The thickness of the nanomagnets is nominally 15 nm. Figures 8.1(a) and (b) show a scanning electron micrograph (SEM) of the nanomagnets and their magnetic force microscope (MFM) images. The nanomagnets are almost circular with major axis of 190 nm and minor axis of 186 nm. Because of this small aspect ratio, they do not show good phase contrast in the MFM images or single domain behavior, but because their shape anisotropy is small, the magnetic anisotropy is dominated by strain

anisotropy in the presence of the SAWs. The spacing between neighboring nanomagnets (~1 µm) is large enough for the dipole interaction between them to be negligible, which means that isolated single nanomagnets are probed.
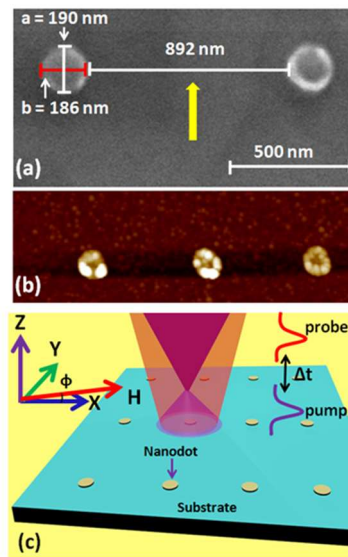


Fig. 8.1: (a) Scanning electron micrograph of the Co nanomagnets deposited on a PMN-PT substrate. The edge-to-edge separation between two neighboring nanomagnets in a row [along the line collinear with their minor axis (x-direction)] is about 892 nm, which shows that the pitch of the array is about 1 µm. The separation between two adjacent rows is ~4 µm along the y-direction. Major and minor axes are denoted as *a* (≈ 190 nm) and *b* (≈ 186 nm), respectively. The yellow arrow indicates the poling direction of the substrate. (b) Magnetic force micrograph of the nanomagnets which do not show good phase contrast because of insufficient shape anisotropy. (c) The experimental geometry is shown with the bias magnetic field (*H*) applied along the array in the direction of the nanomagnets' minor axes (x-direction) with a slight out-of-plane tilt (ϕ) of few degrees.

## 8.2 Proof of the Presence of SAW

To ascertain that the pump beam indeed generates SAWs in the PMN-PT substrate, we first measured the polarization and intensity of light reflected from the bare PMN-PT substrate as a function of the delay between the pump and the probe by focusing both pump and probe beams on to the bare substrate. Clear oscillations are observed in both polarization and intensity of the light

reflected from the bare substrate and they can only originate from the SAWs. In Fig. 8.2(a), we show the intensity (reflectivity) oscillation for 15 mJ/cm$^2$ pump fluence, whereas the oscillation in the polarization (Kerr signal) is shown in Fig. 8.2(b). As expected, there are multiple oscillation modes in both reflectivity and polarization, each with a different frequency, because of the excitation of SAWs with multiple frequencies. Their frequencies at any given fluence were found to be independent of the bias magnetic field, showing that these oscillations are not of magnetic origin. They arise from the SAWs which cause periodic atomic displacements on the substrate's surface thereby changing the surface charge polarization periodically (PMN-PT is a polar material) and giving rise to polar phonons.

The fast Fourier transformation (FFT) of these oscillations reveals the dominance of two peaks (2 GHz and 8 GHz) in the spectra (see Fig. 8.2(a)), which are the two dominant SAW frequencies excited in the PMN-PT substrate by the pulsed pump beam. There is also a small peak in the spectrum at ~16 GHz, which we ignore (it may be a second harmonic of the 8 GHz oscillation). The SAW wavelength $\lambda$ associated with the 2 GHz frequency is ascertained from the relation $v = \lambda f$ where $v$ is the phase velocity of the SAW and $f$ is the frequency. The phase velocity of SAW in a (001) PMN-PT crystal depends on the propagation direction, but it is on the order of 2000 m/sec [122]. The 2 GHz mode therefore corresponds to a wavelength of roughly 1 μm, which happens to be the pitch of the array. It therefore appears that this mode is a resonant mode determined by the geometry of the array, as in refs. [117-119]. The 8 GHz mode cannot be related to any obvious geometric feature of the nanomagnet array and may be intrinsic to the substrate.
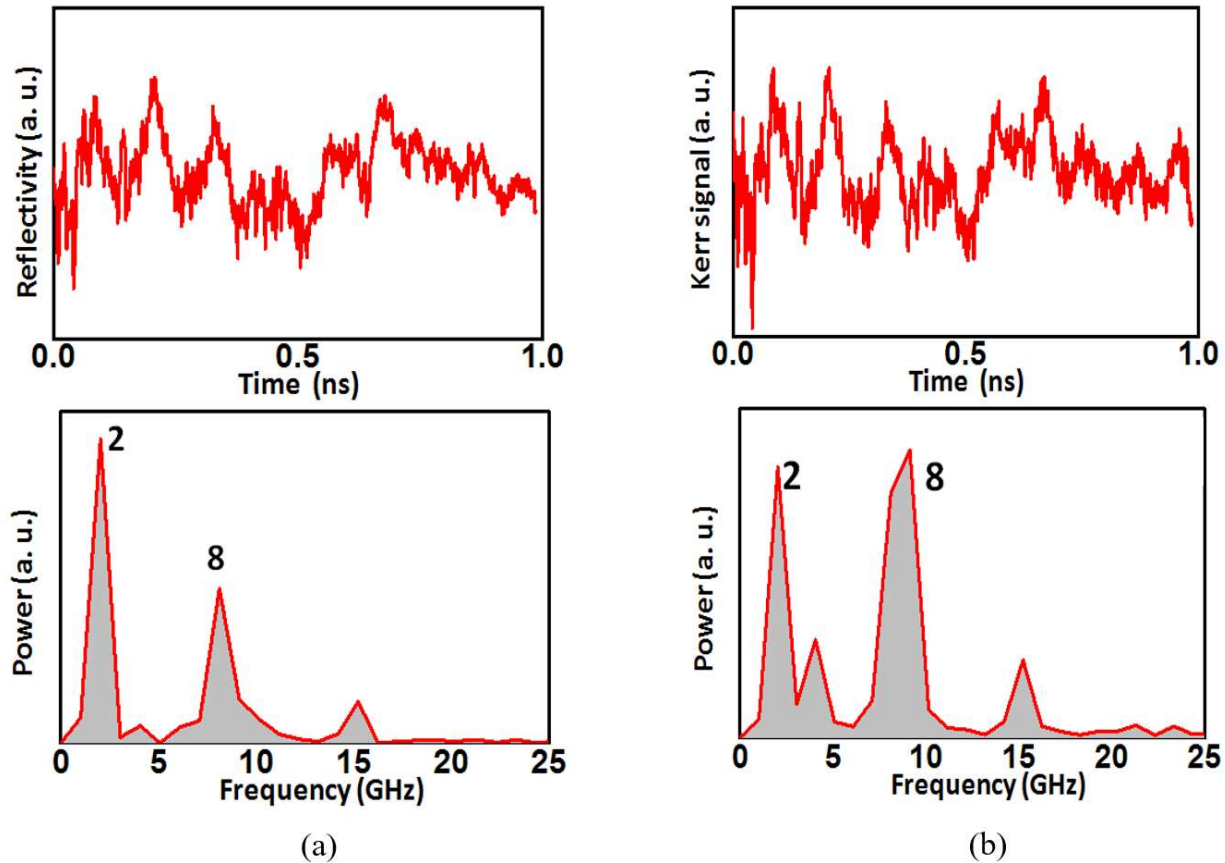
Fig. 8.2: (a) Background subtracted time-resolved data for reflectivity of the bare PMN-PT substrate as a function of the delay between the pump and the probe, obtained at 15 mJ/cm$^2$ pump fluence. Also shown are the fast Fourier transforms of the oscillations. Frequencies of the two most intense peaks are indicated in GHz. (b) Back ground subtracted time resolved data Fourier transform (or frequency spectra) of the oscillations in the polarization (Kerr Signal) of light reflected from the bare PMN-PT substrate.

## 8.3 Hybrid Spin Wave Modes

Next the out-of-plane magnetization dynamics (temporal variation in the spatially averaged out-of-plane component of the magnetization) of a single Co nanomagnet on the PMN-PT substrate is probed in the presence of both a bias magnetic field and SAWs by focusing the pump and probe beams on a *single* nanomagnet and measuring the Kerr oscillations as well as oscillations in the reflectivity. In Figs. 8.3 (a) and (b), we show the background-subtracted time-resolved Kerr oscillations in time as a function of bias magnetic field along with their Fourier transforms. The

pump fluence was 15 mJ/cm$^2$. The reflectivity oscillations and their Fourier transforms are ignored as we are particularly interested on Kerr signal and the corresponding magnetization dynamics.
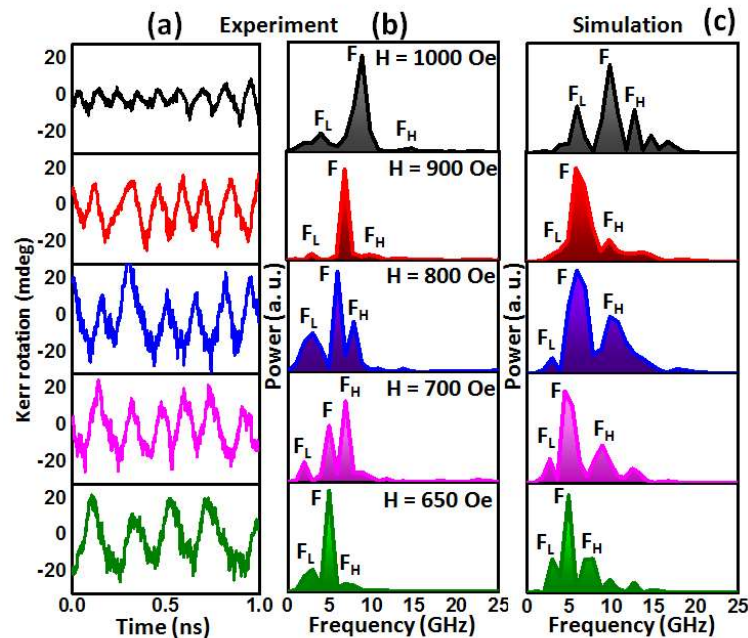


Fig. 8.3: Bias magnetic field dependence of the (background-subtracted) time-resolved Kerr oscillations from a single Co nanomagnet on a PMN-PT substrate. The pump fluence is 15 mJ/cm$^2$. (a) The measured Kerr oscillations in time and (b) the fast Fourier transforms of the oscillations. The Fourier transform peaks shift to lower frequencies with decreasing bias magnetic field strength. There are multiple oscillation modes of various Fourier amplitudes. Out of those, the dominant mode (at all bias fields except 700 Oe) is denoted by F and its nearest modes $F_H$ and $F_L$. (c) Fourier transforms of the temporal evolution of the out-of-plane magnetization component at various bias magnetic fields simulated with MuMax3 where the amplitude of the periodically varying strain anisotropy energy density $K_0$ is assumed to be 22,500 J/m$^3$. The simulation has additional (weak) higher frequency peaks not observed in the experiment. The spectra in the two right panels are used to compare simulation with experiment.

Multiple modes (corresponding to peaks in the Fourier spectra) are observed in Kerr oscillations at all bias magnetic fields used, with all peaks shifting to lower frequencies with decreasing bias field. This magnetic field dependence shows that these modes have a magnetic component mixed in. The most intense peak (at all bias fields except 700 Oe) is denoted as 'F' in Fig. 8.3(b). Two other prominent peaks that appear at higher and lower frequencies with respect to F are indicated

as 'F$_H$' and 'F$_L$', respectively. All modes associated with these three peaks in the Fourier spectra are hybrid magneto-dynamical modes arising from the interaction between the magnetic (precession of the magnetization about the bias magnetic field) and the non-magnetic (periodic change in the magnetization due to the periodic strain generated by the SAWs) dynamics. The former dynamics depends on the bias magnetic field while the latter does not.

In order to understand the origin of the modes observed in the Kerr oscillations, the magnetization dynamics in the Co nanomagnet in the presence of the bias magnetic field and the periodic strain due to the SAWs is modelled and simulated using the MuMax3 package [30]. The SAW-induced periodic strain anisotropy in the nanomagnet is included in the simulation by making the oscillating strain anisotropy energy density $K_1(t) = K_0 \left[ \sin\left(2\pi f_1 t\right) + \sin\left(2\pi f_2 t\right) \right]$, where $K_0 = \left(\frac{3}{2}\right)\lambda_s\sigma$ and $f_1$, $f_2$ are the frequencies of the two dominant SAW modes (2 GHz and 8 GHz) observed for the pump fluence of 15 mJ/cm$^2$. Here $\lambda_s$ is the magnetostriction coefficient of the nanomagnet (40 ppm) and $\sigma$ is the maximum stress generated in it by the SAW (stress amplitude). The minor axis of the nanomagnet is in the $x$-direction, the major axis is along the $y$-direction and the $z$-direction is the out-of-plane direction.

At first the micromagnetic distribution within the nanomagnet in the presence of the bias magnetic field applied along the $x$-direction (but with no strain present) from MuMax3 is generated. Then, with this distribution as the initial state, the two-frequency oscillating strain and a small out-of-plane (square-wave) tickle pulse of amplitude 30 Oe, rise time 10 ps, and duration 100 ps are turned to set the magneto-dynamics in motion. The time-varying components of the nanomagnet's magnetization $M_x(x, y, z, t), M_y(x, y, z, t), M_z(x, y, z, t)$ for different bias magnetic fields and different values are obatined. Then the fast Fourier transform of the spatially averaged value of

$M_z(x, y, z, t)$, which we call $\bar{M}_z(t)$, is performed and the spectra obtained from this transform (for different bias magnetic fields) are shown in Fig. 8.3 (c). They are compared with the spectra of the Kerr oscillations found experimentally and shown in Fig. 8.3 (b). This comparison leads us to the best fit value of $K_0 = 22,500$. A reasonably good agreement between the three dominant peaks $F_L$, $F$ and $F_H$ of the simulated Kerr spectra and the experimentally measured Kerr spectra at low fields is observed. The agreement deteriorates slightly at high bias fields, showing that perhaps a single fitting parameter $K_0$ is not adequate to model the entire range of bias fields used in the experiments. From the value $K_0 = 22,500$ J/m$^3$, the effective stress $\sigma$ generated in the nanomagnet is also obtained. Since $K_0 = \left(\frac{3}{2}\right)\lambda_s\sigma$, we find $\sigma = 375$ MPa. The strain amplitude generated in the nanomagnet is found from Hooke's law: $\sigma = Y\varepsilon$, where $Y$ is the Young's modulus of Co (209 GPa) [123] and $\varepsilon$ is the strain amplitude generated by the (polychromatic) SAW. This yields $\varepsilon = 0.18\%$. There are reports of strain $> 0.6\%$ generated in PMN-PT [109]; so, this large value of strain is not unusual. Next the effective electric field that would be required to produce the strain of 0.18% in PMN-PT is calucaled. The reported $d_{33}$ values in PMN-PT are on the order of 2800 pC/N [124]. Hence the effective electric field $E$ in the PMN-PT substrate (calculated from $\varepsilon = d_{33}E$) is $\sim 6.4 \times 10^5$ V/m. The simulated micromagnetic distribution profile in the periodically strained nanomagnet at various times is shown in fig. 8.4.
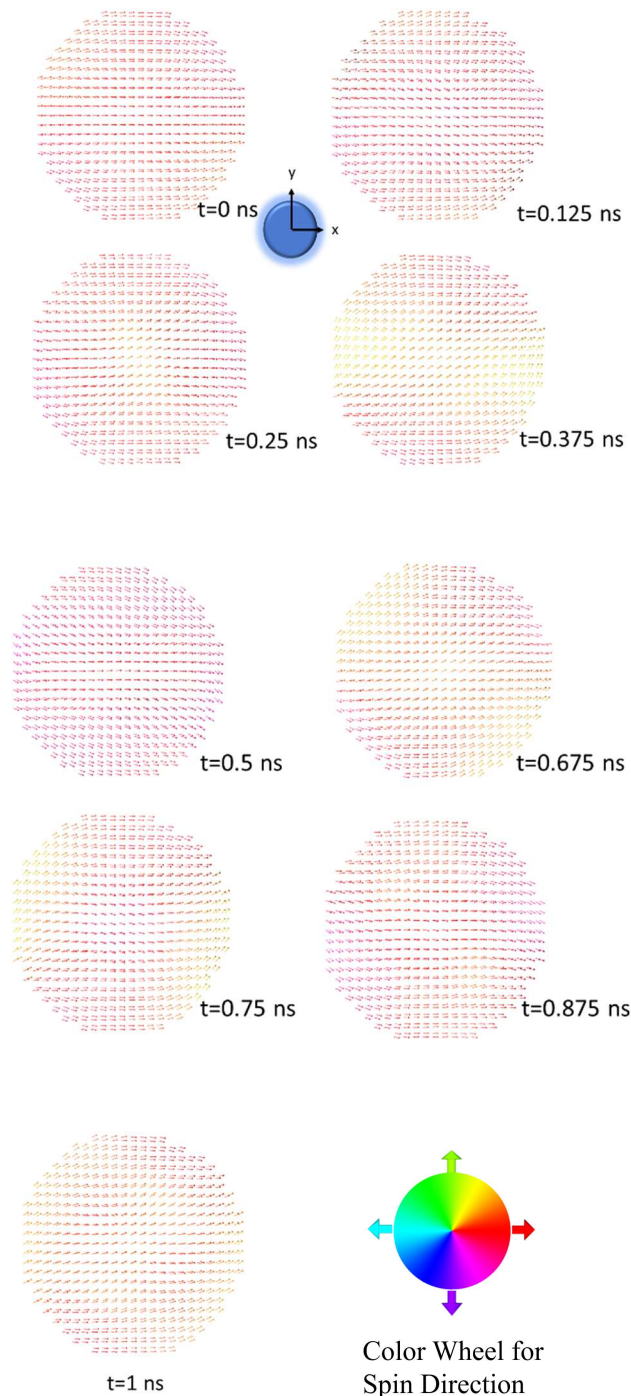
Fig. 8.4: Time-lapsed images of the micromagnetic distributions within the Co nanomagnet for 1ns time period obtained from MuMax3 simulations. Time is counted from the instant the time varying strain anisotropy is turned on. A bias magnetic field of 760 Oe is directed along the minor axis of the ellipse, pointing to the right. The magnetization is initially assumed to be oriented along the bias field and an out-of-plane square wave tickle field of 30 Oe is turned on at time t = 0 for 100 ps to set the magneto-dynamics in motion.

## 8.4 Power and Phase Profiles

To gain more insight into the nature of the hybrid magneto-dynamical modes associated with the three dominant frequencies in the Kerr oscillations, $F_L$, $F$ and $F_H$, the power and phase distributions of the spin waves associated with these modes are calculated and studied theoretically, using *Dotmag* [67]. The MuMax3 simulations are run with a time step of 1 ps and hence provide information about the magnetization of the sample as a function of space (*x, y, z*) every ps. The micromagnetic distributions within the sample at different instants of time (Fig. 8.4) correspond to the superposition of a number of spin wave modes with varying powers and phases. The profiles in Fig. 8.4 do not immediately provide information about the individual resonant modes since the MuMax3 simulations yield only the spatial distribution of magnetization as a function of time: *M (t, x, y, z)*. By fixing one of the spatial co-ordinates of the time-dependent magnetization, a discrete Fourier transform (FFT) of $M\left(x,y,z,t\right)\big|_{z=z_m}$ with respect to time is performed with the Dotmag software. This software plots spatial distribution of the power and phase of the spin waves (in the nanomagnet's plane) at discrete frequencies, and the frequency resolution depends upon the total simulation time. Spatial resolution depends upon the cell size of the system adopted during the MuMax3 simulations. During FFT, the *z-* component of the magnetization is kept fixed to get the *x-y* distribution of the modes inside the dot. This is expressed as

$$\widetilde{M}^{z_m}(f,x,y) = FFT\big[M^{z_m}(t,x,y,z)|_{z=z_m}\big].$$

The power and the phase profiles of resonant modes are calculated following the same procedure as mentioned in chapter 4. At first the unstrained nanomagnet is studied theoretically. In this case, the nanomagnet experiences pure precessional dynamics because of the bias magnetic field and the fast Fourier transform of $\bar{M}_z(t)$ reveals two (bias-dependent) dominant frequencies at any

given bias magnetic field. They can be fitted with the Kittel formula [125]. The power and phase

distributions of the spin wave modes associated with these two frequencies are shown in the Fig.

8.5 for different bias magnetic fields.



Fig. 8.5: (a) Calculated frequency spectrum of the time variation of the spatially-averaged out-of-plane magnetization component $\bar{M}_z(t)$ in an *unstrained* elliptical Co nanomagnet in the presence of a bias magnetic field of 1000 Oe directed along the ellipse's minor axis. The quantity $\bar{M}_z(t)$ is calculated from MuMax3. (b) Calculated spin-wave mode profile in the nanomagnet for the two peak frequencies in the spectrum at different bias fields. These profiles are calculated with the Dotmag code. Since the power is concentrated at the center in one mode and vertical edges at the other, they are a 'center mode' and an 'edge mode' and this nature is independent of the bias field in this range. The units of power and phase in this plot are dB and radians, respectively.

The power distributions of these modes (at the center and vertical edges of the nanomagnet) do

not change much with bias field. The bias field dependence of the precessional frequency reveals

that these two modes have excellent stability. In presence of periodic strain anisotropy due to the

SAWs (with frequencies of 2 and 8 GHz and energy density amplitude $K_0 = 22,500$ J/m$^3$), the

nature of the spin waves associated with the dominant frequencies $F_L$, F and $F_H$ in the Kerr

oscillations are very different compared to the untrained nanomagnet's spin waves. There are three

hybrid magneto-dynamical modes of frequencies $F_L$, F and $F_H$ which display complex spin wave

profiles with their unique characteristics as shown in fig. 8.6. The most intense mode F at 1000 Oe

field contains power throughout the nanomagnet, while the phase profile suggests that spins

precess alternatively in opposite phases giving rise to the azimuthal contrast with azimuthal mode quantization number $n = 5$.
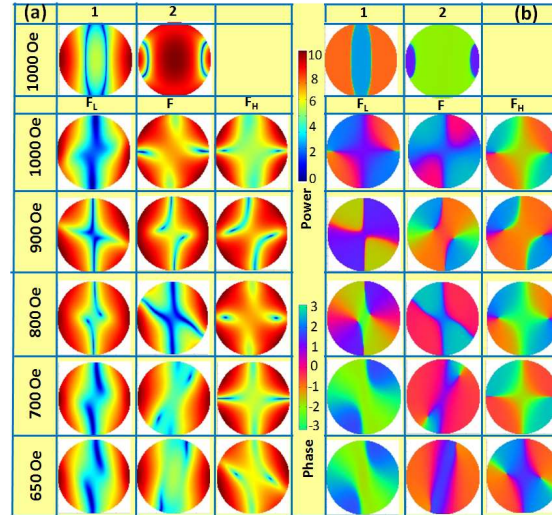


Fig. 8.6: (a) Simulated power and (b) phase profiles of the spin waves associated with the three dominant frequencies $F_L$, F and $F_H$ in the Kerr oscillations at any given bias field. The top most row shows edge and center modes at the two dominant frequencies in the Kerr oscillations in the absence of strain at 1000 Oe bias field. The units of power and phase are dB and radians, respectively.

On the other hand, the spin waves corresponding to the two modes at frequencies $F_L$ and $F_H$ appear as the modified edge mode and quantized mode of the nanomagnet. As the bias field is reduced, the mode with frequency F starts showing some quantization at the intermediate fields and finally transitions to edge mode like behavior in the low field regime. At an intermediate bias field of $H = 800$ Oe, the higher frequency mode ($F_H$) shows azimuthal character with $n = 5$. An important feature is that spin wave power is no longer concentrated along the vertical edges of the nanomagnet like in the conventional edge mode (perpendicular to the applied field) but gets slightly rotated. This is a consequence of having the SAW induced time-varying strain field present, along with the constant bias field in the system, and their competition.

## 8.5 Conclusion

In conclusion, laser-excited hybrid magneto-dynamical modes in a single quasi-elliptical nanomagnet of Co fabricated on top of a poled (001) PMN-PT substrate and subjected to a fixed bias magnetic field is studied. The frequencies of these modes are in the neighborhood of 10 GHz, corresponding to ~100 ps time scale dynamics. The spin wave textures of these modes display rich variation with the applied bias field. These results provide a glimpse of the complexity of ultrafast magnetization dynamics in magnetostrictive nanomagnets subjected to periodic strain (SAW) and could be important in future implementation of ultrafast switching in straintronic magnetic storage and logic devices.

# Chapter 9: Hardware Variant of Simulated annealing with time-varying strain in a dipole-coupled array of magnetostrictive nanomagnets

Consider a system of elliptical nanomagnets with in-plane magnetic anisotropy arranged as in Fig. 9.1 on a substrate. Because of the shape anisotropy, each nanomagnet will have an easy axis along the major axis, which will make its magnetization orient along one of two opposite directions along the major axis. Dipole interaction between the nanomagnets will result in the configuration shown in Fig. 9.1, where all nanomagnets along a column are magnetized in the same direction along the major axis, but alternating columns have opposite (anti-parallel) magnetizations. This is the ground state configuration.
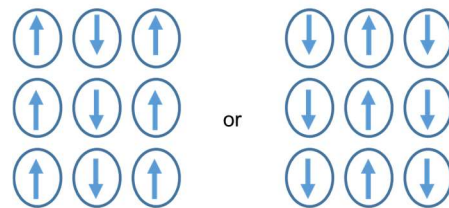


Fig. 9.1: Magnetization orientations in an array of dipole coupled elliptical nanomagnets

In order to verify that Fig. 9.1 is indeed the ground state configuration, we calculated the potential energy for a system of $3 \times 3$ array of elliptical cobalt nanomagnets of major axis dimension 350 nm, minor axis dimension 320 nm and thickness 12 nm, using the micromagnetic simulator MuMax3 which takes into account the demagnetizing field due to shape anisotropy, exchange interaction within a nanomagnet and dipole interaction between the nanomagnets. Since there are 9 nanomagnets in the $3 \times 3$ array, each with 2 possible orientations of the magnetization, there are $2^9 = 512$ possible combinations corresponding to 512 possible magnetic configurations. The energies of these combinations are plotted in Fig. 9.2. Clearly, there are two (degenerate) minimum energy configurations and they conform exactly to the two shown in Fig. 9.1.
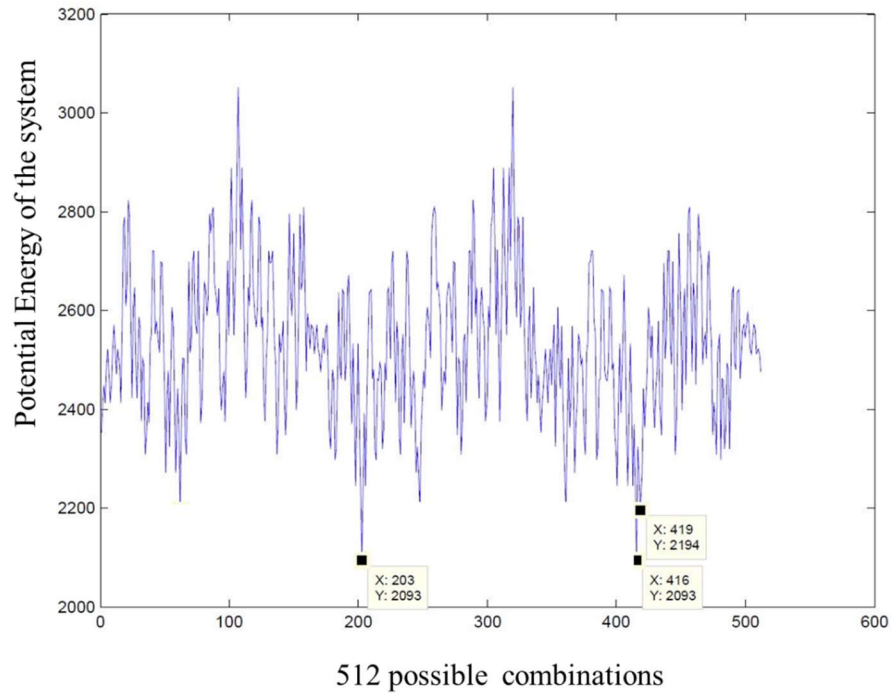
Fig. 9.2: Potential energies of various possible combinations of magnetic ordering in a $3 \times 3$ array of elliptical cobalt nanomagnets.

## 9.1 Hardware Variant of Simulated Annealing

In Fig. 9.3, we show the magnetic ordering of the $3 \times 3$ array, with the micromagnetic distribution within each nanomagnet, for one of the two ground state configurations.
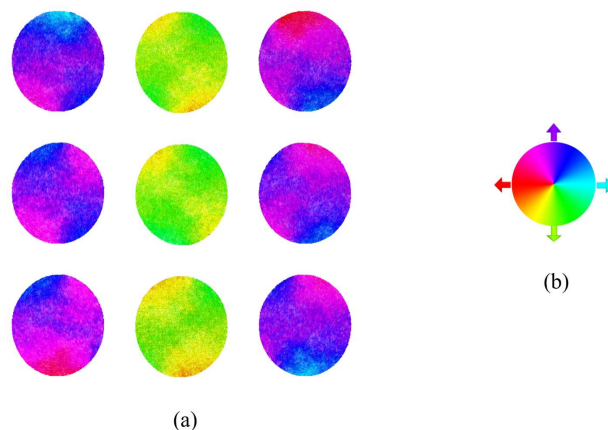


Fig. 9.3: (a) The computed magnetic ordering in a $3 \times 3$ array of elliptical cobalt nanomagnets. (b) Color wheel for the micromagnetic distribution within any nanomagnet (the color denotes the local magnetization direction within any nanomagnet)

Suppose now that the magnetizations are perturbed by an external agent (noise, stray magnetic field, etc.) which drives the system out of the ground state and destroys the ground state magnetic ordering in Fig. 9.1 or 9.3. The system may not be able to return spontaneously to the ground state if there are metastable states (caused by e.g. small variations in magnet shape or thickness, and/or structural defects such as material voids) and the system gets stuck in one of them. Internal energy barriers that separate the metastable state from the ground state will prevent the system to transition to the ground state. In this case, supplying energy from outside, or eroding the intervening energy barriers with an external agent, will allow the system to transition to the ground state. We can view this as a hardware emulation of simulated annealing [126] since the process allows the system to unpin itself and migrate from the metastable to the ground state. In a magnetostrictive nanomagnet system, *strain* can be the external agent that triggers the simulated annealing action. To understand why strain has this effect, consider the cartoon in Fig. 9.4(a) where we show the (arbitrary) potential profile inside a nanomagnet (potential energy versus magnetization orientation).
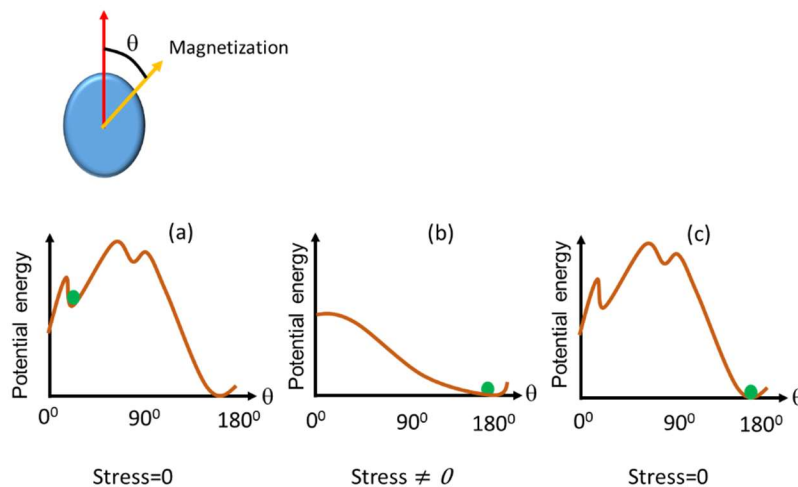


Fig. 9.4: Potential energy profile in a nanomagnet where θ denotes the magnetization orientation. (a) Owing to perturbation, the magnetization is stuck in a metastable state as denoted by the ball, (b) potential energy profile in the presence of stress where the barriers are removed and the magnetization can relax to the ground state, and (c) potential energy profile after removal of stress where the magnetization remains in the ground state.

We have assumed that the nanomagnet has imperfections such as edge roughness, thickness variations, material defects, etc. that cause the potential profile to have one or more metastable states that would be absent in an ideal (perfect) nanomagnet. There is a global energy minimum and some local energy minima, which are arbitrary in this figure because they are caused by random defects. Note that because of dipole coupling, one orientation along the major axis ($\theta = 180^0$) is slightly preferred over the other ($\theta = 0^0$).

If we perturb the magnetizations of one or more nanomagnets and drive the array out of the global energy minimum and pin it into a local minimum, the system will get stuck in the metastable state and cannot decay to the ground state because of the potential barriers separating the metastable and ground states as shown in Fig. 9.4(a). However, when we apply compressive or tensile strain, the energy landscape is altered and may look like the one in Fig. 9.4(b) as long as the product of the magnetostriction coefficient and strain is a negative quantity. Strain alters the potential landscape. Once that happens, the energy barrier(s) between the metastable and ground states is(are) eroded and the system can relax to the ground state configuration as shown in Fig. 9.4(c).

## 9.2 Fabrication of the Device

To test this model, we fabricated cobalt nanomagnets on a piezoelectric $128^0$ Y-cut Lithium Niobate (LiNbO$_3$) substrate using electron beam patterning of a resist, electron beam evaporation of cobalt on to the patterned substrate and lift-off. The contact electrodes for external connection are done using spin coating of photo-resist, photolithography and development, electron beam evaporation of gold and lift-off. The schematic diagram of the device structure and fabrication process flow is shown in figure 9.5.
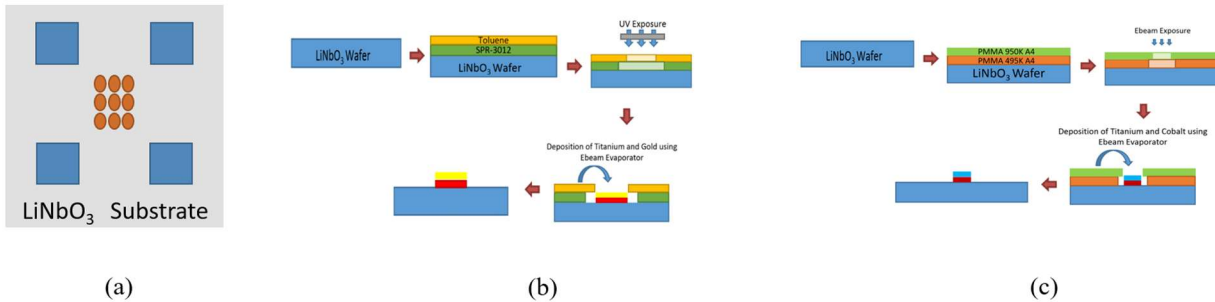
Fig. 9.5: (a) Schematic of the Device Structure, (a) Fabrication Process flow for Gold Contact Electrodes, and (c) Fabrication Process flow for Cobalt Nanomagnets

## 9.3 Experimental Results and Discussion

An atomic force micrograph of a $3 \times 3$ array of nanomagnets is shown in Fig. 9.5. The dimensions conform to the ones used for the simulation: major axis = 350 nm, minor axis = 320 nm and thickness = 12 nm.
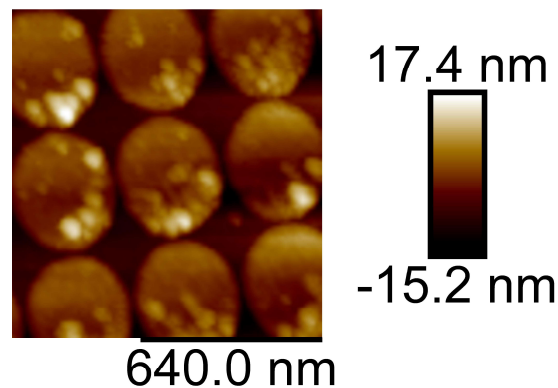


Fig. 9.6: Atomic force micrographs of elliptical cobalt nanomagnets fabricated on a $LiNbO_3$ substrate.

We then determined the magnetic ordering with magnetic force microscopy (MFM). The MFM image of the $3 \times 3$ array is shown in Fig. 9.7(a). We clearly see the ordering computed in Fig. 9.3, where the nanomagnets along a column are all magnetized in the same direction and alternating columns have opposite directions of magnetization. This image is obtained with a low-moment tip in order to carry out non-invasive imaging. Next, we intentionally perturb the magnetization in the

array with a high-moment tip and we show the MFM image of the resulting configuration after the perturbation in Fig. 9.7(b). Clearly the ground state ordering has been destroyed and the system has not spontaneously returned to the ground state (it is stuck in a metastable state). We then launch a surface acoustic wave (SAW) in the substrate, which periodically exerts tensile and compressive strain on the nanomagnets and rotates their magnetization via the Villari effect [14][39][120][121][127-138]. The SAW is launched by applying a sinusoidal voltage of 24 V and frequency of 3.57 MHz to one electrode as shown in the schematic of Fig. 9.5(a). The experimenatal setup is shown in Fig. 9.8. After the SAW excitation is terminated, we image the nanomagnets again, and find that the system has returned to the ground state. The SAW temporarily eroded the potential barriers that impeded transition from the metastable state to the ground state and allowed the system to relax to the ground state as shown in Fig. 9.7(c). This is an emulation of simulated annealing. Here, the periodic strain (SAW) acted as the simulated annealing agent.



Initial magnetization state

Magnetization state after perturbing with high moment tip

Magnetization state after subjecting to surface acoustic wave
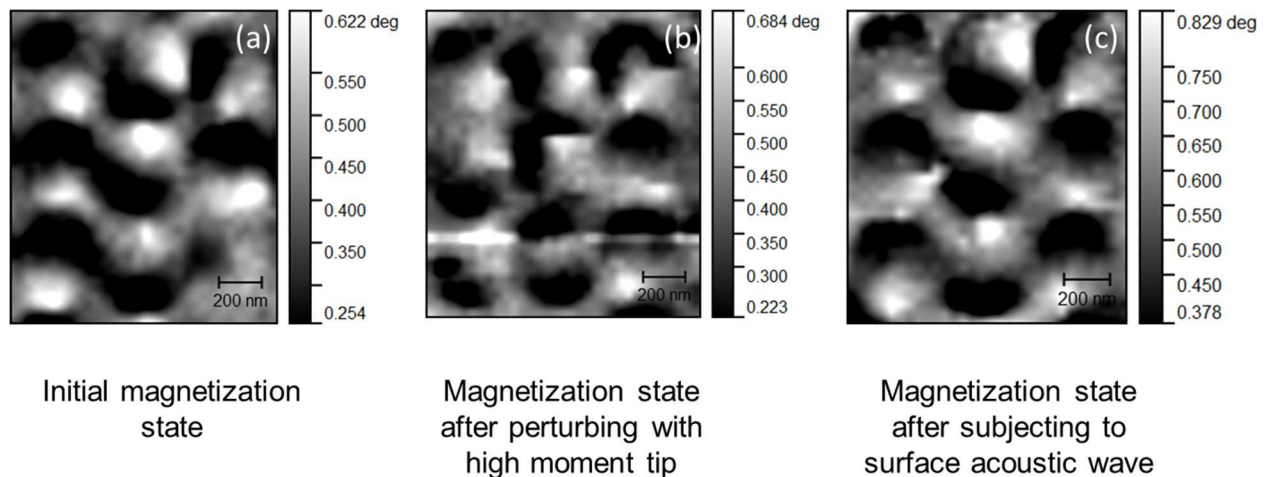
Fig. 9.7: Magnetic force microscopy images showing (a) the initial magnetization state, (b) the state after perturbation with a high moment tip and (c) the magnetization state after passage of the surface acoustic wave.
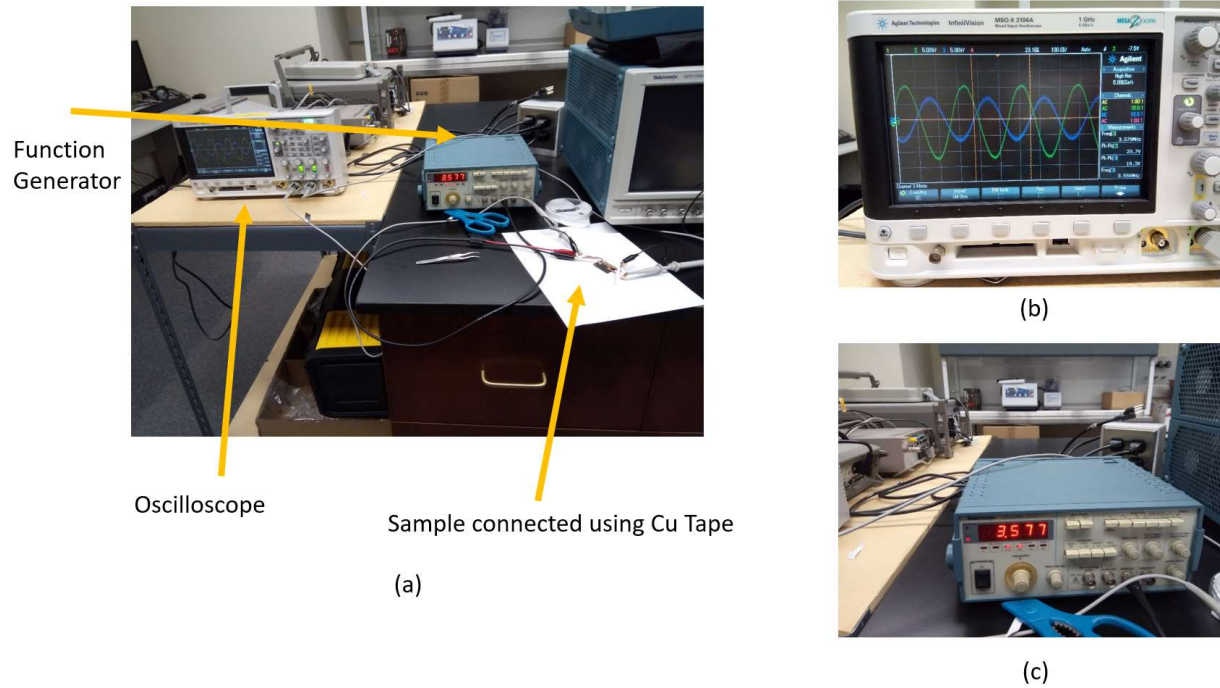
Fig. 9.8: (a) Experimental Setup for the SAW application, (b) View of the Oscilloscope showing input and output signal of the device and (c) View of the function generator showing the applied frequency.

## 9.4 Conclusion

In conclusion, we have shown that in an interacting system of magnetostrictive nanomagnets (interacting via dipole coupling), time-varying strain associated with a surface acoustic wave acts as an agent of simulated annealing. This is an example of hardware based simulated annealing.

**Chapter 10: Experimental Demonstration of a Nanomagnetic Acoustic Antenna Actuated by the Giant Spin Hall Effect from a Pt Nanostrip**

In most of the recent work with nanomagnetic antennas, the nanomagnets have been flipped with alternating strain generated, e.g. with an acoustic wave. This requires the nanomagnets to be magnetostrictive or multiferroic so that strain can rotate its magnetization via the Villari effect. A bulk acoustic wave mediated multiferroic antenna was recently proposed in [139]. In the analysis, it was shown that there is little electromagnetic radiation when the mechanical strain in the magnetostrictive layer is small. However, in the presence of significant strain, the emitted electromagnetic radiation is appreciable. Ref. [140] compared strain powered piezo-magnetic antennas to conventional electrical antennas and showed that appropriate design with high relative permittivity, strong piezo coupling and a high mechanical quality factor could lead to radiation efficiency superior to that of equally sized electric dipole antennas. Further improvement can be achieved by matching mechanical resonance to the ferromagnetic resonance. Experimentally, two type of acoustic wave based antennas – nanoplate resonator (NPR) and film bulk acoustic resonators (FBAR) – were fabricated [141]. These antennas have different resonance modes, providing a frequency range between tens of MHz and few GHz. Series and parallel arrays of such antennas were also studied which showed enhanced gain and bandwidth. These strain based antennas have dimensions considerably smaller than the wavelength of the emitted radiation and are therefore suitable for *in vivo* biological implantation [142][143]. They are preferred in these applications because they are immune to the platform effect and the magnetic near fields emanating from such antennas interact weakly with biological tissues. In this chapter, a *converse* effect is demonstrated based on Spin Hall Effect of Platinum.

## 10.1 Working Principle of Spin Hall Effect Actuated Acoustic Antenna

When an alternating charge current, passed through a heavy metal (Pt) strip that is in contact with an array of nanomagnets, which will then pass an alternating spin current through the nanomagnets

because of the giant spin Hall effect in Pt [144][145]. This results in alternating spin-orbit torque on the nanomagnets and periodically rotates their magnetization. As long as the period of the alternating charge current exceeds the time required to rotate the magnetization of the nanomagnets by a significant amount, the magnetizations of the nanomagnets will fluctuate periodically with sufficient amplitude and emit an electromagnetic wave. If the nanomagnets are magnetostrictive, then they will periodically expand and contact when their magnetizations are rotating, *provided they are not clamped by the Pt strip*. Furthermore, if the nanomagnets are deposited on a piezoelectric substrate, then their periodic expansion/contraction will generate a periodic strain in the underlying piezoelectric, leading to the propagation of a surface acoustic wave (SAW) in the substrate that can be detected with interdigitated transducers (IDT). This is the principle of the spin Hall effect actuated acoustic antenna. The generated surface acoustic wave will typically be a polychromatic wave, but the IDTs will filter out a particular frequency and detect that frequency component most efficiently. The measured efficiency of radiation will be the product of the efficiency of SAW generation by the nanomagnets and the efficiency of detection by the IDT.

The proposed acoustic antenna is shown schematically in Fig. 10.1. The nanomagnets are fabricated with a ledge (as shown in the inset) which is placed underneath a platinum nanostrip. The accumulated spins due to the spin hall effect at the surface of the Pt nanostrip which is in contact of the nanomagnets' ledges will diffuse into the "ledges" and from there into the nanomagnets. That will exert a spin-orbit torque on the nanomagnets and rotate their magnetizations. The alternating spin injection and the associated change in magnetization can be accomplished with an AC source injecting current into the Pt strip. As long as the frequency of the AC source is considerably smaller than the inverse of the spin flip times of the nanomagnets, we can alternately rotate the magnetizations of the nanomagnets in opposite directions with the AC

source. This alternating rotation will emit an electromagnetic wave, similar to spin torque nano-oscillators [102][146] and hence act as an electromagnetic antenna. At the same time, the nanomagnets will periodically expand and contract because they are magnetostrictive. Note that only the ledges are underneath the Pt strip while the main body of a nanomagnet is outside the strip. The purpose of this was to ensure that the nanomagnets are not clamped by the strip. The periodic expansion and contraction will generate periodic strain in the piezoelectric substrate and set up a SAW that can be detected with IDTs.
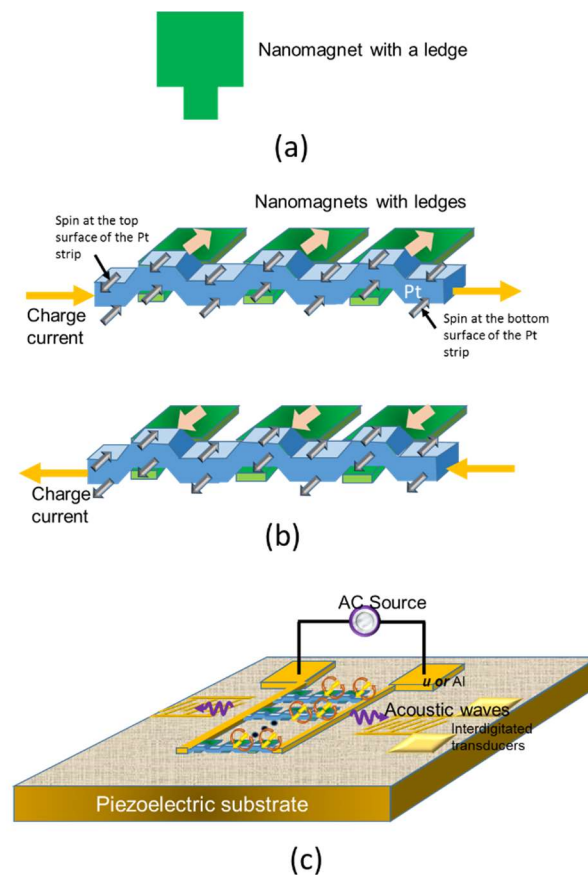


Fig. 10.1: (a) The top view of a nanomagnet with a ledge. (b) Principle of actuation of the antenna by the spin orbit torque in the heavy metal (Pt) nanostrip. For one polarity of the injected charge current, the nanomagnets are magnetized in one direction and for the opposite polarity, they are magnetized in the opposite direction. (c) The nanomagnets expand or contract as they transition between the two orientations and that generates a surface acoustic wave in the piezoelectric substrate which can be detected by interdigitated transducers delineated on the substrate.

## 10.2 Materials and Methods for the Experiment

The nanomagnets and Pt strip were fabricated on a $128^0$ Y-cut LiNbO$_3$ substrate. The substrate was spin-coated with bilayer PMMA e-beam resists of different molecular weights to obtain good undercut: PMMA 495 diluted 4% by volume in Anisole, followed by PMMA 950 also diluted 4% by volume in Anisole at a spin rate of 2500 rpm. The resists were baked at $110^0$ Celsius for 2 min. Next, electron-beam lithography is performed using a Hitachi SU-70 scanning electron microscope (at an accelerating voltage of 30 kV and 60 pA beam current) with a Nabity NPGS lithography system. Subsequently, the resists were developed in MIBK−IPA (1:3) for 270 s followed by a cold IPA rinse. For nanomagnet delineation, a 5 nm thick Ti adhesion layer was first deposited using e-beam evaporation at a base pressure of $\sim 2 \times 10^{-7}$ Torr, followed by the deposition of Co. Pt was deposited similarly. The liftoff was carried out using Remover PG solution.

In Fig. 10.2(a), the schematic of the acoustic antenna is shown and in Fig. 10.2(b), a scanning electron micrograph of the fabricated nanomagnets is shown.
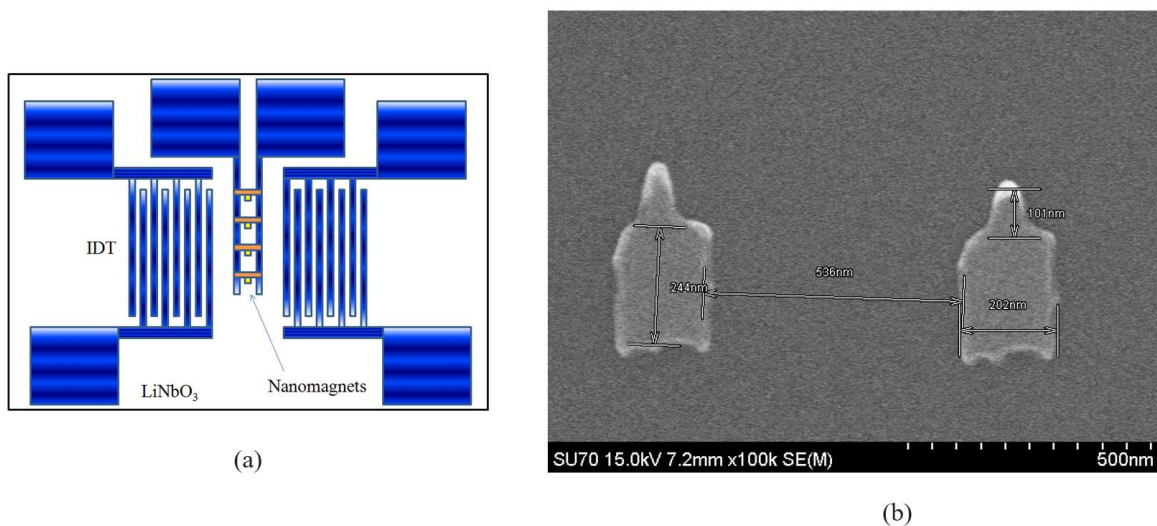


Fig. 10.2: (a) The schematic for the acoustic antenna. (b) Scanning electron micrographs of the fabricated Co nanomagnets.

The nanomagnets are rectangular with long dimension ~250 nm, short dimension ~200 nm and the ledge length is ~100 nm. The ledge has a "Gaussian" shape and the full width at half maximum is ~70 nm. In Fig. 10.3, the scanning electron micrographs of the Pt line and nanomagnet assembly are shown.
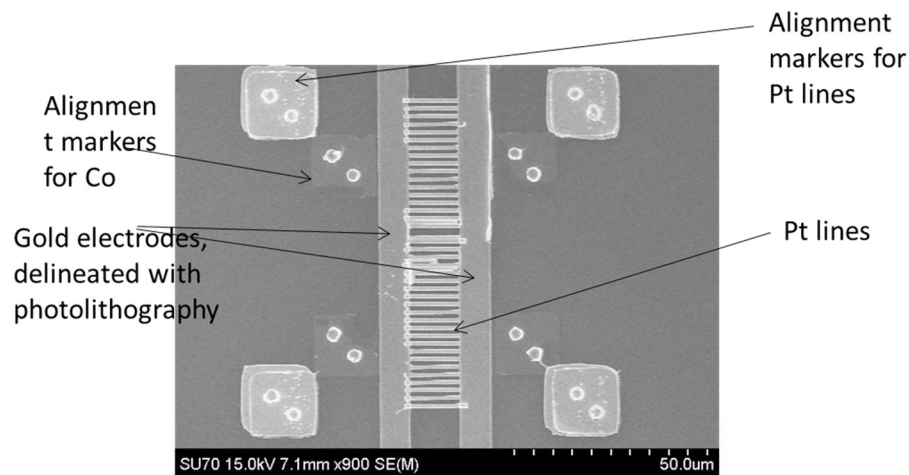


(a)
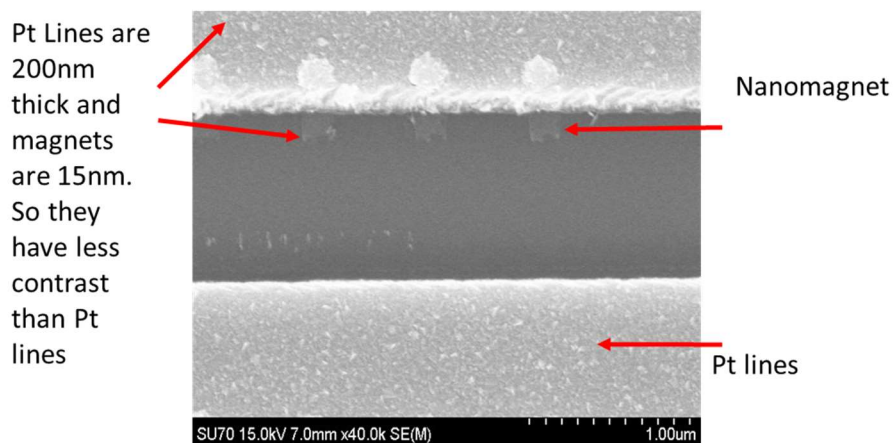


(b)

Fig. 10.3: (a) Scanning electron micrograph of the Pt lines overlying the nanomagnets. (b) Zoomed view showing the nanomagnets underneath the Pt lines.

## 10.3 Results And Discussion

In Fig. 4, the oscilloscope traces of the sinusoidal voltage applied across the Pt lines to actuate the acoustic antenna via spin-orbit torque and the voltage detected at the interdigitated transducers (IDT) are shown. These plot for two frequencies, 3.63 MHz which is the resonant frequency of the IDT, and 6.87 MHz are shown.

The resistance of the Pt lines varied between 98 ohms and 108 ohms from sample to sample. The resistance is on the order of 100 ohms. For the case in Fig. 4(a), the peak to zero input voltage of 11.25 V will produce a current of 112.5 mA in the Pt strip. The strip has a length of 15 μm, width 1 μm and thickness 200 nm. Therefore, the current density produced by the current is $5.625\times10^{11}$ A m$^{-2}$, which should be well above the critical current needed to produce spin-orbit torque. In the case of Fig. 4(b), the peak to zero input voltage of 12.85 V produced a current of 128.5 mA in the Pt strip, resulting in a current density of $6.425\times10^{11}$ A m$^{-2}$. The input power to produce the acoustic radiation detected by the IDTs is calculated as $\frac{V_{in}^2}{2R_{Pt}}$ where $V_{in}$ is the peak to zero input voltage and $R_{Pt}$ is the Pt line resistance. For the case in Fig. 4(a), this quantity is 633 mW. For the case in Fig. 4(b), the input power is 825 mW. In order to calculate the radiation efficiency, we have to know the power in the acoustic wave that has been produced. The power carried by an acoustic wave of amplitude $\phi$ is given by [147]

$$P = \frac{1}{2}y_0\frac{W}{\lambda}\phi^2, \qquad (1)$$

where $y_0$ is the characteristic admittance of the SAW line and has a value of $2.1\times10^{-4}$ S for LiNbO$_3$ [147], $W$ is the width of the IDT and λ is the wavelength of the SAW. In the case of Fig. 4(a), $W/\lambda = 40$.

Neglecting capacitive and inductive effects, the voltage $V_{out}$ detected at the IDT is related to the SAW amplitude $\phi$ as [147]

$$\phi \approx \mu V_{out} , \qquad\qquad (2)$$

where $\mu$ is the response function of an IDT operating in the transmitting mode. For our system, this quantity was calculated in ref. [120] as approximately 2. Hence, in Fig. 4(a), $\phi$= 0.9 V peak-to-zero and in Fig. 4(b), $\phi$= 1.6 V peak-to-zero. Therefore, from Equation (2), the SAW power produced in the two cases are 3.4 mW and 10.7 mW, respectively. The corresponding efficiencies of SAW production are 0.54% and 1.29%, respectively. These numbers are approximate because of some simplifying assumptions such as neglecting inductive and capacitive effects.

One important question that needs to be resolved before proceeding further is whether the output voltage detected at the IDT is direct electromagnetic pick up from the input. This could never have produced the phase shifts (time delay) seen between the input and output signals in Fig. 4. The distance between the input and output ports is 6 mm and the time that would take electromagnetic wave to traverse this distance is 20 ps. At a frequency of 3.63 MHz (Fig. 4a), this would produce a phase lag of 4.56 x$10^{-4}$ radians, which is much smaller than what is observed. For an acoustic wave with a velocity 5 orders of magnitude smaller than electromagnetic waves, the phase shift will be $7.26 \times 2\pi$ radians = $7 \times 2\pi + 0.26 \times 2\pi$ radians. When the modulo $2\pi$ value is taken, this is 1.63 radians. The observed phase shift is about 2.28 radians which is much closer to the acoustic phase shift than the electromagnetic phase shift. This gives us confidence that the detected signal is not due to electromagnetic pick up.
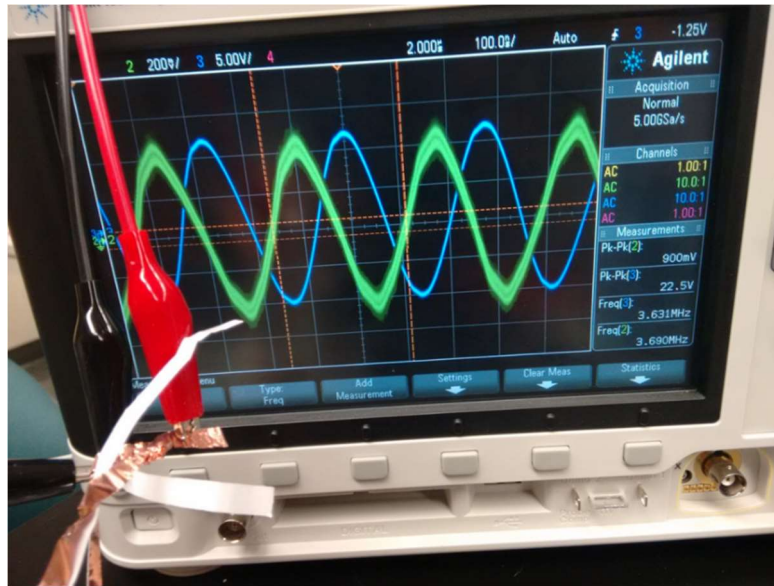
(a)
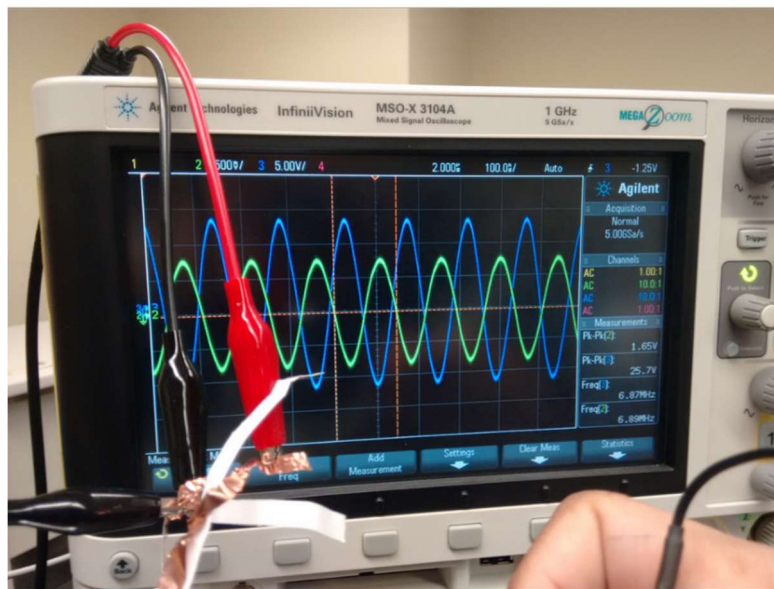


(b)

Fig. 10.4: Oscilloscope traces of the alternating voltage applied across the Pt lines to actuate the acoustic antenna (blue) and the alternating voltage detected at the interdigitated transducer (green). They are respectively the input and output signals. (a) The input voltage frequency is 3.63 MHz which is the resonant frequency of the interdigitated transducers (IDT) determined by the spacing of the IDT fingers and the velocity of surface acoustic wave in the substrate. Input voltage peak to peak amplitude is 22.5 V and the detected voltage peak-to-peak amplitude is 0.9 V. (b) The input voltage frequency is 6.87 MHz and the peak-to-peak amplitude is 25.7 V, while the detected voltage peak-to-peak amplitude is 1.65 V.

## 10.4 Conclusion

In conclusion, an acoustic antenna actuated by the spin-orbit torque from a heavy metal that exhibits the giant spin Hall effect is demonstrated. This results in the conversion of photons in the input low frequency electromagnetic wave to phonons in the surface acoustic wave. This is the converse of the phenomenon in refs. [139-144] which converted phonons to photons. Ref. [148] reported a similar phenomenon of converting spin current to phonons, but not in the context of an antenna, although the physics is the same.

**Chapter 11: Conclusion**

Straintronic nanomagnetic devices can be switched with very low energy dissipation. But this switching scheme is unfortunately more unreliable than many others. There seems to be a trade-off between energy dissipation and error rate, which may be a universal feature. The high switching error probability in straintronic switching might preclude applications in either Boolean logic or memory. In this thesis, I investigated one of the primary causes of switching error, namely material fabrication defects and surface roughness. Expectedly, I found that defects increase the switching error rate by several orders of magnitude. Analog spin wave and probabilistic computing devices are not immune to errors caused by defects, either. Theoretical simulations showed that defects quench spin wave modes and spawn new ones. Resonant (confined) spin wave modes were studied experimentally in a single nanomagnet strained with surface acoustic wave using time resolved magneto-optical Kerr effect. Novel hybrid spin wave modes were found for the first time.

Image processing using dipole coupled nanomagnets was simulated and certain functionalities could be demonstrated, although the system is not capable of acting as a universal general-purpose image processor. Image processing exploits the collective behavior of an array of coupled nanomagnets and is relatively resilient against error since it does not rely on the action of a single nanomagnet. The system is a hardware platform for image processing (no software needed) and performs energy efficient noise removal and edge enhancement of corrupted pixels in an image.

A single MTJ based microwave oscillator whose operation is governed by the complex interplay among the strain anisotropy, shape anisotropy, dipolar magnetic field and spin transfer torque is also demonstrated theoretically. It has a much higher quality factor than spin-torque-nano-oscillators.

A novel interacting magnetic many body system was made to emulate simulated annealing under the influence of time varying strain in a surface acoustic wave. A spin Hall effect actuated surface acoustic wave antenna was also demonstrated. The radiation efficiency was disappointingly poor (~1%), but the phenomenon is novel and demonstrates conversion of photons to magnons to phonons.

The work in this thesis can help to sketch out the future direction for straintronics. Some applications are more promising than others and resources are best spent pursuing the more promising avenues.

# Author Biography and List of Publications

Md Ahsanul Abeed received the B.Sc. degree in electrical and electronic engineering from the Bangladesh University of Engineering and Technology, Dhaka, Bangladesh, in 2013. This thesis is the final requirement of the Ph.D. degree he is pursuing with the Department of Electrical and Computer Engineering, Virginia Commonwealth University, Richmond, VA, USA.

His research interests include modeling, fabrication and characterization of spintronic devices for logic, memory and non-Boolean computing applications.

**Journals**

**Published:**

- **M. A. Abeed,** J. L. Drobitch and S. Bandyopadhyay, "A Microwave Oscillator based on a Single Straintronic Magneto-tunneling Junction Utilizing a Two-Phase Multiferroic Soft Layer," Physical Review Applied, 2019.

- **M. A. Abeed**, J. Atulasimha, S. Bandyopadhyay, "Magneto-elastic switching of magnetostrictive nanomagnets with in-plane anisotropy: The effect of material defects," Journal of Physics: Condensed Matter, Vol 30, 394001, 2018.

- **M. A. Abeed**, A. K. Biswas, M. M. Al-Rashid, J. Atulasimha, and S. Bandyopadhyay, "Image Processing With Dipole-Coupled Nanomagnets: Noise Suppression and Edge Enhancement Detection," IEEE Transactions on Electron Devices, vol. PP, no. 99, pp. 1–8, 2017.

- S. Mondal, **M. A. Abeed**, K. Dutta, A. De, S. Sahoo, A. Barman, and S. Bandyopadhyay, "Hybrid Magnetodynamical Modes in a Single Magnetostrictive Nanomagnet on a

Piezoelectric Substrate Arising from Magnetoelastic Modulation of Precessional Dynamics," ACS Applied Materials & Interfaces 2018.

- N. D'Souza, A.K. Biswas, H. Ahmad, M. S. Fashami, M.M. Al-Rashid, V. Sampath, D. Bhattacharya, **M. A. Abeed**, J. Atulasimha, S. Bandyopadhyay, "Energy-efficient switching of nanomagnets for computing: straintronics and other methodologies," Nanotechnology, Vol 29, 442001, 2018.

- J. L. Drobitch, **M. A. Abeed** and S. Bandyopadhyay, "Precessional switching of a perpendicular anisotropy magneto-tunneling junction without a magnetic field," *Jpn. J. Appl. Phys.*, vol. 56, no. 10, p. 100309, Sep. 2017.

**In Press:**

- **M. A. Abeed**, S. Bandyopadhyay, "Low Barrier Nanomagnet Design for Binary Stochastic Neurons: Design Challenges for Real Nanomagnets with Fabrication Defects," IEEE Magnetics Letters, 2019.

**Submitted and Under Review:**

- **M. A. Abeed**, S. Sahoo, D. Winters, A. Barman and S. Bandyopadhyay, " The effect of material defects on resonant spin wave modes in a nanomagnet," Submitted to Nature Scientific Report (Under Review)

- D. Winters, **M. A. Abeed**, S. Sahoo, A. Barman and S. Bandyopadhyay, "Error Probability in Magneto-elastic Switching of Non-ideal Nanomagnets with Defects: A Case Study for the Viability of Straintronic Logic and Memory," Submitted to Physical Review Applied (Under Review)

- **M. A. Abeed**, and S. Bandyopadhyay, "Simulated annealing with time-varying strain in a dipole-coupled array of magnetostrictive nanomagnets," Submitted to Applied Physics Letters (Under Review) (https://arxiv.org/abs/1908.00893)

- **M. A. Abeed**, and S. Bandyopadhyay, "Experimental Demonstration of a Nanomagnetic Acoustic Antenna Actuated by the Giant Spin Hall Effect in a Pt Nanostrip ," Submitted to ACS Applied Materials and Interfaces (Under Review)

- **M. A. Abeed** and S. Bandyopadhyay, "Sensitivity of the Power Spectra of Magnetization Fluctuations in Low Barrier Nanomagnets to Barrier Height Modulation and Defects." (Submitted To Spin – World Scientific)

- M. T. McCray, **M. A. Abeed**, and S. Bandyopadhyay, "A Nanomagnetic Voltage-Tunable Correlation Generator between Two Random Bit Streams for Stochastic Computing." (Submitted To IEEE Journal of Exploratory Solid State Computational Devices and Circuits)

## CONFERENCE ATTENDED & PRESENTATION

- M. A. Abeed, S. Sahoo, D. Winters, A. Barman, S. Bandyopadhyay, "The Effect of Defects on Precessional Dynamics in a Magnetic Field and Resulting Spin Wave Modes in Elliptical Nanomagnets with In-Plane Anisotropy", Bulletin of the American Physical Society, March Meeting 2019.

# References

1. K. Roy , S. Bandyopadhyay,  and J. Atulasimha,  "Binary switching in a 'symmetric' potential landscape.," Scientific Reports, 3, p. 3038, 2013

2. A. K. Biswas, S. Bandyopadhyay, J. Atulasimha, "Complete magnetization reversal in a magnetostric-tive nanomagnet with voltage-generated stress: A reliable energy-efficient non-volatile magneto-elastic memory," Appl. Phys. Lett., 105, 072408, 2014

3. A. K. Biswas, H. Ahmad, J. Atulasimha, S. Bandyopadhyay, "Experimental demonstration of complete 180° reversal of magnetization in isolated Co nanomagnets on a PMN-PT substrate with voltage generated strain," Nano Lett. 17 3478, 2017

4. A. K. Biswas, J. Atulasimha, S. Bandyopadhyay, "An error-resilient non-volatile magneto-elastic universal logic gate with ultralow energy-delay product," Sci. Rep. 4, 7553, 2014

5. S. Ikeda, J. Hayakawa, Y. Ashizawa, Y. M. Lee, K. Miura, H. Hasegawa, M. Tsunoda, F. Matsukura and H. Ohno, "Tunnel magnetoresistance of 604% at 300 K by suppression of Ta diffusion in CoFeB/MgO/CoFeB pseudo spin valves annealed at high temperature," Appl. Phys. Lett., **93**, 082508, 2008.

6. M. A. Abeed , A. K. Biswas, M. M. Al-Rashid, J. Atulasimha,S. Bandyopadhyay, "Image processing with dipole-coupled nanomagnets: noise suppression and edge enhancement detection," IEEE Trans. Electron Devices 64 2417, 2017

7. M. A. Abeed, J. Atulasimha, S. Bandyopadhyay, "Magneto-elastic switching of magnetostrictive nanomagnets with in-plane anisotropy: The effect of material defects," Journal of Physics: Condensed Matter, Vol 30, 394001, 2018.

8. D. M. Winters, M. A. Abeed, S. Sahoo, A. Barman and S. Bandyopadhyay, "Error probability in magneto-elastic switching of non-ideal nanomagnets with defects: A case study for the viability of straintronic logic and memory," 2019. (https://arxiv.org/abs/1905.09322).

9. M. A. Abeed, S. Sahoo, D. Winters, A. Barman and S. Bandyopadhyay, " The effect of material defects on resonant spin wave modes in a nanomagnet," (Under Review in Nature Scientific Report)

10. O. Hassan, R. Faria, K. Y. Camsari, J. Z. Sun, and S. Datta, "Low barrier magnet design for efficient hardware binary stochastic neurons," IEEE Magnetics Lett. 10 4502805, 2019.

11. M. A. Abeed, S. Bandyopadhyay, "Low Barrier Nanomagnet Design for Binary Stochastic Neurons: Design Challenges for Real Nanomagnets with Fabrication Defects," IEEE Magnetics Letters, 2019 (In Press).

12. M. A. Abeed, J. L. Drobitch and S. Bandyopadhyay, "A Microwave Oscillator based on a Single Straintronic Magneto-tunneling Junction Utilizing a Two-Phase Multiferroic Soft Layer," Physical Review Applied, Vol 11(5), 054069, 2019.

13. M. T. McCray, M. A. Abeed, and S. Bandyopadhyay, "A Nanomagnetic Voltage-Tunable Correlation Generator between Two Random Bit Streams for Stochastic Computing," 2019. (https://arxiv.org/abs/1907.07532)

14. S. Mondal, **M. A. Abeed**, K. Dutta, A. De, S. Sahoo, A. Barman, and S. Bandyopadhyay, "Hybrid Magnetodynamical Modes in a Single Magnetostrictive Nanomagnet on a Piezoelectric Substrate Arising from Magnetoelastic Modulation of Precessional Dynamics," ACS Applied Materials & Interfaces, Vol 10 (50), 43970-43977, 2018.

15. M. Balaji and S. A. Christe, "FPGA implementation of various image processing algorithms using Xilinx system generator", in Computational Intelligence in Data Mining, vol. 2, Eds. L. C. Jain, H. S. Behera, J. K. Momdal and D. P. Mohapatra, (Springer, New York, 2015), pp. 59-68.

16. W. H. Lee and P. Mazumder, "Color image processing with multi- peak resonant tunneling diodes", ACM J. on Emerging Technologies in Computing Systems, Vol. 9, no. 3, 18, 2013.

17. V. P. Roychowdhury, D. B. Janes, S. Bandyopadhyay and X. D. Wang, "Collective computational activity in self-assembled arrays of quantum dots: A novel neuromorphic architecture for nanoelectronics", IEEE Trans. Elec. Dev., Vol. 43. no. 10, pp. 1688-1699, 1996.

18. K. Karahaliloglu, S. Balkir, S. Pramanik and S. Bandyopadhyay, "A quantum dot image processor", IEEE Trans. Elec. Dev., Vol. 50. no. 7, pp. 1610-1616, 2003.

19. N. Tiercelin, Y. Dusch, V. Preobrazhensky, and P. Pernod, "Magnetoelectric memory using orthogonal magnetization states and magnetoelastic switching," J. Appl. Phys., vol. 109, no. 7, pp. 1–4, 2011.

20. A. K. Biswas, S. Bandyopadhyay, and J. Atulasimha, "Energy-efficient magnetoelastic non-volatile memory," Appl. Phys. Lett., vol. 104, p. 232403, 2014.

21. K. Roy, S. Bandyopdhyay and J. Atulasimha, "Hybrid spintronics and straintronics: A magnetic technology for ultralow energy computing and signal processing", Appl. Phys. Lett., vol. 99, no. 6, 023914, 2011.

22. M. Salehi-Fashami, K. Roy, J. Atulasimha and S. Bandyopadhyay, "Magnetization dynamics, Bennett clocking and associated energy dissipation in multiferroic logic", Nanotechnology, vol. 22, 155201, 2011.

23. J. Z. Cui, J. L. Hockel, P. K. Nordeen, D. M. Pisani, C-y Liang, G. P. Carman and C. S. Lynch, "A method to control magnetism in individual strain-mediated magnetoelectric islands", Appl. Phys. Lett., vol. 103, 232905, 2013.

24. C-Y Liang, S. M. Keller, A. E. Sepulveda, W. Y. Sun, J. Z. Cui, C. S. Lynch and G. P. Carman, "Electrical control of single magnetoelastic domain structure on a clamped piezoelectric thin film - analysis", J. Appl. Phys., vol. 116, 123909, 2014.

25. J. Z. Cui, C-y Liang, E. A. Paisley, A. Sepulveda, J. F. Ihlefeld, G. P. Carman and C. S. Lynch, "Generation of localized strain in a thin film piezoelectric to control individual magnetoelectric heterostructures", Appl. Phys. Lett., vol. 107, 092903, 2015.

26. G. Dewar, "Effect of the large magnetostriction of Terfenol-D on microwave transmission," J. Appl. Phys., vol. 81, no. 8, pp. 5713–5715, 1997.

27. J. L. Butler, Application manual for the design of ETREMA Terfenol-D magnetostrictive transducers. ETREMA Products, Incorporated, 1988.

28. P. Farber and H. Kronmüller, "Crystallization behaviour and magnetic properties of highly magnetostrictive Fe–Tb–Dy thin films," J. Magn. Magn. Mater., vol. 214, no. 3, pp. 159–166, 2000.

29. D. B. Gopman, J. W. Lau, K. P. Mohanchandra, K. Wetzlar, and G. P. Carman, "Determination of the exchange constant of Tb 0.3 Dy 0.7 Fe 2 by broadband ferromagnetic resonance spectroscopy," Phys. Rev. B, vol. 93, no. 064425, 2016.

30. A. Vansteenkiste, J. Leliaert, M. Dvornik, M. Helsen, F. Garcia-Sanchez, and B. Van Waeyenberge, "The design and verification of MuMax3," AIP Adv., vol. 4, no. 10, p. 107133, 2014.

31. N. D'Souza, J. Atulasimha and S. Bandyopadhyay, "An ultrafast image recovery and recognition system implemented with nanomagnets possessing biaxial magnetocrystalline anisotropy," IEEE Trans.Nanotechnol., Vol. 11, no. 5, 896-901, 2012.

32. A. Khitun, M. Q. Bao and K. L. Wang, "Magnetic cellular nonlinear network with spin wave bus for image processing", Superlatt. Microstruct., Vol. 47, no. 3, pp. 464-483, 2010.

33. H. Ahmad, J. Atulasimha and S. Bandyopadhyay, "Reversible strain-induced magnetization switching in FeGa nanomagnets: Pathway to a re-writable, non-volatile, non-toggle extremely low energy straintronic memory", Sci. Rep., Vol. 5, 18264, 2015.

34. N. D'Souza, M. Salehi-Fashami, S. Bandyopadhyay and J. Atulasimha, "Experimental clocking of nanomagnets with strain for ultralow power Boolean logic", Nano Lett., Vol. 16, no. 2, pp. 1069-1075, 2016.

35. Z. Zhao, M. Jamali, N. D'Souza, D. Zhang, S. Bandyopadhyay, J. Atulasimha, and J. P Wang, "Giant voltage manipulation of MgO-based magnetic tunnel junction via localized anisotropic strain: A potential pathway to ultra-energy-efficient memoy technology," *Appl. Phys. Lett*. **109** 092403, 2016.

36. H. Ahmad, J. Atulasimha, and S. Bandyopadhyay, "Reversible strain-induced magnetization switching in FeGa nanomagnets: Pathway to a rewritable, non-volatile, non-toggle, extremely low energy straintronic memory," *Sci. Rep*. **5** 18264, 2015.

37. H. Ahmad, J. Atulasimha, and S. Bandyopadhyay, "Electric field control of magnetic states in isolated and dipole-coupled FeGa nanomagnets delineated on a PMN-PT substrate," *Nanotechnology* **26** 401001, 2015.

38. K. Munira, Y. Xie, S. Nadri, M. B. Forgues, M. Salehi-Fashami, J. Atulasimha, S. Bandyopadhyay, and A. W. Ghosh, "Reducing error rates in straintronic multiferroic nanomagnetic logic by pulse shaping," *Nanotechnol.* **26** 245202, 2015.

39. V. Sampath, N. D'Souza, G. M. Atkinson, S. Bandyopadhyay and J. Atulasimha, "Experimental demonstration of acoustic wave induced magnetization switching in dipole coupled magnotostrictive nanomagnets for ultralow power computing," *Appl. Phys. Lett*. **109** 102403, 2016.

40. M. Yaseen, W. Ren, X. Chen, Y. Feng, P. Shi, and X. Wu, "Effects of thickness, pulse duration, and size of strip electrode on ferroelectric electron emission of lead zirconate titanate films," *J. Elec. Mater*. **57** 1183, 2018.

41. E. W. Lee, "Magnetostriction and magneto-mechanical effects." *Rep. Prog. Phys*. **18** 184, 1955.

42. R. Abbundi and A. E. Clark, "Anomalous thermal expansion and $Tb_{0.27}Dy_{0.73}Fe_2$," *IEEE Trans. Mag.* **13** 1547, 1977.

43. D. Bhattacharya, M. M. Al-Rashid, N. D'Souza, S. Bandyopadhyay, and J. Atulasimha, "Incoherent magnetization dynamics in strain mediated switching of magnetostrictive nanomagnets," *Nanotechnology* **28** 015202, 2016.

44. A. C. Chavez, W.-Y. Sun, J. Atulasimha, K. L. Wang, and G. P. Carman, "Voltage induced artificial ferromagnetic-antiferromagnetic ordering in synthetic multiferroics," *J. Appl. Phys.* **122** 224102, 2017.

45. A. Spinelli, B. Bryant, F. Delgado, J. Fernández-Rossier, & A. F. Otte, "Imaging of spin waves in atomically designed nanomagnets," *Nature Mater*. **13**, 782-785, 2014.

46. A. Khitun, M. Bao, & K. L. Wang, "Magnonic logic circuits," *J. Phys. D: Appl. Phys*. **43**, 264005, 2010.

47. T. Schneider, A.A. Serga, B. Leven, & B. Hillebrands, "Realization of spin-wave logic gates," *Appl. Phys. Lett*. **92**, 022505, 2008.

48. T. Chen, et al., "Spin-torque and spin-Hall nano-oscillators," *Proc. IEEE* **104**, 1919-1945, 2016.

49. K. Yogendra, D. Fan, & K. Roy, "Coupled spin-torque nano-oscillators for low power neural computation," *IEEE Trans. Magn.***51**, 4003939, 2015.

50. A. Barman, & J. Sinha, " Spin dynamics and damping in ferromagnetic thin films and nanostructures," (Springer, Switzerland, 2018).

51. S. Jung, B. Watkins, L. DeLong, J. B. Ketterson, & V. Chandrasekhar, "Ferromagnetic resonance in periodic particle arrays," *Phys. Rev. B* **66**, 132401, 2002.

52. G. Gubbiotti, M. Conti, G. Carlotti, P. Candeloro, E. Di Fabrizio, K. Y. Guslienko, A. Andre, C. Bayer, & A. N. Slavin, "Magnetic field dependence of quantized and localized spin wave modes in thin rectangular magnetic dots," J. Phys. Cond. Matter **16** 7709, 2004.

53. V. V. Kruglyak, A. Barman, R. J. Hicken, J. R. Childress, & J. A. Katine, " Precessional dynamics in microarrays of nanomagnets," *J. Appl. Phys*. **97**, 10A706, 2005.

54. A. Barman, S. Wang, J. D. Maas, A. R. Hawkins, S. Kwon, A.Liddle, J.Bokor, & H. Schmidt, "Magneto-optical observation of picosecond dynamics of single nanomagnets," *Nano Lett*. **6**, 2939 2006.

55. P.S. Keatley, V. V. Kruglyak, A. Neudert, E. A. Galaktionov, R. J. Hicken, J. R Childress, & J. A. Katine, "Time-resolved investigation of magnetization dynamics of arrays of non-ellipsoidal nanomagnets with non-uniform ground states," *Phys. Rev. B* **78**, 214412, 2008.

56. A. Barman, & S. Barman, "Dynamic dephasing of magnetization precession in arrays of thin magnetic elements," *Phys. Rev. B* **79**, 144415, 2009.

57. V. V. Kruglyak, P.S. Keatley, A. Neudert, R. J. Hicken, J. R. Childress, & J. A. Katine, "Imaging collective magnonic modes in 2D arrays of magnetic nanoelements," *Phys. Rev. Lett*. **104**, 027201, 2010.

58. J. M. Shaw, T. J. Silva, M. L. Schneider, & R. D. McMichael, "Spin dynamics and mode structure in nanomagnet arrays: Effects of size and thickness on linewidth and damping," *Phys. Rev. B* **79**, 184404, 2009.

59. R. Zivieri, F. Montoncello, L. Giovannini, F. Nizzoli, S. Tacchi, M. Madami, G. Gubbiotti, G. Carlotti, & A. O. Adeyeye, "Collective spin modes in chains of dipolarly interacting rectangular magnetic dots," *Phys. Rev. B* **83**, 054431, 2011.

60. B. Rana, D. Kumar, S. Barman, S. Pal, Y. Fukuma, Y. Otani, & A. Barman, "Detection of picosecond dynamics of 50 nm magnetic dots down to the single dot regime," *ACS Nano* **5**, 9559, 2011.

61. P.S. Keatley, P. Gangmei, M. Dvornik, R. J. Hicken, J. Grollier, & C. Ulysse, "Isolating the dynamics dipolar interaction between a pair of nanoscale ferromagnetic disks, "*Phys. Rev. Lett*. **110**, 187202, 2013.

62. S. Saha, R. Mandal, S. Barman, D. Kumar, B. Rana, Y. Fukuma, S. Sugimoto, Y. Otani, & A. Barman, "Tunable magnonic spectra in two-dimensional magnonic crystals with variable lattice symmetry," *Adv. Funct. Mater*. **23**, 2378, 2013.

63. J. Ding, & A. O. Adeyeye,"Binary ferromagnetic nanostructures: Fabrication, static and dynamics properties," *Adv. Funct. Mater*. **23**, 1684, 2013.

64. K. Adhikari, S. Barman, Y, Otani, & A. Barman, " Tunable angle dependent magnetization dynamics in $Ni_{80}Fe_{20}$nanocross structures of varying size," *Phys. Rev. Appl*.**10**, 044010, 2018.

65. A. Haldar, D. Kumar, & A. O. Adeyeye, "A reconfigurable waveguide for energy-efficient transmission and local manipulation of information in a nanomagnetic device," *Nat. Nanotechnol*. **11**, 437, 2016.

66. J. Torrejon, et al., "Neuromorphic computing with nanoscale spintronic oscillators," *Nature* **547**, 428-431, 2017.

67. D. Kumar, O. Dmytriiev, S. Ponraj, & A. Barman, " Numerical calculation of spin wave dispersions in magnetic nanostructures," *J. Phys. D: Appl. Phys*. **45**, 015001, 2012.

68. A. Barman, V. V. Kruglyak, R. J. Hicken, J. M. Rowe, A. Kundrotaite, J. Scott, & M. Rahman, "Imaging the dephasing of spin wave modes in a square thin magnetic element," *Phys. Rev. B*. **69**, 174226, 2004.

69. J. R. Eshbach, & R. W. Damon, " Surface magnetostatic modes and surface spin waves," *Phys. Rev.* **18**, 1208-1211, 1960.

70. R. W. Damon, & J. R. Eshbach, " Magnetostatic modes of a ferromagnet slab," *J. Phys. Chem. Solids* **19**, 308, 1961.

71. J. H. Collins, J. M. Owens, & C. V. Smith, "Magnetostatic wave signal processing," *Proc. IEEE UltrasonicsSymp*. (IEEE, New York), pp. 541-552, 1977.

72. D. C. Ralph, and M. D. Stiles, "Spin transfer torques," J. Magn. Magn. Mater., vol. 320, 1190, 2008.

73. M. Yamanouchi, D. Chiba, F. Matsukura, and H. Ohno, "Current-induced domain-wall switching in a ferromagnetic semiconductor structure," *Nature* 428 539, 2004.

74. L. Liu, C. F. Pai, Y. Li, H. W. Tseng, D. C. Ralph and R. A. Buhrman, "Spin-torque switching with the giant spin Hall effect of tantalum," *Science* **336** 555, 2012.

75. A. R. Mellnik, J. S. Lee, A. Richardella, J. L. Grab, P. J. Mintun, M. H. Fischer, A. Vaezi, A. Manchon, E. A. Kim, N. Samarth, and D. C. Ralph, "Spin transfer torque generated by a topological insulator," *Nature* **511** 449, 2014.

76. I. M. Miron, G. Gaudin, S. Auffret, B. Rodmacq, A. Schuhl, S. Pizzini, J. Vogel, and P. Gambardella, "Current-driven spin torque induced by the Rashba effect in a ferromagnetic layer," *Nat. Mater*. **9** 230, 2010.

77. Y. Shiota, T. Maruyama, T. Nozaki, T. Shinjo, M. Shiraishi, and Y. Suzuki Y, "Voltage assisted magnetization switching in ultrathin $Fe_{80}Co_{20}$ alloy layers," *Appl. Phys. Express* **2** 063001, 2009.

78. K. Roy, S. Bandyopadhyay and J. Atulasimha, "Energy dissipation and switching delay in stress-induced switching of multiferroic nanomagnets in the presence of thermal fluctuations," J. Appl. Phys., **112**, 023914, 2012.

79. H. Ahmad, J. Atuladsimha and S. Bandyopadhyay, "Electric field control of magnetic states in isolated and dipole coupled FeGa nanomagnets delineated on a PMN-PT substrate," *Nanotechnology* **26** 401001, 2015.

80. Y. Shiota, T. Nozaki, S. Tamaru, K. Yakushiji, H. Kubota, A. Fukushima, S. Yuasa, and Y. Suzuki, "Reduction in write error rate of voltage-driven dynamic magnetization switching by improving thermal stability factor,"*Appl. Phys. Lett*. **111** 022408, 2017.

81. A. D. Patil, S. Manipatruni, D. Nikonov, I. A. Young, and N. R. Shanbhag, "Shannon-inspired statistical computing to enable spintronics," 2017. (https://arxiv.org/abs/1702.06119).

82. U. Roy, T. Pramanik, L. F. Register, and S. K. Banerjee, "Write error rate of spin transfer torque random access memory including micromagnetic effects using rare event enhancement," IEEE Trans. Magnetics, 52, 3402106, 2016.

83. S. Khasanvis, M. Y. Li, M. Rahman, M. Salehi-Fashami, A. K. Biswas, J. Atulasimha, S. Bandyopadhyay and C. A. Moritz, "Self-similar magneto-electric nanocircuit technology for probabilistic inference engines," *IEEE Trans. Nanotechnol*. **14** 980, 2015.

84. S. Khasanvis, M. Y. Li, M. Rahman, A. K. Biswas, M. Salehi-Fashami, J. Atulasimha, S. Bandyopadhyay and C. A. Moritz, "Architecting for causal intelligence at nanoscale," *COMPUTER***48** 54, 2015.

85. S. Nasrin, J. L. Drobitch, S. Bandyopadhyay, and A. R. Trivedi, "Low power restricted Boltzmann machine using mixed mode magneto-tunneling junctions," *IEEE Elec. Dev. Lett*. **40** 345, 2019.

86. S. Bhanja, D. K. Karunaratne, R. Panchumarthy, S. Rajaram, and S. Sarkar, "Non-Boolean computing with nanomagnets for computer vision applications," *Nat. Nanotech*. **11**, 177, 2016.

87. M. Sharad, D. Fan, K. Aitken, and K. Roy, "Energy-efficient non-Boolean computing with spin neurons and resistive memory,"*IEEE Trans. Nanotechnol*. **13** 23, 2014.

88. A. K. Biswas, J. Atulasimha, and S. Bandyopadhyay, "The straintronic spin neuron," *Nanotechnology***26** 285201, 2015.

89. I. Chakraborty, A. Agrawal and K. Roy. "Design of a low-voltage analog-to-digital converter using voltage-controlled stochastic switching of low barrier nanomagnets", *IEEE Magnetics Lett*., **9** 3103905, 2018.

90. P. Debashis, R. Faria, K. Y. Camsari, and Z. Chen, "Design of stochastic nanomagnets for probabilistic spin logic,"*IEEE Magnetics Letters* **9**4305205, 2018.

91. K. Y. Camsari, R. Faria,B. M. Sutton, and S. Datta, "Stochastic p-bits for invertible logic," *Phys. Rev. X* **7** 031014, 2017.

92. B. Sutton, K. Y. Camsari,B. Behin-Aein, and S. Datta, "Intrinsic optimization using stochastic nanomagnets," *Sci. Rep*. **7** 44370 , 2017.

93. R. Faria, K. Y. Camsari, and S. Datta, "Low barrier nanomagnets as p-bits for spin logic,"*IEEE Magnetics Lett*. **8** 4105305, 2017.

94. S. Chikazumi, "*Physics of Magnetism,"* (Wiley, New York, 1964).

95. V. A. Bautin, A. G. Seferyan, M. S. Nesmeyanov and N. A. Usov, "Magnetic properties of polycrystalline cobalt nanoparticles", *AIP Advances* **7** 045103, 2017.

96. J. Bass and W. P. Pratt, Jr., "Spin-diffusion lengths in metals and alloys, and spin flipping at metal/metal interfaces: An experimentalist's critical review, *J. Phys: Condens. Matt*., **19** 183201, 2007.

97. A. Z. Pervaiz, L. A. Ghantasala, K. Y. Camsari and S. Datta, "Hardware emulation of stochastic p-bits for invertible logic," *Sci. Rep*. **7** 10994, 2017.

98. N. D'Souza, A. Biswas, H. Ahmad, M. Salehi-Fashami, M. M. Al-Rashid, V. Sampath, D. Bhattacharya, M. A. Abeed, J. Atulasimha and S. Bandyopadhyay, "Energy-efficient switching of nanomagnets for computing: Straintronics and other methodologies," Nanotechnology, **29**, 442001 2018.

99. S. Dey Manasi, M. M. Al-Rashid, J. Atulasimha, S. Bandyopadhyay and A. R. Trivedi, "Skewed Straintronic Magnetotunneling-Junction-Based Ternary Content Addressable Memory – Part I," IEEE Trans. Elec. Dev., **64**, 2835-2841, 2017.

100. K. Pagiamtzis and A. Sheikholeslami, "Content-addressable memory (CAM) circuits and architectures: A tutorial and survey," IEEE J. Solid State Circuit*s*, 41, 712, 2006.

101. See, for example, Rudolf F. Graf, *Modern Dictionary of Electronics*, 7th ed. (Amsterdam, 1999), p. 638.

102. Z. Zeng, P. K. Amiri, I. N. Krivorotov, H. Zhao, G. Finocchio, J-P Wang, J. A. Katine, Y. Huai, J. Langer, K. Galatsis, K. L. wang and H. W. Jiang, "High-power coherent microwave emission from magnetic tunnel junction nano-oscillator with perpendicular anisotropy," ACS Nano, **6**, 6115, 2012.

103. M. Salehi-Fashami, J. Atulasimha and S. Bandyopadhyay, "Magnetization dynamics, throughput and energy dissipation in a universal multiferroic logic gate with fan-in and fan-out," Nanotechnology, **23**, 105201 (2012).

104. K. Roy, S. Bandyopadhyay and J. Atulasimha, "Metastable state in a shape-anisotropic single-domain nanomagnet subjected to spin-transfer-torque," Appl. Phys. Lett., **101**, 162405, 2012.

105. W. X. Xia, K. Inoue, S. Saito and M. Takahashi, "Effect of Rh spacer on synthetic-antiferromagnetic coupling in FeCoB/Rh/FeCoB films," J. Phys. Conf. Ser., **266**, 012064, 2011.

106. M. O. A. Ellis, M. Stamenova and S. Sanvito, "Multiscale modeling of current-induced switching in magnetic tunnel junctions using ab-initio spin transfer torques," Phys. Rev. B., **96**, 224410, 2017.

107. S. Pathak, J. Cha, K. Jo, H. Yoon and J. Hong, "Fast efficient STT switching in MTJ using additional transient pulse current," App. Phys. Lett., **110**, 232401, 2017.

108. P. Li, A. Chen, D. Li, Y. Zhao, S. Zhang, L. Yang, Y. Liu, M. Zhu, H. Zhang and X. Han, "Electric field manipulation of magnetization rotation and tunneling magnetoresistance of magnetic tunnel junctions at room temperature," Adv. Mater., **26**, 4320, 2014.

109. S.-E Park and T. R. Shrout, "Ultrahigh strain and piezoelectric behavior in relaxor based ferroelectric single crystals," J. Appl. Phys., **82**, 1804, 1997.

110. V. T. Lee, A. Alaghi and L. Ceze, "Correlation manipulating circuits for stochastic computing", https://arxiv.org/pdf/1803.04862.pdf

111. A. Alaghi and J. P. Hayes, "Survey of Stochastic Computing", ACM Transactions on Embedded Computing Systems, 12, 92, 2013.

112. Y. Liu, M. Parhi, M. D. Riedel and K. K. Parhi, "Synthesis of correlated bit streams for stochastic computing" 50th Asilomar Conference on Signals, Systems and Computers, 2016.

113. A. Alaghi and J. P. Hayes, "Exploiting correlation in stochastic circuit design", 31st IEEE International Conference on Computer Design, Asheville, NC, 2013.

114. K. Ried, M. Schnell, F. Schatz, M. Hirscher, B. Ludescher, W. Sigle and H. Kronmüller, "Crystallization behavior and magnetic properties of magnetostrictive TbDyFe films", Phys. Status Solidi A. **167,** 195, 1999.

115. R. Kellogg and A. Flatau, "Experimental investigation of Terfenol-D's elastic modulus", J. Intell. Mater. Syst. Struct. 19**,** 583, 2008.

116. S. Barman, S. Wang, et al., "Size-dependent Damping in Picosecond Dynamics of Single Nanomagnets," *Appl. Phys. Lett*. 90, 202504, 2007.

117. Y. Yahagi, B. Hartenek, S. Cabrini, H. Schmidt, " Controlling Nanomagnet Magnetization Dynamics via Magneto-elastic Coupling," *Phys. Rev. B*. 90, 140405(R) ,2014.

118. Y. Yahagi, C. Berk, B. Hebler, S. Dhuey, S. Cabrinia, M. Albrecht, H. Schmidt, " Optical Measurement of Damping in Nanomagnet Arrays Using Magneto-elastically Driven Resonances," *J. Phys. D: Appl. Phys.* 50, 17LT01, 2017.

119. Y. Yahagi, B. Hartenek, S. Cabrini, H. Schmidt, "In Control of Magnetization Dynamics in Patterned Nanostructures with Magnetoelastic Coupling, Photonic and Phononic Properties of Engineered Nanostructures V; Adibi, A., Lin, S.-Y., Scherer, A., Eds.; Proceedings of SPIE, Vol. 9371, 2015.

120. V. Sampath, N. D'Souza, D. Bhattacharya, G. M. Atkinson, S. Bandyopadhyay and J. Atulasimha, "Acoustic-Wave-Induced Magnetization Switching of Magnetostrictive Nanomagnets from Single-Domain to Nonvolatile Vortex States," *Nano. Lett*. **16,** 9, 2016.

121. K. Roy, S. Bandyopadhyay, and J Atulasimha, " Energy-efficient Mixed Mode Switching of a Multiferroic Nanomagnet," https://arxiv.org/abs/1012.0819 (submitted Dec 03, 2012).

122. K. H. Choi, J. H. Oh, H. J. Kim, J. Y. Kim, "Surface Acoustic Wave Propagation Properties of the Relaxor Ferroelectric PMN−PT Single Crystal," *IEEE Ultrasonics Symposium*, Vol 1, p 161-163, 2001.

123. A. M. James, M. P. Lord, "Macmillan's Chemical and Physical Data," Macmillan: London, U.K., 1992.

124. R. Zhang, B. Jiang, W. Cao, "Elastic, Piezoelectric and Dielectric Properties of Multidomain 0.67Pb(Mg1/3Nb2/3)O3- 0.33PbTiO3 Single Crystals," *J. Appl. Phys.* 90, 3471−3475, 2001.

125. C. Kittel, "On the Theory of Ferromagnetic Resonance Absorption," *Phys. Rev.* 73, 155−161, 1948.

126. Quantum Annealing and Related Optimization Methods, Eds. A. Das and B. K. Chakrabarti (Springer-Verlag, Berlin Heidelberg, 2005).

127. A. K. Biswas, S. Bandyopadhyay and J. Atulasimha, "Acoustically assisted spin-transfer-torque switching of nanomagnets: An energy-efficient hybrid writing scheme for non-volatile memory," *Appl. Phys. Lett.,* 103, 232401, 2013.

128. S. Davis, A. Baruth and S. Adenwalla, "Magnetization dynamics triggered by surface acoustic waves, " *Appl. Phys. Lett.,* 97, 232507, 2010.

129. W. Li, B. Buford, A. Jander and P. Dhagat, "Acoustically assisted magnetic recording: A new paradigm in magnetic data storage," IEEE Trans. Magn. 50, 2285018, 2014.

130. W. Li, B. Buford, A. Jander and P. Dhagat, "Writing magnetic patterns with surface acoustic waves," *J. Appl. Phys*. 115 17E307, 2014.

131. O. Kovalenko, T. Pezeril and V. V. Temnov, "New concept for magnetization switching by ultrafast acoustic pulses," *Phys. Rev. Lett.,* 110, 266602, 2013.

132. L. Thevenard, J.-Y. Duquesne, E. Peronne, H. von Bardeleben, H. Jaffres, S. Ruttala, J.-M. George, A. Lemaître and C. Gourdon, 'Irreversible magnetization switching using surface acoustic waves," *Phys. Rev. B* 87, 144402, 2013.

133. U. Singh and S. Adenwalla, "Spatial mapping of focused surface acoustic waves in the investigation of high frequency strain induced changes," *Nanotechnology* 26, 25, 2015.

134. E. M. Chudnovsky and R. Jaafar, "Manipulating the magnetization of a nanomagnet with surface acoustic waves: Spin-rotation mechanism," *Phys. Rev. Appl.* 5 031002, 2016.

135. M. Foerster, F. Macià, N. Statuto, S. Finizio, A. Hernández-Mínguez, S. Lendínez, P. V. Santos, J. Fontcuberta, J. M. Manel Hernàndez, M. Kläui and L. Aballe, "Direct imaging of

delayed magneto-dynamic modes induced by surface acoustic waves," *Nat. Commun.,* 8, 407, 2017.

136. A. V. Scherbakov, A. S. Salasyuk, A. V. Akimov, X. Liu, M. Bombeck, C. Brüggemann, D. R. Yakovlev, V. F. Sapega, J. K. Furdyna and M. Bayer, "Coherent Magnetization Precession in Ferromagnetic (Ga,Mn)As Induced by Picosecond Acoustic Pulses," *Phys. Rev. Lett.,* 105, 117204, 2010.

137. L. Thevenard, I. S. Camara, S. Majrab, M. Bernard, P. Rovillain, A. Lemaître, C. Gourdon and J.- Y. Duquesne, "Precessional magnetization switching by a surface acoustic wave," *Phys. Rev. B,* 93, 134430, 2016.

138. M. Weiler, L. Dreher, C. Heeg, H. Huebl, R. Gross, M. S. Brandt and S. T. B. Goennenwein, "Elastically Driven Ferromagnetic Resonance in Nickel Thin Films," *Phys. Rev. Lett.,* 106, 117601, 2011.

139. Z. Yao, Y. E. Wang, S. Keller, G. P. Carman, "Bulk acoustic wave mediated multiferroic antennas: architecture and performance bound," *IEEE Trans. Antennas Propag*. *63*, 3335–44, 2015.

140. J. P. Domann, G. P. Carman, " Strain powered antennas," *J. Appl. Phys*. *121*, 044905, 2017.

141. T. Nan, et al., "Acoustically actuated ultra-compact NEMS magnetoelectric antennas," *Nat. Commun*. *8*, 296, 2017.

142. H. Lin, et al., "NEMS magnetoelectric antennas for biomedical applications," *IEEE/MTT-S Int. Microwave Biomedical Conf.*, 13–15, 2018

143. H. Lin, M. R. Page, M. McConney, J. Jones, B. Howe, N. X. Sun, " Integrated magneto-electric devices: filters, pico-Tesla magnetometers, and ultra-compact acoustic antennas," *MRS Bull.*, *43*, 841–847, 2018.

144. G. Y. Guo, S. Murakami, T.-W. Chen, and N. Nagaosa, "Intrinsic Spin Hall Effect in Platinum: First-Principles Calculations," Phys. Rev. Lett. 100, 096401, 2008.

145. A. J. Berger, E. R. J. Edwards, H. T. Nembach, O. Karis, M. Weiler, and T. J. Silva, "Determination of the spin Hall effect and the spin diffusion length of Pt from self-consistent fitting of damping enhancement and inverse spin-orbit torque measurements," Phys. Rev. B 98, 024402, 2018.

146. S. M. Mohseni, S. R. Sani, J. Persson, T. N. Anh Nguyen, S. Chung, Ye. Pogoryelov, J. Akerman, J., "High frequency operation of a spin-torque oscillator at low field," *Phys. Satus Solidi RRL*, *12*, 432, 2011.

147. S. Datta, "*Surface Acoustic Wave Devices*," Prentice Hall, Englewood Cliffs, New Jersey, 1986.

148. S. Bhuktare, A. S. Shukla, H. Singh, A. Bose, A. A. Tulapurkar, " Direct observation of reciprocity between spin current and phonon interconversion," *Appl. Phys. Lett*., *114*, 052402, 2019.